

En face retinal imaging

THÈSE N° 8518 (2018)

PRÉSENTÉE LE 18 AVRIL 2018

À LA FACULTÉ DES SCIENCES ET TECHNIQUES DE L'INGÉNIEUR
LABORATOIRE DE DISPOSITIFS PHOTONIQUES APPLIQUÉS
PROGRAMME DOCTORAL EN PHOTONIQUE

ÉCOLE POLYTECHNIQUE FÉDÉRALE DE LAUSANNE

POUR L'OBTENTION DU GRADE DE DOCTEUR ÈS SCIENCES

PAR

Dino CARPENTRAS

acceptée sur proposition du jury:

Prof. H. Altug, présidente du jury
Prof. C. Moser, directeur de thèse
Prof. F. Behar-Cohen, rapporteuse
Dr P. Ferraro, rapporteur
Prof. M. Unser, rapporteur



ÉCOLE POLYTECHNIQUE
FÉDÉRALE DE LAUSANNE

Suisse
2018

To Caterina.

For always being with me;
even when I am extremely annoying.

Acknowledgements

I really would like to thank my thesis director: Prof. Christophe Moser of the École polytechnique fédérale de Lausanne (EPFL), Switzerland, for all the help and the extremely useful advices over the past years.

I would also like to thank two collaborators that mostly contributed to the development of the retinal phase imaging method: Dr. Timothé Laforest and Mr. Mathieu Künzi, EPFL. Without their hard work and brilliant ideas, this thesis would not have been the same.

I would also like to thank the experts who were involved in the retinal phase imaging project: Prof. Francine Behar-Cohen and Dr. Laura Kowalczuk of the Faculty of Biology and Medicine, University of Lausanne, Switzerland, for their help with biological samples and for all the fruitful discussions.

Finally, I am also grateful to the other present and past members of the Laboratory of Applied Photonics Devices for creating such an amazing environment.

Dino Carpentras

21/01/2018

Abstract

Retinal imaging is routinely used to provide information about vision health. Recent studies showed that retinal images can also provide information on general health (e.g. stress level), brain pathologies and attention. Depending on the target information, different imaging systems can be chosen and optimized. This thesis will focus on two distinct challenges in ophthalmology.

The first one regards a see-through wearable ophthalmoscope for applications such as health monitoring and eye tracking. Such a system uses a scanning 2D micromirror that results in a compact confocal scanning laser ophthalmoscope. Another key feature of such a system is the use of a holographic plate on which a diffraction grating has been recorded. This allows the light from the laser beam to be diffracted to the eye without altering the patient's field of view. Such a system is proposed and analyzed with simulations and with a proof of concept setup.

The second challenge regards in-vivo imaging of retinal microstructures. Indeed, with the current state-of-the-art technology, it is still not possible to observe the morphology of transparent cellular structures in the top layers of the living retina with high contrast in a time frame relevant for use in patients. Such a possibility is appealing since neuronal layers of the retina could be used to obtain information on degenerative diseases of both retina and brain. In this thesis, it is shown how asymmetrical illumination of the retina results in phase contrast and how this can be used for fast imaging modalities of cellular structures. The technique is here detailed with a theoretical model, numerical simulations and ex-vivo experimental validations.

Keywords

Ophthalmology, ophthalmic devices, funduscopy, fundus imaging, ganglion cells, retinal imaging, phase imaging, phase contrast, wearable device, wearable healthcare, point of care.

Abstract

L'osservazione del fondo oculare è solitamente utilizzata per ottenere informazioni riguardanti la salute dell'occhio. Recenti studi hanno mostrato che immagini del fondo oculare forniscono informazioni anche sullo stato generale di salute (es. sul livello di stress), patologie neurologiche e attenzione. A seconda dell'informazione che si desidera monitorare è possibile scegliere una differente modalità di acquisizione dell'immagine. In questa tesi mi focalizzerò su due differenti problematiche nel campo dell'oftalmologia.

La prima riguarda un oftalmoscopio indossabile che non interferisce con il campo visivo dell'utente. Un simile dispositivo potrebbe essere usato per applicazioni come oculometria o monitoraggio dei parametri vitali. Questo sistema usa un micro-specchio per effettuare la scansione del fascio laser, ottenendo un setup estremamente compatto. Un'altra caratteristica fondamentale di tale dispositivo è l'utilizzo di un reticolo di diffrazione stampato su di una pellicola fotosensibile. Questo permette di diffrangere il fascio laser senza alterare il campo visivo dell'utente. Analisi di tale sistema sono condotte con simulazioni ed esperimenti.

La seconda problematica riguarda l'osservazione di microstrutture nella retina vivente. Infatti, anche con l'utilizzo di tecniche all'avanguardia, non è possibile osservare la morfologia di strutture trasparenti con tempistiche adatte all'uso clinico. Un tale utilizzo è desiderabile dato che gli strati neuronali possono essere utilizzati per acquisire informazioni su malattie neurodegenerative. In questa tesi mostrerò come è possibile usare un'illuminazione asimmetrica per ottenere un contrasto di fase e come questo possa essere usato per una rapida visualizzazione di strutture retiniche. Tale tecnica sarà analizzata con un modello teorico, simulazioni numeriche ed esperimenti.

Parole chiave

Oftalmologia, dispositivi oftalmici, fundoscopia, gangli, scanner della retina, fondo oculare, contrasto di fase, dispositivi indossabili, point of care.

Content

Abstract.....	xi
Keywords.....	xi
Abstract.....	xiii
Parole chiave	xiii
Content	xv
Symbols and notation	19
Acronyms	23
Chapter 1 Introduction	25
1.1 The human eye	26
1.1.1 General structure	26
1.1.2 Retina	28
1.1.3 Eye motion	30
1.2 Retinal and optic nerve’s diseases	30
1.3 Applications of fundus imaging	32
1.4 Techniques for fundus imaging.....	34
1.4.1 Portable digital ophthalmoscopes.....	36
1.4.2 Wearable ophthalmoscopes	37
1.5 Eye tracking methods	38
1.6 Phase contrast microscopy	39
1.6.1 Label free cellular contrast in the eye	42
1.7 Alternative to transpupillary illumination.....	43
1.8 Structure of the thesis	45
Chapter 2 A wearable see-through ophthalmoscope	47
2.1 Optical design	47
2.2 Geometrical considerations.....	49
2.3 Ray tracing simulations.....	50
2.4 Experimental results	53
2.5 Conclusions.....	56
Chapter 3 Phase contrast imaging of retina	59
3.1 Theory.....	59
3.1.1 General theory	59
3.1.2 Ramp approximation.....	62

3.2	Simulations	64
3.2.1	Monte Carlo Simulations of backscattering	64
3.2.2	Shape of the transfer function	65
3.2.3	Alternative pupil functions	72
3.2.4	Non-linear illumination function	78
3.2.5	Phase contrast images	80
3.3	Experimental validation	82
3.3.1	Experimental setup	83
3.3.2	Relationship between slope and contrast	85
3.3.3	Backscattering of choroid.....	85
3.3.4	Phase contrast of retina sample.....	86
3.3.5	Gradient illumination	88
3.4	Conclusion	89
Chapter 4	Image reconstruction	91
4.1	Tian's method for reconstruction	91
4.2	Retinal image formation model	93
4.3	Normalization	96
4.3.1	Effect of the illumination intensity modulation	97
4.3.2	Effect of the backdiffraction from the first pass illumination	98
4.3.3	Phase reconstruction simulations	98
4.4	Ex-vivo experiments	102
Chapter 5	In-vivo experimentation.....	105
5.1	Eye safety for transscleral illumination.....	105
5.1.1	Introduction on Eye safety	105
5.1.2	MPE for transscleral illumination	107
5.1.3	Comparison with known cases	111
5.2	Experimental tests	112
5.3	Conclusion	117
Chapter 6	Conclusion	119
6.1	Achieved results	119
6.2	Future development	120
	References.....	123
	Appendix A – Ramp approximation	135

Symbols and notation

In this section I will define the symbols and the notation that will be used in the following of this thesis.

Vectors will always be represented in bold. In such a way that v will represent a scalar quantity and \boldsymbol{v} a vectorial one.

When a function f is defined by a spatial variable x (or \boldsymbol{x} in case of vectorial quantity), it will be represented as $f(x)$ (respectively $f(\boldsymbol{x})$) where x is either a spatial coordinate in real space or a spatial coordinate in Fourier space. If the function depends also on other non-spatial variables (in the following called “parameters”), they will be represented as subscripts. In this way, a function f dependent on a spatial coordinate \boldsymbol{x} and a parameter η , will be represented as $f_{\eta}(\boldsymbol{x})$.

In some cases, a function will depend on another function. Also in this case, the dependency will be placed as a subscript, but between square brackets to differentiate it from scalar parameters. So, if the values of a function $f(\boldsymbol{x})$ depends also on the values of another function $g(\boldsymbol{x}')$ I will write $f_{[g]}(\boldsymbol{x})$.

In some cases, for the sake of readability, subscripts or the dependence can be neglected, in such a way that a long expression, such as $f_{\alpha,\beta,\gamma}(\boldsymbol{x})$ will be written simply as f . When this happens, it will be mentioned in the text to avoid confusion.

If two functions of the same type, such as $f_{\alpha_1,\beta_1}(\boldsymbol{x})$ and $f_{\alpha_2,\beta_2}(\boldsymbol{x})$, are present in the same section, they might be simplified in a lighter notation such as: f_1 and f_2 . When this happens, it will be mentioned in the text.

Fourier transform will be represented, together with a change of the spatial coordinate, with the symbol: “ \sim ” over the letter which represents the function. i.e. the Fourier transform of the function $f(\boldsymbol{x})$ will be represented as $\tilde{f}(\boldsymbol{u})$, where \boldsymbol{u} is the spatial coordinate of the Fourier space.

The hat “ \wedge ” will be used over a vector to represent a unit vector. i.e. a vector \boldsymbol{v} , if normalized, will be represented as $\hat{\boldsymbol{v}}$.

The symbol “ \triangleq ” will be used to mean “definition.” This is used to distinguish between the original definition and other formulas obtained by approximation (denoted by the “ \sim ” symbol) and hypothesis.

A distinction will be made between mathematical symbols and letters or acronyms used to refer to specific components of a physical system. The first group will be written in italic, while the second one in standard text style. For example, a hologram is abbreviated as H and a function is represented as $H(x)$. Furthermore, to avoid confusion, the same letter will not be used to represent a function and a physical component in the same chapter.

In the following, a list of the symbols used in the thesis is provided.

Symbol	Notes	First appearance in section:
SPATIAL VARIABLES		
u	Spatial variable of component u_x and u_y .	3.1.1
u'	Spatial variable of component u'_x and u'_y .	3.1.1
u''	Spatial variable of component u''_x and u''_y .	3.1.1
x	Spatial variable of component x and y .	3.1.1
FUNCTIONS		
$\gamma(\sim)$	Radial component of the phase transfer function $g(\sim)$.	3.2.2
$\phi(\sim)$	Phase function.	1.6
$\mu(\sim)$	Absorption function.	3.1.1
$\delta(\sim)$	Dirac's delta function	3.1.1
$\rho(\sim)$	Reflectance of the eye fundus	4.2
$b(\sim)$	Angular profile of the backscattered light.	4.2
$D(\sim)$	Intensity of the backdiffracted light	4.2
$G(\sim)$	Phase transfer function	3.1.1
$G'(\sim)$		4.2
$g(\sim)$	Normalized phase transfer function	3.1.1
$g'(\sim)$		3.1.2
$g^\circ(\sim)$	Normalized phase transfer function in case of ramp approximation	3.1.2
$H(\sim)$	Absorption transfer function	3.1.1
$H'(\sim)$		4.2
$h(\sim)$	Normalized absorption transfer function	3.1.1
$h'(\sim)$		3.1.2
$h^\circ(\sim)$	Normalized absorption transfer function in case of ramp approximation	3.1.2
$I(\sim)$	Intensity at the camera's plane (image).	3.1.1
$i(\sim)$	Light's intensity at the eye fundus	4.2
$J(\sim)$	Normalized image	3.1.1
$l(\sim)$	Angular component of the phase transfer function	3.2.2
$N(\sim)$	White noise function.	3.2.4

$P(\sim)$	Pupil function.	3.1.1
$p'(\sim)$	Circular pupil function.	3.1.2
$Q(\sim)$	Illumination propagated at the object's plane.	3.1.1
$S(\sim)$	Luminous intensity at the display's surface.	3.1.1
$S^\circ(\sim)$	Linear luminous intensity at the display's surface.	3.1.2
$S_{ev}(\sim)$	Even part of the illumination function S	3.1.1
$S_{odd}(\sim)$	Odd part of the illumination function S	3.1.1
$\bar{S}(\sim)$	Spatial average of the product $S P$	4.2
PARAMETERS		
φ	Azimuthal angle of the illumination function	3.1.2
θ	Angular parameter.	2.2
λ	Wavelength	1.4
A	Surface's area.	5.1.2
a_i	Internal radius of a ring.	3.2.3
d	Distance.	2.2
D	Diameter.	2.2
E	Luminous intensity	5.1.1
f	Frequency of a signal.	2.4
f_e	Focal distance of the eye.	5.1.2
I_{DC}	Temporal average of the current.	2.4
M	Magnification.	2.2
m	Slope of the linear illumination function $s(\sim)$	3.1.2
NA	Numerical Aperture	1.4
q	Mean value of the linear illumination function $s(\sim)$	3.1.2
r	Normalized slope of the illumination function $s(\sim)$.	3.1.2
T	Thickness.	2.2
t	Time.	5.1.2
OTHERS		
\mathbf{v}_φ	Unit vector of the form $\mathbf{v}_\varphi = \cos(\varphi)\hat{\mathbf{x}} + \sin(\varphi)\hat{\mathbf{y}}$	3.1.2
$\hat{\mathbf{x}}$	Unit vector \mathbf{x} parallel to the x-axis.	3.1.2
$\hat{\mathbf{y}}$	Unit vector \mathbf{y} parallel to the y-axis	3.1.2
B	Mean value of the image $I(\sim)$	3.1.1
CONSTANTS		
j	Imaginary constant $j = \sqrt{-1}$.	3.1.1
π	The ratio between the circumference of a circle and its diameter.	2.4
e	Euler's number $e = \sum_{n=1}^{\infty} \frac{1}{n!}$.	1.6
q_e	Electron's charge $q_e \sim -1.6 \cdot 10^{-19} C$.	2.4
OPERATORS		
$Abs\{\sim\}$	Absolute value.	3.2.4
$\varepsilon_p\{\sim\}$	Pixelwise error	3.2.4
$Low\{\sim\}$	Low pass filter.	3.3.1

Acronyms

In the following table I listed the acronyms that will be used along the text, together with its first appearance.

Acronym	Meaning	First appearance in section:
AMD	Age-related Macular Degeneration	1.2
AMOLED	Active Matrix Organic Light Emitting Diode	3.3.1
cSLO	Confocal Scanning Laser Ophthalmoscope	1.4
DIC	Differential Interference Contrast	1.6
DPC	Differential Phase Contrast	4.1
FDA	American Food and Drugs Administration	5.1.3
FOV	Field of View	2.2
FWHM	Full Width Half Maximum	2.3
GCL	Ganglion Cell Layer	1.1.2
ICNIRP	International Commission on Non-Ionizing Radiation Protection	5.1
INL	Inner Nuclear Layer	1.1.2
IPL	Inner Plexiform Layer	1.1.2
IS	Inner Segment	1.1.2
LED	Light Emitting Diode	3.3.1
MPE	Maximum Possible Exposure	5
MTF	Modulation Transfer Function	3.1.1
NA	Numerical Aperture	1.4
NFL	Nerve Fiber Layer	1.1.2
OCT	Optical Coherence Tomography	1.4
OPL	Outer Plexiform Layer	1.1.2
OS	Outer Segment	1.1.2
PBS	Polarizing Beam Splitter	2.1
PSF	Point Spread Function	3.1.1
RPE	Retina Pigmented Epithelium	1.1.1
SLO	Scanning Laser Ophthalmoscope	1.4
WOA	Weak Object Approximation	1.6
ZPC	Zernike Phase Contrast	1.6

Chapter 1 Introduction

Imaging of the eye fundus is currently used to provide key information about vision health. Indeed, some of the major causes of blindness, such as age-related macular degeneration [1], can be identified thanks to fundus imaging [2]. Furthermore, recent studies showed how eye imaging can be used also for different purposes, such as acquiring information on brain neurodegenerative diseases (such as Alzheimer's disease) [3], poison detection [4], mental state (such as attention) [5, 6] and personal preferences [7]. Depending on the targeted information, different characteristics are required from the acquisition system, such as: compactness, speed to obtain the information, contrast and image resolution. This thesis is divided in two distinct parts, each addressing a current challenge in ophthalmology.

The first part regards the development of a compact, wearable ophthalmoscope, able to perform continuous acquisition of retinal images without interfering with the user's field of view. Such a device is appealing for performing continuous monitoring for applications such as eye tracking and poisoning detection.

The second part is related to the challenge of imaging transparent cellular structures in the living retina, such as ganglion cells. Retinal microstructural changes have been linked to the development of retinal degenerative diseases [8, 9] and the ability to visualize microstructures *in vivo* in the retina, chronically, is fundamental to understand the root causes of these diseases. A device with such an ability could also potentially lead to an early diagnosis tool. However, with state of the art technology, it is still not possible to image relevant microstructures in a time frame short enough (< 30 sec) to enable clinical use [10].

In this chapter, I will introduce the key concepts that will be used in the following chapters, together with a review of the current state of the art in the most relevant fields. In section 1.1, I will review the key information on the human eye, with emphasis on the retina and eye motion, while in section 1.2, I will describe the most common retinal degenerative diseases. In section 1.3, I will detail how retinal imaging can be used for obtaining meaningful information outside the field of ophthalmology and in section 1.4, I will describe the state of the art in retinal imaging. Section 1.5 will be used to explain eye tracking methods both for the purpose of recording gaze direction and for compensating for eye movement (e.g. for stabilizing retinal acquisition). In section 1.6, I will discuss about phase contrast in microscopy, introducing the techniques that will be then developed

from chapter 3. In section 1.7, I will discuss transscleral illumination in the eye and in section 1.8, I will clarify the structure of the thesis. This is useful to better understand how different sections in the introduction are linked to the rest of the thesis.

1.1 The human eye

Since the time of ancient Greek philosophers, sight is commonly thought as the most important of the five senses [11]. This comes from the fact that human sight provides a precise estimation of the surrounding three-dimensional space. In humans, the only organs that allow for image formation are the two eyes [12].

In this section, I will present the eye structures and features that will be relevant for future discussion in this thesis. It is however important to remind that this is not a complete description of the eye anatomy, for which I suggest the reading of dedicated books, such as Snell's and Lemp's Clinical Anatomy of the Eye [13].

1.1.1 General structure

The human eye is commonly divided in two segments: the anterior and the posterior one [14]. The anterior segment contains the biological structure for rays' refraction (such as the cornea and the lens) [15], while the posterior one allows for free propagation of rays and the transduction from the image to biological signal [16].

The most external layer is the fibrous tunic (also known as corneoscleral), which can be still divided in two distinct tissues: the cornea and the sclera [17]. Even if they are both composed of collagen fibrils [18], the appearance is strongly different, since the sclera has an opaque white appearance, while the cornea is fully transparent (see Figure 1.1). This main difference is due to the distribution of the collagen fibrils which, in the case of the cornea, shows high lateral order, which strongly improves the light transmission [19]. In the posterior segment, moving towards the center of the eyeball, after the sclera, we find the choroid, a dark looking layer rich in melanin [20]. Closer to the eyeball's center lays the retina. This membrane is mostly transparent except for a strongly absorbing layer, called the retina pigmented epithelium (RPE). This layer is rich in melanin and lipofuscin, two pigments that provide the dark looking color of the RPE [21, 22]. The RPE has many functions, one of which is to decrease the amount of light scattered from the eye fundus. Closer to the center is a cavity, called posterior chamber and filled of a transparent media called vitreous humor.

Some of the structures mentioned for the posterior segment are common to the anterior segment, which differs strongly only in the region beneath the cornea. Indeed, here, instead of the choroid, there is a cavity called: “anterior chamber.” This is filled of a transparent medium called: “aqueous humor.” At the opposite extremity of this cavity we find the iris, a diaphragm whose color can differ from person to person. The aperture generated from the iris is called “pupil.” The crystal-line lens is located just below the iris. It is a transparent structure that strongly refracts light [15].

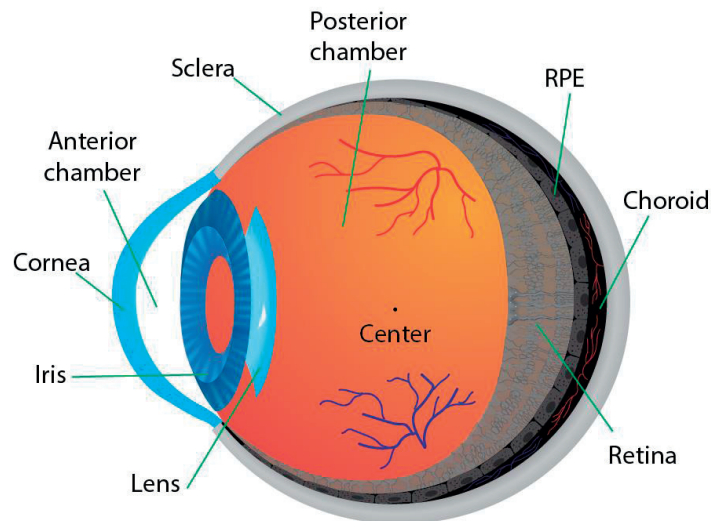


Figure 1.1

Scheme of the human eye and its main structures.

To better understand image formation, we follow the path of light from the outside world to the electrical signal ready to be sent to the brain. When light impinges on the eye, part of it is stopped by the eyelid and sclera. The other part of light, which will go through the pupil, is refracted thanks to the cornea [23] and crystalline lens [24]. Light is then transmitted through the transparent vitreous humor that fills the posterior chamber and reaches the retina. Photoreceptors are not placed on top of the retina, so, before being converted into electrical signal, light need to travel through many different cellular layers [15]. These layers are transparent, so as to maximize light transmission. Also, it is currently under debate if some cells, such as the Muller Ganglion Cells, can act similarly to optical fibers [25, 26], and so improve light transport to the bottom of the retina. Once light reaches the photoreceptors it is absorbed and transformed in electrical signal.

1.1.2 Retina

In the second part of this thesis (chapters 3 to 5), I will discuss the techniques to image cellular structures in the retina. Because of that, it is useful to detail some of the major structures that can be found in the human retina.

Several cells are present in the retina, such as: astrocytes, ganglion cells, Müller glial cell, amacrine, bipolar cell, horizontal cells, microglia and photoreceptors (see Figure 1.3) [13]. Photoreceptors are divided into two categories: rods (~91 millions) and cones (~4.5 millions), whose density distribution is given in Figure 1.2 [27]. Rods provide black and white vision in low light condition and are sensitive enough to respond to single photon excitation [28]. Cones are furthermore divided in 3 types: L, M and S (which stand for long, medium and short wavelength, respectively) each one characterized by a different absorbance spectrum. This characteristic gives humans trichromatic color vision [29].

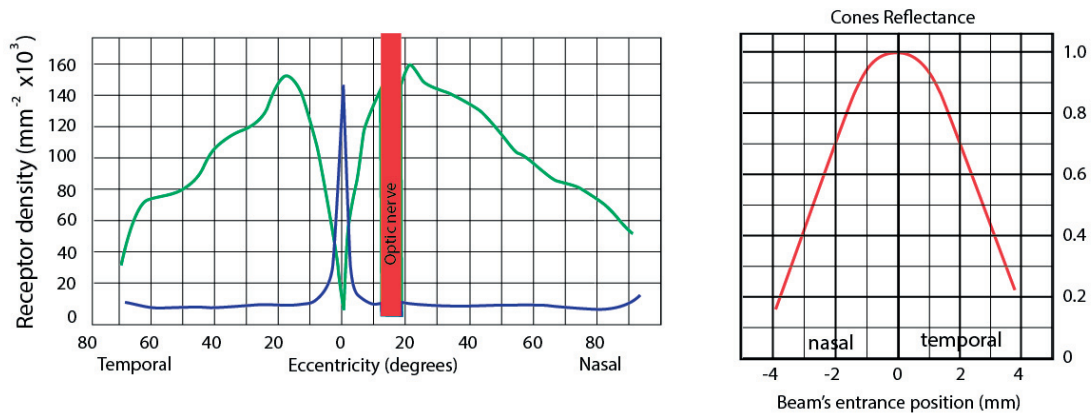


Figure 1.2

Left) Photoreceptor's distribution depending on the eccentricity. Cones have a strong peak at the center of vision. At the optic nerve both rods and cones are absent, representing a blind spot. In all the other regions the rods' density is higher than the cones' one. Right) Graph of the reflectance of cone photoreceptors depending on beam's entrance position [30, 31].

In fundus imaging, cone cells appear as strongly reflective discs, but, due to Stiles-Crawford effect, this intensity has been showed to be dependent on the illumination angle [30, 31]. Photoreceptors are connected to ganglion cells, a type of neuron characterized by a long axon. These axons form the optic nerve that connects the retina to the brain [32].

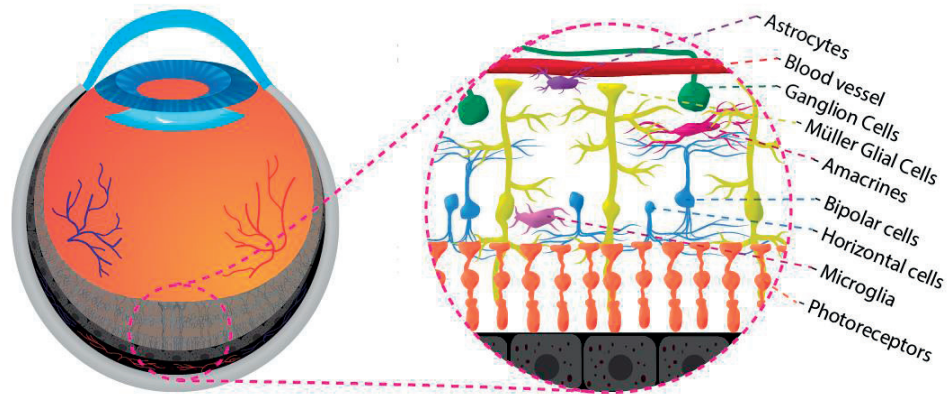


Figure 1.3

Scheme of the main cells and structures that are present in the retina.

The previously mentioned cells are organized in different layers. The innermost (i.e. the closest to the eye center) is the nerve fiber layer (NFL) composed of the axons of the ganglion cells [33]. Moving towards the eye's periphery we find the ganglion cells layer (GCL), which hosts the somas of the ganglion cells, the inner plexiform layer (IPL) and then the inner nuclear layer (INL), a layer rich of bipolar cells. After the outer plexiform layer (OPL) we find the outer nuclear layer, which contains photoreceptors nuclei [34]. Photoreceptors are present in the two layers namely the inner segment (IS) and the outer segment (OS), but only the OS contains the photosensitive part of the cell [35].

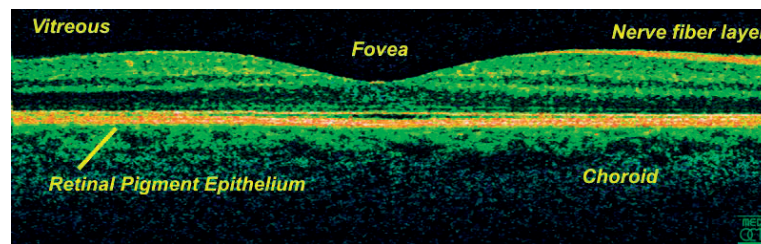


Figure 1.4

OCT scan of a retina at 800 nm with an axial resolution of 3 μm . The image shows different thickness values depending on the region. Courtesy of medOCT-group, Dept. of Med. Physics, Med. Univ. Vienna, Austria, 2004.

Retina thickness is not uniform, but ranges from about 200 μm to 350 μm depending on the region [36]. The fovea (the region responsible for central vision) is characterized by a thin retinal

region, surrounded by thicker region. Fovea is also characterized by a high density of cones photo-receptors and the absence of rods photoreceptors (as shown in Figure 1.2).

1.1.3 Eye motion

Another key feature of human eyes is movement. Understanding this phenomenon is fundamental for studying eye tracking either during an ophthalmic measurement or for recording eye motion during user's activity.

The image of a scene is not formed in the brain only by a single static acquisition, but rather from fixation of different areas. The quick eye movement between two fixation phases is known as saccade [14]. Eye motion during a saccade can undergo eye rotations up to 90° and be as fast as 700° per second [37].

Usually, ophthalmologists use a fixation target to minimize saccades. Nevertheless, even while fixating a point, the human eye is never completely at rest. Usually, three different type of movement are distinguished during fixation: microsaccades, ocular drift and tremor. It is however important to say that some authors consider this distinction only historical and do not recognize a real difference between eye movements during fixation [38].

Microsaccade has been classified as an involuntary erratic motion, similar to saccade in speed, but limited to 12 arc min [39]. Eye drift has been defined as a movement below 40 Hz, with an average speed of $\sim 1^\circ/\text{s}$ [40, 41], while tremor is defined by frequencies above 40 Hz. Furthermore, tremor is also limited to movements whose amplitude is in the range of the size of a photo-receptor in the fovea; making analysis of this movement extremely challenging [38]. All these different types of movement need to be compensated if a sensitive acquisition is required. In section 1.5, I will discuss about eye tracking and compensation methods.

For the sake of completeness, the human eye also shows different type of movement, for example during the rapid eyes movement (REM) phase of sleep. However, analysis of similar phenomena is beyond the goal of this thesis.

1.2 Retinal and optic nerve's diseases

Different pathological conditions can affect vision. Some affects eye areas involved in the way the image is formed on the retina (such as keratoconus or myopia [42]), some other affects the

phototransduction and transmission of the electrical signal (such as macular degeneration [43]) and some affects the way signal is processed in the brain (such as prosopagnosia [44]). In this section, I will focus my attention on some of the most common diseases that affects the retina and the optic nerve, which represents the main motivation for the development of techniques for in vivo observation of retinal cellular structures (analyzed in chapters 3 to 5).

Macular degeneration, also known as Age-related Macular Degeneration (AMD) is a retinal degenerative disease that may produce blurred or even absence of sight in the area of central vision [45]. The disease is also associated with the appearance in the retina of drusen which is an accumulation of extracellular material between the RPE and the Bruch's membrane (see Figure 1.5) [2]. It has been estimated that in 2020, 196 million people will suffer from AMD worldwide, and that in 2040 the number will rise to 288 million [1]. Furthermore, in 2010 the World Health Organization estimated that almost 5% of the 39.3 million visually impaired people across the world lost their vision due to AMD. With the current technology, it is still not possible to restore lost vision, but only to slow down the degenerative process [45, 46]. Because of that, early detection is crucial, but difficult, since early stages of AMD may be asymptomatic [45]. However, AMD has been shown to result in a thinning of the photoreceptor's layer [8], so detection of microstructural changes in retinal morphology might be used as an early diagnosis.

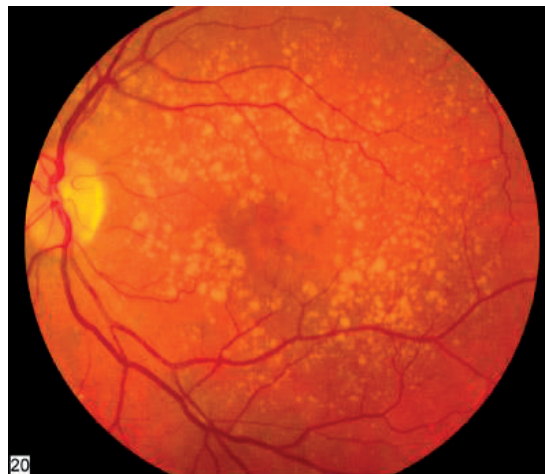


Figure 1.5

A fundus photo showing intermediate age-related macular degeneration. The yellow spots are the so-called “drusen.” Courtesy of the National Eye Institute, National Institutes of Health.

Diabetic retinopathy is a medical eye condition induced by diabetes [1] and it has been estimated to be responsible of 12% of all new cases of blindness [47]. Vision impairment is due to retinal

damage generated by aneurysms in the retinal blood vessels. Early stages of the disease may not produce any symptoms, however structural abnormalities can be identified even before development of microangiopathy signs [9].

	Estimated cases in 2013 (in millions)
Cataract	24.41
Diabetic Retinopathy	7.68
Glaucoma	2.72
AMD	2.07

Table 1.1

Statistics on ocular diseases in the United States of America [46]. It has been estimated that, by 2050 the quantities in the table will be roughly doubled.

The term “glaucoma” represent a class of eye diseases characterized by a progressive degeneration of ganglion cells [48]. Glaucoma is the second cause of blindness worldwide [49] and it has been estimated that 66.8 million people worldwide suffer from this disease [50]. Furthermore, due to the lack of symptoms in the early stages of such a disease, up to 50% of affected people in industrialized country are not informed of their situation and so they receive no treatment [51, 52]. However, a correlation has been shown between the loss of visual field and the decrease of the number of ganglion cells in the retina [53]. Furthermore, retinal ganglion cell apoptosis has been showed in vivo by using fluorescent staining [54].

For these discussed diseases, vision in the area of retinal damage cannot be restored and early diagnosis is thus currently the only way to slow down even further vision loss. In many cases, microstructural changes have been linked to appearance and development of the disease. Because of this, a noninvasive, high resolution, high contrast retinal cell imaging system is necessary to early detection and screening and is currently not available. In this thesis, I propose and demonstrate an imaging system that is a potential solution towards this goal.

1.3 Applications of fundus imaging

One of the main application of eye imaging is eyecare [55]. This is due to the fact that, by observing abnormalities in the eye it is possible to infer the presence of specific eye pathology. Imaging for

such a purpose involves both the external side of the eye (for diseases such as keratoconus) and the posterior segment (for diseases such as retinal detachment). Thanks to the optical transparency of the eye, observation of the inner layers of the eye by optical means can be performed in a non-invasive way. This also provides information on vasculature and neuronal structures. Indeed, optical fundus imaging can provide information such as: arterial and venous blood color [4], size and shape of vasculature [56] and state of neuronal degenerative diseases such as Parkinson and Alzheimer [57, 58] as explained below.

Observation of blood color through fundus imaging has been used by Molnar et al. [4] to detect real time poisoning from cyanide and arsenide. Indeed, these chemicals affect the oxygen content in arterial and venous blood and so their absorption spectrum. Besides color, also blood vessel's size has been linked to general health. Blood pressure and hypertension have been shown to produce micro change in retinal vessel size (see Figure 1.6) [59, 60, 61]. Furthermore, blood vessels pattern in the eye fundus has been shown to be unique for each individual, allowing for personal identification [62].

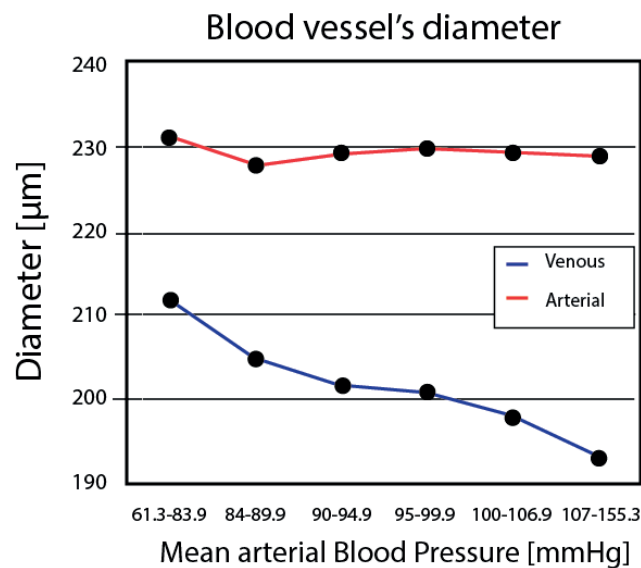


Figure 1.6

Change of blood vessel's diameter depending on the mean arterial blood pressure [60]. The black points represent experimental data. The error bar is smaller than the black points.

In 2011 Hamaoui et al. [3] observed, in mice's retina, the presence of β -amyloid plaques, which are Alzheimer's disease's hallmark. Similarly, α -synuclein, a neural protein linked to Parkinson

disease [63], has been observed in human affected by the disease [64]. In both cases the respective hallmarks were found in the inner retina [58].

Another application is the connection between the eye and the mind. Indeed, eye movements have been used for studying contextual awareness [65], human-computer interaction [66], mental state [5, 6], user's attention [67] and personal taste [7], which was then successfully applied to advertisement [68, 69].

1.4 Techniques for fundus imaging

Depending on the area of the eye that needs to be imaged, different methods are required (e.g. slit lamps for analysis of the anterior segment [70]). The term “ophthalmoscopes” is usually understood as a class of devices for fundus imaging. In this section, I will discuss about the main techniques for fundus imaging. These techniques are: direct ophthalmoscopy (which produces a virtual zoomed image of the retina), indirect ophthalmoscopy (which produces a real image of the retina on a camera), scanning laser ophthalmoscopy and optical coherence tomography.

Indirect ophthalmoscopes provide a large field of view image of the fundus. Imaging is performed by means of two main components: an optical system in the proximity of the ophthalmologist face, and a lens in the proximity of the patient's eye (see Figure 1.7). Between the two components a real image is formed [71].

Direct ophthalmoscopes are small imaging tools, which usually fit in one hand, which provide a high magnification image at the cost of a smaller field of view than indirect ophthalmoscopes. They work at a small distance to the patient's eye and produce a virtual image of the fundus [71].



Figure 1.7

Left) Fundus examination performed with an indirect ophthalmoscope. Courtesy of the American National Institute of Health. Right) Eye examination performed with a direct ophthalmoscope. Courtesy of the United States Air Force.

Standard ophthalmoscopes require the ophthalmologist to directly observe the fundus, while digital ophthalmoscopes record the image on a digital camera. Digital ophthalmoscopes are also called retinal cameras [72]. Some of them are able to reach the maximum spatial resolution, thanks to the use of adaptive optics systems. These systems are neither cheap nor portable (such as RTX1 [73]) since they require bulky and complex optics. However, the possibility of compensating for eye aberrations allows for imaging of some retinal microstructures, such as cone photoreceptors [74].

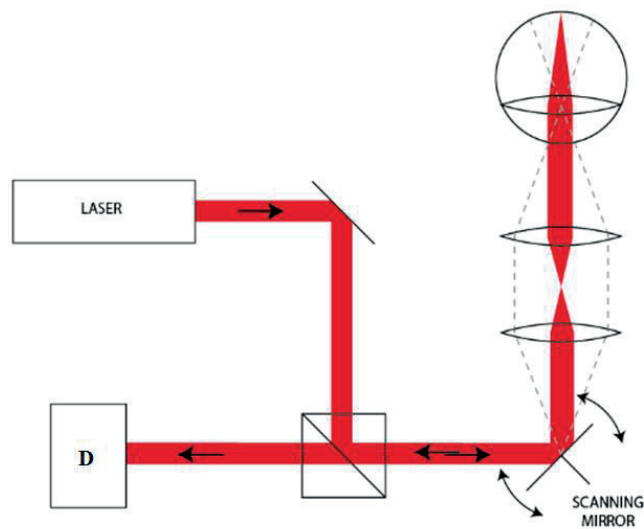


Figure 1.8

Scheme of a SLO. The laser beam is focused on the retina and scanned by a scanning mirror. The backscattered light follows the same path back to a detector (D), where the signal intensity is recorded.

Scanning laser ophthalmoscopy (SLO) is a special type of fundus imaging technique, which uses point by point scanning of a laser beam for image acquisition (see Figure 1.8) [75]. The Lateral resolution of such a system can be calculated is $0.66 \frac{\lambda}{NA}$ [76]. In many cases, to improve sectioning, the collected beam is then focused on a pinhole conjugated with the focus spot. This configuration is called confocal SLO (cSLO) [77] and it is able to reject most of the out of focus light. Lateral resolution is improved of a factor $\sqrt{2}$ and it is also obtained an axial resolution of $1.5 n \frac{\lambda}{NA^2}$ [76]. The main drawback of such a technique is the loss of signal power due to filtering in the case of an aberrated point spread function (PSF). A solution to this has been presented by Roorda, who used an adaptive optics system to compensate for aberrations before the confocal aperture. In this way

it is possible to filter out the out of focus light without rejecting the in-focus signal, as in an ideal confocal laser scanning system [78]. Even if cSLO provides sectioning, in order to obtain a 3D image of the retina, the system need to perform a 2D scan for each plane.

At the moment, the most common system for 3D imaging of the retina is the optical coherence tomography (OCT). OCT was invented in 1993 in the laboratory of James Fujimoto [79] and since then it experienced an extremely fast growth. In 1999 approximately 180 units were sold, by 2004 about 10 million procedures took place worldwide and in 2005 it became a standard of care [80]. Such a rapid growth is given by the ability of OCT to provide fast and accurate 3D images of the retina. Indeed, for Fourier domain OCT, a single position of the scanning beam allows for the acquisition of the entire depth profile along the beam [81] with a depth resolution of $\sim 0.44 \frac{\lambda_0^2}{\Delta\lambda}$ [82]. Where $\Delta\lambda$ is the source's spectrum and λ_0 is its carrier wavelength. Furthermore, even if standard OCT is not able to show *en face* images of cellular microstructures such as ganglion cells, it is able to show different retinal layers and eventual deformations in them. This has been implemented in the study of eye pathology that involves morphological changes, such as retinal detachment [83]. Currently, the use of new techniques for data analysis, allowed for the introduction of OCT angiography (OCTA). This imaging technique uses signal variation due to motion in OCT acquisition to provide images of the blood vessels within both retina and choroid without the use of contrast agent (and so fully non-invasive) [84].

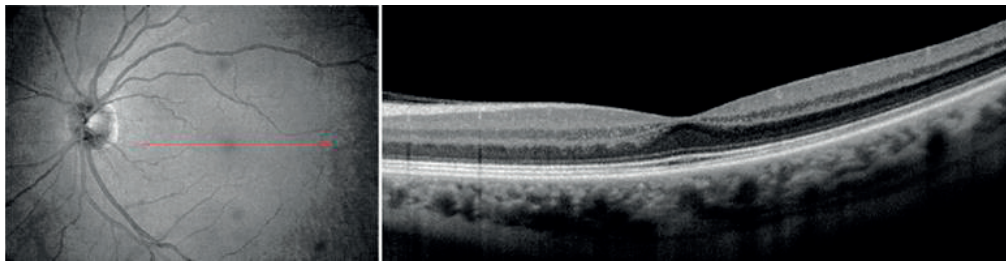


Figure 1.9

Left) En face image of the retina. Right) B-scan showing different layers. Courtesy of J. S. Duker [84]

1.4.1 Portable digital ophthalmoscopes

With the advent of small digital cameras, compact digital ophthalmoscopes appeared on the market. Some of these ophthalmoscopes, such as EyeQuickTM [85], use an integrated digital camera to replace the ophthalmologist's eye. Some other device, such as iExaminer [86], exploited the built-in properties of current smartphones (such as high-resolution camera with autofocus) and produced

an add-on to a mobile phone [87]. This is extremely useful for point of care, especially in developing countries. Indeed, by splitting the process of image acquisition and its interpretation, fundus images can be acquired also by non-specialized users. Once the digital image is recorded, it can be either digitally sent to specialist, or directly analyzed by a dedicated software [88].

Compactness has been introduced also for cLSO [89] and OCT [90, 91]. Such a system is required for non-collaborative patients, such as young children, who are not able to follow the ophthalmologist's instructions. This has been possible thanks to the use of two-dimensional scanning micromirrors, which provides both a compact imaging system and a fast acquisition rate. By using a compact OCT system it was possible to perform full acquisition at a frequency of 40 frame per second [90]. As we will see better in chapter 2, the main drawback of compact scanning systems is the small beam size, which result in a limit for the maximal achievable spatial (and axial) resolution.

1.4.2 Wearable ophthalmoscopes

By wearable ophthalmoscopes here, I refer to ophthalmoscopes that are worn by the patient and not by the ophthalmologist (such as many indirect ophthalmoscopes). Currently wearable ophthalmoscopes are based on cameras with a lens imaging the fundus, resulting in a direct ophthalmoscope, that is worn like a helmet or a pair of glasses.

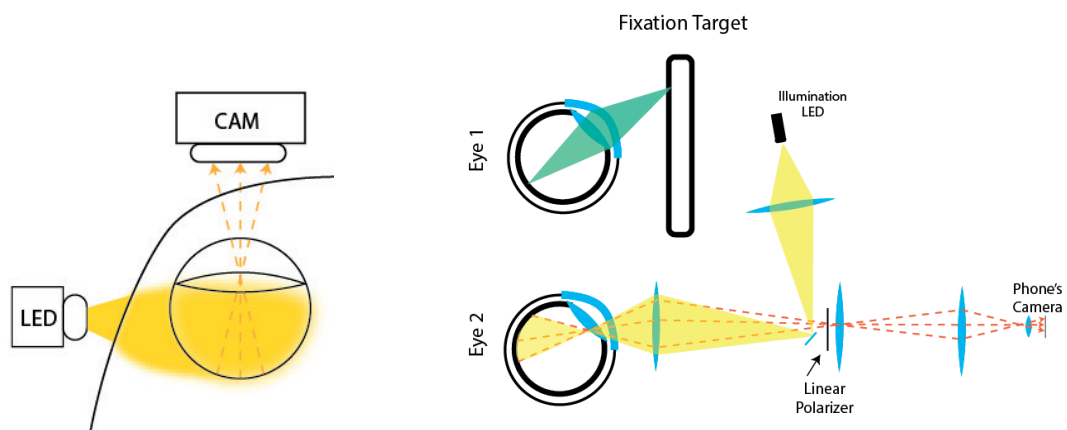


Figure 1.10

Left) Scheme of Lawson's setup. Top view of the user's head (head is pointing at the page's top). In the scheme it is represented the eye used for imaging in which the LED provides illumination through the temple. Right) Setup of Samaniego. Top view, the user's head is pointing at the right of the page. In the scheme it is shown the fixation target placed in front of eye 1, while eye 2 is used for the acquisition.

Lawson developed the first wearable ophthalmoscope in a shape of a pair of glasses [92]. The camera is placed in front of one eye, while a display is placed in front of the second eye. The display is used as an active fixation target. Illumination is provided by a superluminescent diode through the temple, allowing for a full use of the pupil path.

Samaniego used a more sophisticated design with the use of a smartphone as a camera [93]. Polarization was used, together with transpupillary illumination, to avoid corneal reflection by detection with cross polarizers. Also in this case, one eye was used for acquisition and the other for fixation. Despite the better image quality with respect to what has been shown by Lawson, Samaniego's system is bulky making it unsuitable for long monitoring.

Note that both systems were designed as ophthalmoscopes for standard chronical fundus imaging and not for continuous monitoring. Indeed, both systems block the user's field of view, making it impossible to perform any task that requires access to the ambient visual field. These wearable ophthalmoscopes were not designed to be see-through. On the other hand, headworn displays for augmented reality such as Google Glass and Vuzix AR3000 Augmented Reality Smart-Glasses [94, 95] are designed as see-through. The difference between see-through devices for augmented reality and an ophthalmoscope is that the first projects an image on the retina, while the latter does just the inverse. As we will see in chapter 2, I use techniques from see-through displays to make a wearable ophthalmoscope fully see-through.

1.5 Eye tracking methods

I already mentioned in 1.3 that eye tracking can be used for analysis of the mind. Another major application of eye tracking is in retinal imaging. Indeed, by detecting a shift in the image, it is possible to estimate the eye movement and so compensate for its effect. This is widely used in systems for fundus acquisition with exposure time longer than saccades time, such as scanning systems. Indeed, in these cases, eye motion occurring during the acquisition produces artifacts and prevent the formation of a meaningful image (see Figure 1.11).

Eye tracking can be performed with various methods. Some require a contact approach such as the measurement of the electric potential of electrodes placed near the eye [96], or the tracking of an external body attached to the eye, such as a special contact lens [97]. Other methods are non-contact and based only on imaging, such as imaging of the pupil, corneal reflection [98, 99] or fundus imaging [100, 101]. Indeed, since eye movement is approximately a rigid body rotation, it is possible

to estimate the gaze direction by observing movements either of the anterior or the posterior segment.

Some approaches which uses fundus imaging are based on SLO imaging to detect movement (such as Spectralis® OCT, Heidelberg Engineering, Germany), while others directly use full-field camera imaging (such as RTVue, Optovue Inc., USA) [100]. Since acquisition of a SLO image is, in general, slower than acquisition of a wide field image, SLO systems need to calculate shift within the single image formation, while wide field systems detect shift between consecutive images. In some cases, such as the tracking OCT module from Physical Sciences Inc., a full image is not acquired, but the system targets only a specific retinal feature (such as a vein) [100]. This can be done, for example, by scanning a circular pattern on the feature and detecting the reflection profile. With such a system, by adding a closed loop system for motion compensation, it is possible to quickly detect and compensate for eye movement up to 500 °/s [102]. Even if several techniques use an SLO system to detect eye movement, none of them has been realized for a wearable system. Such a device will be developed and analyzed in chapter 2.

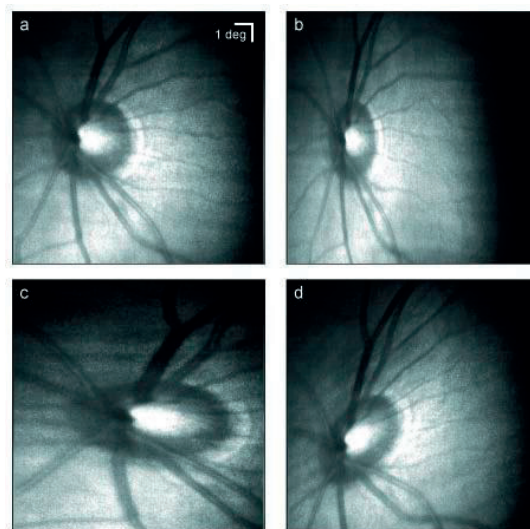


Figure 1.11

Distortions due to eye movement in image acquisition of a SLO. Courtesy of Hammer [101]

1.6 Phase contrast microscopy

Phase contrast microscopy is an imaging technique that uses the phase of light to observe transparent objects without the use of contrast agents [103]. Light passing through a fully transparent

sample modulates its phase ϕ , but not in its amplitude. Such a phase, for a sample of thickness T , can be calculated from the refractive index n as:

$$\phi(x) = n(x)T \quad (1.1)$$

Where x is the spatial coordinate along the sample's plane.

This means that a plane perfectly conjugated to the object plane will show uniform intensity, and so no intensity contrast. Phase imaging techniques, thus, convert a phase change in the object plane into an intensity change in the image plane. This can be done in several different ways such as a darkfield, structured or oblique illumination [103-108]), by introducing defocus [103], by introducing absorption or phase elements in the object's Fourier plane [109-111], by interference of two beams [112, 113] or by use of non-standard detectors, such as split detectors [114] and wavefront sensors [115]. As shown by Zernike, in the case of a plane wave illuminating the sample, even just the presence of a finite aperture produces phase contrast [103]. This is due to the fact that the finite size of the pupil aperture prevents some angular frequencies from reaching the image plane, thus destroying perfect image reconstruction.

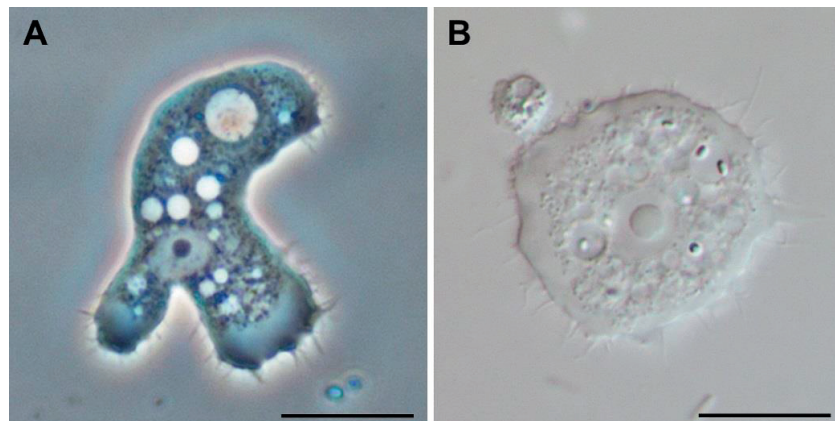


Figure 1.12

Acanthamoeba trophozoites with the characteristic acanthopodia (A) in phase contrast, (B) in bright field microscopy. Scale bar: 10 μm . Courtesy of Dr. Lorenzo-Morales.

The phase contrast techniques above can be either quantitative or non-quantitative. For example, Zernike phase contrast is not quantitative, meaning it cannot provide the object's phase value, but is useful for displaying contrast in the image. Techniques with such a characteristic are said to provide "qualitative phase contrast," [116] while microscopy techniques that provide an absolute value of the phase and are said to be "quantitative." For the sake of clarity, I will introduce

also the term “quasi-quantitative.” This represents the phase images where the final image is proportional to the original refractive index profile, but the proportionality constant is unknown. Alternatively, it is possible to see quasi-quantitative imaging as a method that provides a quantitative phase image but in arbitrary units (see Figure 1.13).

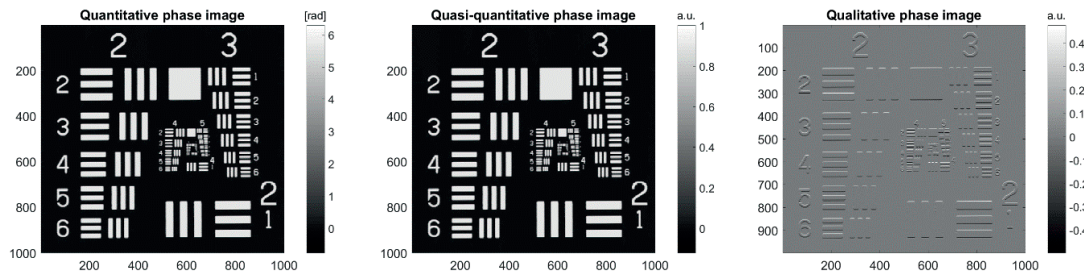


Figure 1.13

Left) Simulation of a quantitative phase image (or ground truth) of a resolution target. Center) quasi-quantitative image. It is possible to see how its appearance is identical to the quantitative case, however, the real phase is unknown. Right) Qualitative phase image of the same target. Even if the image appearance is different from the previous one, it is still possible to recognize the original pattern. Also in this case the phase values are unknown.

At the moment, the most common phase contrast techniques in biological research are Zernike’s phase contrast (ZPC) and differential interference contrast (DIC) [117]. ZPC uses a phase plate in the Fourier plane to introduce a phase shift in the light diffracted by the sample. This has been shown by Zernike to improve phase contrast in the image plane [103, 110].

DIC images requires the interference of two slightly shifted coherent beams with normal polarization. This is obtained by the use of a birefringent medium such as a Wollaston prism. In this way each beam, after passing through the sample, exhibit a slightly different phase modulation. When the two beams are then recombined together in the image plane, the path difference between the two results in intensity modulation [113]. Due to the differential nature of such a method, the resulting image is similar to what shown in the qualitative image of Figure 1.13. Both in Zernike’s method and in DIC, the transformation from phase to intensity is due to interference.

Another technique, which is not based on interference to transform phase variation into intensity variation was introduced by Mehta [108] and developed by Tian [105, 106]. In this technique, asymmetrical incoherent illumination is shined through a sample. Such an illumination, together with a finite pupil aperture, has shown to provide qualitative phase contrast in the image plane resulting in images similar to DIC. Tian developed a mathematical model in the case of the weak

object approximation (WOA) to obtain a quantitative value for the phase variation. With the WOA, phase contrast in the image plane can be roughly approximated to the partial derivative of the phase profile. So, by recording at least 4 images obtained with 4 different illumination profiles, it is possible to reconstruct the original object's phase. The mathematical details of such a technique are discussed in chapter 3. The WOA is the assumption used in this thesis to provide quantitative phase imaging of the retina.

Parthasarathy showed that by splitting the pupil plane in four, it is possible to produce four different phase contrast images in a single shot [118, 109]. Furthermore, by the information collected in the four images it is possible to reconstruct a quantitative phase image. The drawback is a reduction of the spatial resolution.

All the previous mentioned techniques for phase contrast have been developed for a transmission configuration, which is in most cases not appropriate for in-vivo imaging. In 2012, Ford showed how light backscattered from the deep layers of a thick scattering media can be used to provide phase contrast on the top layers [119, 120]. In the case of fundus imaging, the retina is a thick transparent media on top of a strongly backscattering layer (RPE). In chapter 3, I will make use of the backscattering light from the RPE to provide an effective transmission configuration for the transparent layers above.

1.6.1 Label free cellular contrast in the eye

In section 1.2, I discussed how microscopic structural changes in the eye could be used for early diagnose of eye pathology. However, in-vivo imaging of many retinal cellular structures (such as ganglion cells) is still invasive or time consuming [54, 10]. Because of that, research efforts are being dedicated to develop novel techniques for observing cellular structures in the retina.

One of these techniques is based on a confocal scanning system and a split detector. It consists of two separate detectors on which half of the incoming beam is sent. This asymmetry in the image plane which is equivalent to asymmetric illumination in the object plane [108]. By subtracting the power measured on the two detectors, it is possible to enhance contrast of high frequency features and observe retinal microvasculature [121-124].

Another technique is based on the introduction of an offset in the aperture of a confocal scanning ophthalmoscope [125, 126]. Such a technique suppresses the backreflected signal and

collects the backdiffracted one. This technique allowed for the in-vivo observation of ganglion cells in monkeys [127].

Recently, OCT coupled with adaptive optics was used to obtain high resolution images of the retina [10]. It was shown that organelles inside ganglion cells move and thus change the detected speckle pattern since the illumination is coherent. By averaging several images collected over a time span of about 10 minutes, on a patient with the head stabilized by a bite bar, it was possible to obtain an image of ganglion cell's somas. Despite the good quality of the images, the technique is fundamentally limited by the speed of organelles motility (see Figure 1.14). For clinical application, a fast acquisition (<30 sec) is required, especially in the case of patients with difficulties in fixating a target.

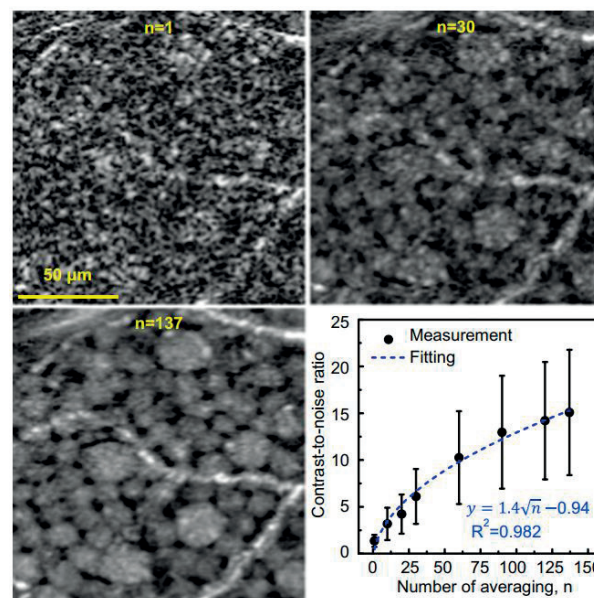


Figure 1.14

Averaging of en face images obtained with an adaptive optics OCT system. For high number of averages, it is possible to distinguish ganglion cell's somas. Courtesy of Miller [10].

1.7 Alternative to transpupillary illumination

Imaging of the eye fundus requires an external light source for illuminating the imaging area. In standard ophthalmoscopy light is transmitted through the pupil since is the only transparent opening. However, transpupillary illumination generates also strong reflections at the different eye interfaces, and especially the interface between air and cornea. This is due to the large abrupt change in the refractive index. Such a problem has been solved either by using part of the pupil for

illumination and the other for collection or by means of polarization [71, 93]. Indeed, if a polarized beam is sent to the eye, the backreflected light preserves the polarization state, while light backscattered from the eye fundus shows random polarization. By using a polarizer in the collection path, it is possible to mitigate the reflection. An alternative solution is to avoid light transmission through the pupil and transmit it through sclera [129-132], through the eyelid [133] or through the temple [92]. The first two are respectively called transscleral and transpalpebral illumination. Illumination through the pupil is usually called transpupillary illumination.

Transscleral and transpalpebral illumination are particularly used in eye surgery because they provide uniform illumination over a large area and because they allow to use the entire pupil for fundus observation (i.e. without reflections or scattering from the anterior segment). For the same reason, it has also been used in large field of view fundus cameras [129, 133]. Another interesting feature is the reduction of the reflection at the vitreous-retina interface, which can mask underlying features. Indeed, transscleral illumination has been successfully used in imaging eye tumors [129-131] which are easily masked in images acquired by standard retinal camera. A main limitation of these illumination techniques comes from the fact that the light illuminating the entire eye is also passing through the retina in a localized area. This produces a high intensity spot that limits the maximum possible exposure (see Figure 1.15).

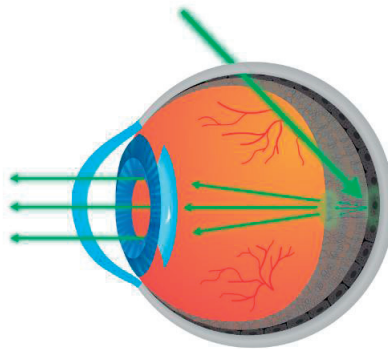


Figure 1.15

Scheme of transscleral illumination.

Light transmission through the sclera is strongly affected by the abundance of pigment in the choroid and the RPE. However, no significant differences in eye pigmentation have been observed between different gender, eye color and skin color [21, 22].

An interesting property of transscleral and transpalpebral illumination is that it provides angled illumination of the retina. Due to the geometry of the eye and the eyelids, transscleral illumination is possible only on one axis (left-right) and transpalpebral on the perpendicular axis (top-down). Indeed, the normal aperture of the eye lid is almost the same size of the iris [134], leaving almost no space for transscleral illumination on top or bottom of the eye.

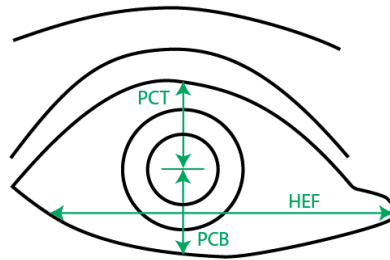


Figure 1.16

Scheme of the eye proposed by Bosch [134]. In his studies, the lateral eye opening (HEF) ranges between 22 and 30 mm. The distance from the pupil center to the top (PCT) ranges between 2 and 5 mm and the distance to the bottom (PCB) ranges between 4 and 6.

Illumination through the temple has also been used by Lawson [92]. However, probably due to the thickness of the tissue and consequent scarcity of light, the final image quality appears to be poor in quality. It is important also to say that such a technique has not been fully analyzed yet, and that for an application in clinical studies safety conditions should be analyzed.

1.8 Structure of the thesis

The previous sections provide the background needed for understanding the following chapters. As previously mentioned, this thesis will focus on two distinct challenges in the field of ophthalmology.

The first one regards the development of a see-through wearable ophthalmoscope and it will be discussed in chapter 2. I will cover the setup working principle up to the proof of principle validation on resolution target and an ex-vivo human eye. The motivation for such a research stems from the possibility of accessing, on demand, general health from eye imaging, as discussed in section 1.2.

The second challenge regards the observation of transparent cellular bodies in the living retina in a time frame compatible with standard ophthalmic systems. This is crucial for early diagnosis of diseases discussed in 1.2. Due to its complexity, this topic will be divided into three different

chapters. Chapter 3 will focus on the proposed technique and on what affects the phase contrast in the raw images. Phase contrast in the raw images is still qualitative (i.e. it does not represent the real phase profile). In chapter 4, I will discuss how quantitative images can be obtained from the qualitative one. Finally, in chapter 5 I will talk about the challenges that need to be faced to apply this technique to the in-vivo case.

Chapter 6 will be used to summarize the key notions that have been presented in the thesis. Especially, I will point out what are the main results that I achieved in this research. Finally, I will also explain what I think will be the future steps to keep exploring this field.

Chapter 2 A wearable see-through ophthalmoscope

With the miniaturization of scanning mirrors and the emergence of wearable health monitoring devices, an intriguing step is to investigate the potential of a LSO for retinal imaging with wearable glasses (see section 1.4.2). In addition to providing morphological information of the retina, such as vasculature, LSO images could also be used to provide information on general health condition. A compact eyeglass with LSO capability would give access, on demand, to retinal parameters without disturbing the subject's activity. One of the main challenges in this field is the creation of a device that does not interrupt the user's field of view.

In this chapter, I report, to my knowledge, the first see-through ophthalmoscope. Such a system is based on the works of Tidwell and Guillaumée's on headworn display [135, 136]. Tidwell's pioneering work showed that it is possible to produce an image on the retina by raster scanning a laser beam on it. Guillaumée used a thick holographic plate to diffract the scanned beam into the eye while letting through vision unaffected. Indeed, the angle and wavelength selectivity of the holographic plate allowed all the other rays to pass through the grating almost unperturbed and so providing see-through.

The system design, will be illustrated in section 2.1. In section 2.2, I will discuss geometrical considerations. The system will be analyzed with 3D ray tracing simulations in section 2.3 and then tested in a proof of concept setup with the same key-parameters of a wearable device in section 2.4. In section 2.4, image quality will be analyzed by acquiring images of a resolution target and of an ex-vivo human eye sample. Conclusions and final discussion on such a system are written in section 2.5.

This chapter is based on the following peer reviewed research article: D. Carpentras, C. Moser, *See-through ophthalmoscope for retinal imaging*, J. Biomed. Opt. 22(5), 056006, 2017.

2.1 Optical design

In the presented setup (see Figure 2.1), the laser beam is brought by a single mode optical fiber followed by a polarizer. After passing through a polarizing beam splitter (PBS), the beam is directed on a single 2D micromirror's surface. The beam is scanned on the volume hologram's surface by

rotating the micromirror, which is then diffracted towards the eye lens and then focused on the retina. At the latter surface, light is scattered back with mixed polarizations and travels back to the PBS. The part of the scattered beam having a polarization perpendicular to the original one is selected by reflection off a polarizing beam splitter in a new path. This light is focused into a multimode fiber, which brings the signal to a photodetector. The rejection of light with the same polarization as the source beam suppresses the background noise generated by multiple reflections at the interfaces.

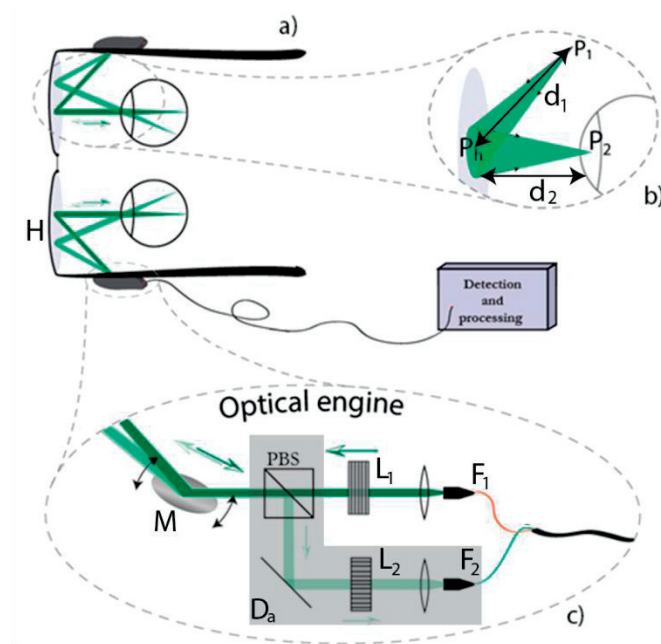


Figure 2.1

a) Concept for retinal imaging with a wearable, see-through ophthalmoscope. Laser light is scanned by a micromirror (M) on the eye, thanks to diffraction from a holographic grating (H). Backscattered light from the eye fundus is then confocally collected and sent to a photodetector for acquisition (box “detection and processing”). b) The hologram is made with 2 spherical waves whose centers are located at the pupil plane (P2) and the micromirror (P1) respectively. d_1 is the distance between the micromirror and the hologram’s center, while d_2 is the distance between hologram’s center and the center of the pupil. c) Expanded view of the optical engine. Light enters the system through the fiber F1 and it becomes vertically polarized passing through the linear polarizer L1. The backscattered beam is collected in the detection arm Da where the horizontally polarized light is collected by the polarizing beam splitter PBS, filtered by the polarizer L2 and collected by the optical fiber F2. Polarization optics is used to suppress light reflections at interfaces.

The detection system is not included in Tidwell’s original work, and particular care should be dedicated to make it compact for wearability. To keep the eyewear as light as possible, source and detection are kept separate from the optical engine and connected by optical fibers. Indeed, with current technology for lenses, polarizers and micromirrors, the optical engine can be made compact

and light. Sensitive photodetectors are in general bulkier, so we chose to separate them from the eyewear by providing optical connection via optical fibers. Sensitive optical detectors with a limited size are commercially available (e.g. micro PMT photon counting head H12406 Series from Hamamatsu $38 \times 30 \times 15 \text{ mm}^3$ and attached to a voltage driver of size $22 \times 15 \times 6 \text{ mm}^3$). This means that the detection box can be shrunk down to almost the size of a smartphone (few cubic centimeters), making this box wearable in a pocket.

2.2 Geometrical considerations

The see-through hologram presented in figure 2.1b is recorded in such a way that a diverging beam coming from the micromirror is diffracted towards the pupil's center. In order to model imaging, I approximate the hologram as a spherical lens, which is mapping the plane containing P_1 into a plane containing P_2 . The magnification between the two planes is given by the ratio $M = d_1/d_2$, where d_i is the distance between the hologram's center and the point P_i . In this way, I can consider the micromirror as an aperture at the eye pupil's plane of size $D_a = D_m d_1/d_2$, where D_m is the physical micromirror's diameter.

The values of d_1 and d_2 are limited by wearability constraints to the range of tens of millimeters. The choice of a small value for d_2 is appealing since it provides a bigger aperture at the pupil's plane, and so more light collected. However, this choice amplifies the difference in path length for different angle of illumination which contributes to distorting the final image. It is important also to take into account that a bigger pupil's diameter will also increase the aberrations introduced by the eye. For a healthy eye (meaning almost no myopia or astigmatism), a beam diameter below 2 mm is limited by diffraction and high orders aberrations can be neglected [137]. Another disadvantage of a large pupil is that the hologram is designed for small beam diameter, making the diffraction efficiency decreases rapidly when the impinging beam becomes large (figure 2.4d).

It is important to notice also that the choice of the geometrical parameters affects also the maximum achievable field of view (FOV). Indeed, in the paraxial approximation I consider the linear FOV equal to $\theta d_1/d_2$, where θ is the micromirror's scan range. However, having a big FOV is not a stringent requirement for the device, since the main goal is to track small features. From these considerations and aiming for a flexible setup, I chose to place both pupil and micromirror at 30 mm from the plane of the hologram, thus yielding $d_1 = 30 \text{ mm}$ and $d_2 = 30\sqrt{2} \text{ mm}$.

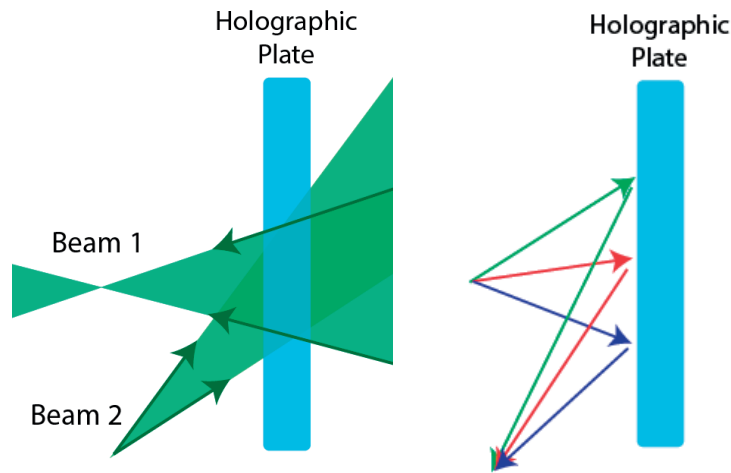


Figure 2.2

Left) Scheme used for recording the setup. Two beams interfere at the plane of the holographic plate.
 Right) By shining the holographic plate with a really small beam (approximated as a ray) the beam is diffracted on the same path used for recording.

2.3 Ray tracing simulations

In order to take into account, the effect of the hologram on the retinal image resolution, I simulated the system by 3D ray-tracing using MATLAB®. All lenses (including the eye lens) have been considered in the paraxial approximation and the curvature of the eye fundus has been included in this study. The eye lens has been modeled with a focal distance of 17 mm [15] and the rays scattered from the eye fundus are generated following Lambert's cosine law [138]. Part of the rays back scattered from the retina is stopped by the eye pupil, while the other part is collected by the eye lens and collimated towards the hologram. Here, the hologram diffraction efficiency has been obtained by the use of Kogelnik's theory [139], while the direction of the diffracted ray is estimated from Heifetz et al. [140]. It is important to take into account that the hologram is recorded for a diverging beam, while the illumination used in the scanning system is a collimated beam. This means that part of the beam is not Bragg matched with the holographic grating, reducing the diffraction efficiency (see figure 2.3). Because of that simulations have been used to estimate the diffraction efficiency of a collimated beam depending on its diameter (as shown in figure 2.4b). In the graph, it is possible to observe how the diffraction efficiency is almost maximal for beams whose diameter is smaller than 1.5 mm. Above this value part of the beam is mismatched respect to the grating and so the efficiency decreases with increasing beam's diameter.

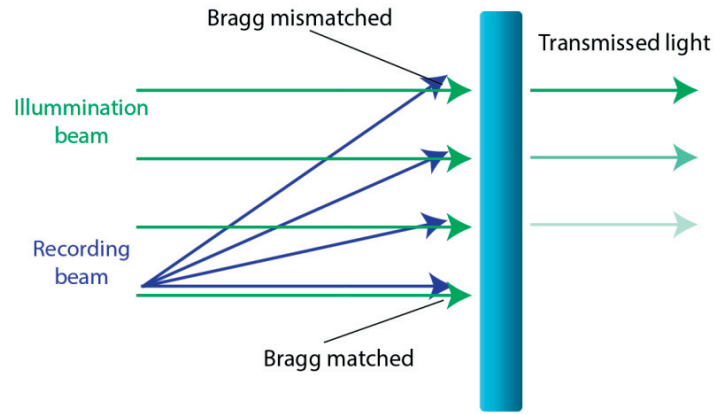


Figure 2.3

Diffraction efficiency for a collimated beam (green rays). In the areas where the illumination angle is close to the recording angle the light is Bragg matched. This means that the light is diffracted and so, ideally, there is no transmitted light. The bigger the angle difference between illumination and recording, the bigger is the angle mismatch, and so also the transmitted light.

Beam diffraction is such that the beam is focused at a distance d_f , which is different for each spatial location on the hologram (Figure 2.4c). After the focal point, the beam diverges and only a fraction of it is collected by the micromirror. The collected light is then collimated by the scan lens (not shown in Figure 2.1) and focused by a lens (Figure 2.1 c) on the multimode fiber acting as a pinhole.

Spatial resolution is estimated by computing the light collection from different retinal points without changing the micromirror's angle for a pinhole of 1 Airy unit. Resolution is calculated from the curve's full width half maximum (FWHM) as $FWHM/0.84$ [76]. In this way I obtain a lateral resolution of $12\ \mu m$ and an axial resolution of $\sim 500\ \mu m$, which is larger than the retina thickness. Since the targeted applications are based on 2D imaging of the fundus, depth selectivity is not required. This simulation has been performed only at the center of the eye and it should be repeated for different illumination direction. The experimental results (see section 3) showed a similar value for lateral resolution across the entire field of view. A diffraction limited system would produce an $8\ \mu m$ spot at the retina and, for a confocal system, an optical resolution of $5\ \mu m$. In the simulations, all the optics have been modeled as ideal, thus the hologram is responsible for the aberration leading to a higher lateral resolution.

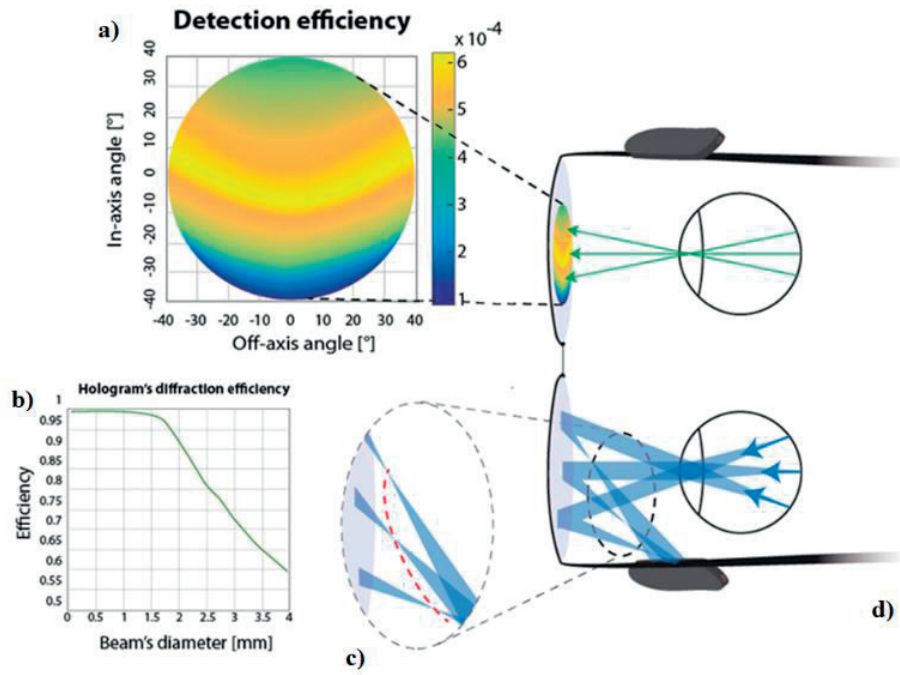


Figure 2.4

a) Detection efficiency (in light collected in the multimode fiber) for different areas of the hologram. The graph shows more sensitivity for in-plane rays. b) Hologram's diffraction efficiency for different beam's size. The efficiency is almost constant up to 1.5 mm, with a rapid decrease thereafter. c) Focusing effect of the hologram. The dashed red line is the place where the focal points lay. Their different distance to the micromirror is the main cause for the non-uniformity in the collection efficiency. d) Illustration on the eyewear.

Due to the system asymmetry, there is a variation in collected backscattered power from different areas of the eye resulting in a non-uniform reconstructed image. Figure 2.4 b illustrates this effect. Simulation shows that the power collected by the pinhole is more sensitive for in-plane beams and almost negligible for out of plane beams. The origin of this effect lies in the position of the focal point of the diffracted beam which varies along the surface of the hologram (dashed red line in Figure 2.4 c). For in-plane rays, the focal distance is different for each source point, resulting in a different beam size at the micromirror. This produces relevant changes in the amount of collected light.

By analyzing the power budget along the return path, simulation shows that only 1.4 % of scattered light from the retina is collected by a 4 mm eye pupil, which is furthermore decreased to 0.8 % due to the hologram's efficiency (60%). The micromirror further decreases this fraction to 0.17 %.

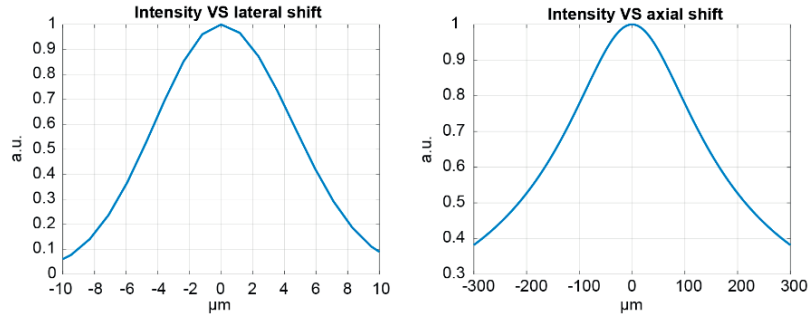


Figure 2.5

Left) Signal's intensity versus lateral shift. Right) Signal intensity versus axial shift.

2.4 Experimental results

To validate the system, I realized a proof of concept setup on a breadboard. Relative distances between the micromirror, the hologram and the eye are chosen according to the previous section, and so equal to a wearable setup. Miniaturization has not been attempted on the other components in the detection path.

The micromirror chosen for the setup is a 2D scanning mirror by Hamamatsu (S13124-01M) with a scan angle of $\pm 7^\circ$, 2 mm diameter of reflective area and resonant frequencies of 1000 and 350 Hz on the two axes. The system can be used either in resonance or linear mode. The resonance mode allows for high line scan frequency (1 kHz per line), improving also the frame rate, but it provides almost no control on the mirror's position over time. This means that the data from the scan are acquired but it is not possible to place each value at the corresponding pixel. The linear mode requires a scanning frequency smaller than the resonance frequency (150 Hz used in the following). This mode provides a complete control of the micromirror point by point. As a general rule, I could say that the smaller the frequency, the higher the precision of the micromirror angular position, even if some specific frequency could still excite resonance modes introducing image distortions. After testing several frequencies for scanning the micromirror, I found 150Hz to be a good value for the line frequency.

The frame rate can be obtained as the scanning frequency divided by the number of lines. Because of this, a tradeoff should be found between FOV and frame rate. Table 2.1 shows different scanning choice that allows either a large FOV or a fast scan. However, it is clear the imaging frame rate is limited up to ~ 15 Hz, which is not fast enough for eye tracking.

An increase in speed is possible by reducing the FOV (e.g. single features) and using circular scanning [101, 102]. In this technique the laser is scanned in a circle like fashion, providing a linear profile instead of a 2D one. This technique is well suited for features tracking but it cannot be used for imaging. The software provided with the micromirror supports also circular scan that can be used at 150 Hz producing a circle at the retina of diameter of $500\ \mu m$.

Another important consideration regards the maximum achievable FOV with this micro-mirror. A micromirror scan angle of $\pm 7^\circ$ corresponds to almost a $6 \times 6\ mm^2$ FOV on the retina. However, for large angles, the micromirror behaves non-linearly yielding distortions in the final image. Because of that, I preferred to limit the FOV to a maximum of $4 \times 4\ mm^2$.

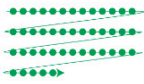
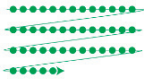
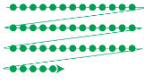
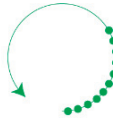
Mode	Number of pixels	Spacing between points	Repetition rate	FOV
Raster scan 	500 x 500	$8\ \mu m$	0.3 Hz	$4 \times 4\ mm^2$
Raster scan 	100 x 100	$15\ \mu m$	1.5 Hz	$1.5 \times 1.5\ mm^2$
Raster scan 	10 x 100	$15\ \mu m$	15 Hz	$150 \times 1500\ \mu m^2$
Circular mode 	196	$8\ \mu m$	150 Hz	Circle of diameter $500\ \mu m$

Table 2.1

Comparison between different scanning techniques. The scanning mode can be raster scanning or circular mode. The number of pixels, together with the spacing between adjacent points determines the FOV. While the number of lines determines the repetition rate (that in a raster scan is the frame rate.) To prevent distortions due to resonance the line frequency has been fixed to 150 Hz.

The hologram is fabricated by interference using a $532\ nm$ single frequency laser (model MSL FN 532 from CNI) used to activate a thin photopolymer layer ($16\ \mu m$) and change its refractive index. The laser light is split in two beams (reference and object beam). The reference beam is a spherical wave centered at P_1 that propagates to the photopolymer. The object beam is also a

spherical beam that travels from the photopolymer to its focal point P_2 . The photopolymer exposure generates a change in the index of refraction of 0.03. The photopolymer is a $16\ \mu\text{m}$ film of Bayfol® HX200 by Covestro. The photodiode used for acquisition is an APD410A2/M by Thorlabs.

A USAF chart is used for testing the system's resolution. An ex-vivo eye sample is used to obtain images of the fundus. The human eye has been fixed with a solution of paraformaldehyde and cut in half, in order to remove the eye lens. This last step was required because the ex-vivo eye lens does not have the correct focal distance, probably due to after death process and fixation effects.

Figure 2.6 has been obtained with a USAF chart as the sample. The obtained resolutions are $14\ \mu\text{m}$ for the horizontal axis and a $16\ \mu\text{m}$ for the vertical axis. This has been obtained on a 500×500 pixels image of size $2 \times 2\ \text{mm}^2$. The image was acquired in approximately 3 seconds. Different acquisition speeds have been tested for the micromirror without noticing any significant decrease in the image properties as long as the scanning frequency is not close to the resonant frequency. For high speed acquisition near resonance, image distortions are present due to excitation of the mirror's resonant modes.

In case of a commercial device, eye security has to be taken into account also in the case of a mirror's failure. In case of visible light, I calculate the maximum exposure for a time of 0.25 s, which is the eye reaction time to visual disturbance (such as a bright spot). For infrared radiation this is not possible anymore, because the user is not able to see the radiation and the exposure time could be arbitrary long. However, many possible techniques can be implemented to check the correct functioning of the device, such as a feedback system or a control on the acquired data. Because of that I estimated a maximum exposure time of 10 s for infrared. From these considerations I obtain a limit of $980\ \mu\text{W}$ for a $515\ \text{nm}$ beam, and $617\ \mu\text{W}$ in case of an $800\ \text{nm}$ radiation [141].

Due to the maximum limit of power and signal reduction, noise should also be taken into account. The signal's power (for the following experiment: $300\ \mu\text{W}$), should be multiplied by the collection's efficiency ($\sim 6 \cdot 10^{-4}$) and by the retina's reflectivity ($\sim 5\%$). The sensor has a responsivity of $\sim 20\ \text{A/W}$ (giving a current of $180\ \text{nA}$) and a transimpedance gain of $250\ \text{kV/A}$, leading to a conversion gain of $\sim 5\ \text{MV/W}$ (and so a voltage of $45\ \text{mV}$). By using a resistance of $50\ \Omega$, I obtain a power of $40\ \mu\text{W}$. Since the noise equivalent power (NEP) is $0.09\ \text{pW}/\sqrt{\text{Hz}}$, then for $150\ \text{kHz}$ I obtain $35\ \text{pW}$, which is negligible compared to the signal's power.

Shot noise should also be taken into account. The shot noise contribution from the current can be calculated as $\sqrt{2|q_e|fI_{DC}}$, where q_e is the electron's charge, I_{DC} the temporal average of the photocurrent and f the acquisition frequency. From this formula, I obtain a contribution of 90 pA, which is more than three orders of magnitude smaller than the 180 nA of the signal's current.

An image of an ex-vivo human eye has been acquired with a field of view of about $4 \times 4 \text{ mm}^2$. With an incident signal power of $300 \mu\text{W}$ at 532 nm. All the images have been renormalized following the intensity inhomogeneity presented in Figure 2.4. The obtained image quality allows us to observe major structures such as blood vessels.

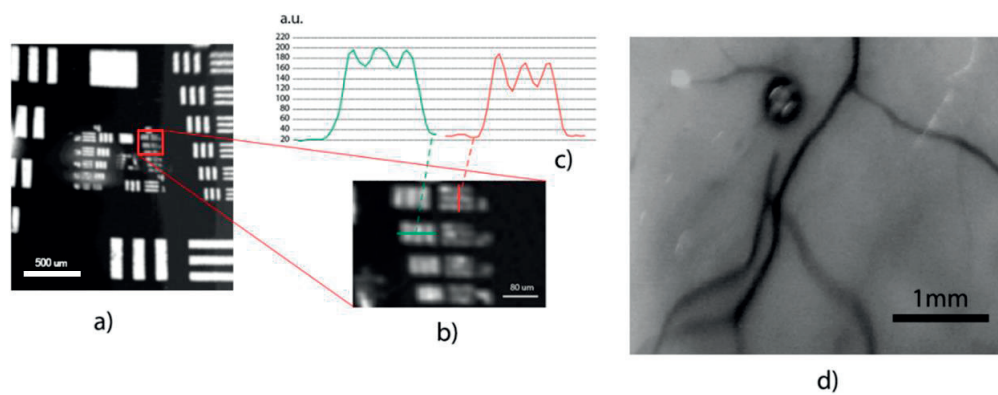


Figure 2.6

a) Image of a USAF resolution target with the see-through system of figure 2.1, with b) zoomed area. c) Intensity cross section of the resolvable features. d) Image of an ex-vivo human retinal sample. It is possible to distinguish clearly some retinal blood vessels. The black spot is supposed to be an air bubble due to sample degradation. All the images have been acquired with a single scan. No average has been performed

2.5 Conclusions

I have presented the proof of concept of the first see-through ophthalmoscope. The system has been designed for a fundus acquisition without disturbing the user's activity for applications such as health monitoring and eye tracking. The optical engine has been realized in a compact structure using the same sizes and distances as a wearable setup.

The measured imaging resolution is $16 \mu\text{m} \times 14 \mu\text{m} (x, y)$ in agreement with 3D simulations. The system is not diffraction limited because of distortions caused by the hologram. A 500×500 pixel image of the retina of an ex-vivo eye sample was obtained in 3 seconds. The acquired images showed good contrast of the vasculature, which is potentially interesting for eye tracking and monitoring applications using the vasculature. The acquisition speed in the current

work was not optimized. The use of a resonant scanning mirror, such as the 8 kHz scanning mirror used by Hammer et al. [101], would improve the acquisition speed making the system suitable for in-vivo applications. The polymeric material used in this article is sensitive only to wavelengths in the visible range, but if a complete disturbance-free device is needed an infrared source should be chosen.

Chapter 3 Phase contrast imaging of retina

As discussed in chapter 1, the observation of retinal cellular structures is fundamental to study and detect eye pathologies at early stages. However, except for rods and cones, most of the retinal microstructures are weakly reflective and thus difficult to image *en face*, especially in a time frame compatible to medical screening [10].

In chapters 3 to 5, I will discuss different aspects of how, light backscattered from the eye fundus can be used to obtain a phase image of the retina. Specifically, chapter 3 will be dedicated to the connection between phase contrast and the spatial profile of the backscattered light. In chapter 4, I will discuss the process of reconstructing a quantitative phase image out of a set of qualitative phase images, while in chapter 5, I will discuss the challenges for in-vivo imaging.

In section 3.1 of this chapter, I will use Tian's image formation theory to show how the shape of the backscattered light affects the contrast. In section 3.2, I will use Monte Carlo simulations to estimate the backscattering spatial profile off the choroid and RPE, and then I will use simulations, based on Tian's theory, to estimate properties of the resulting phase image. Section 3.3 will be dedicated to experimental validation on a human eye sample, while in section 3.4, I will draw my conclusions on this chapter.

This chapter contains work from the article: "The effect of backscattering in phase contrast imaging of the retina," D. Carpentras, T. Laforest, M. Künzi, C. Moser, Optics Express, 2018.

3.1 Theory

3.1.1 General theory

The model of image formation for an asymmetric illumination has been initially developed by Mehta and Sheppard [108]. A more detailed analysis has then been proposed later by Tian [105].

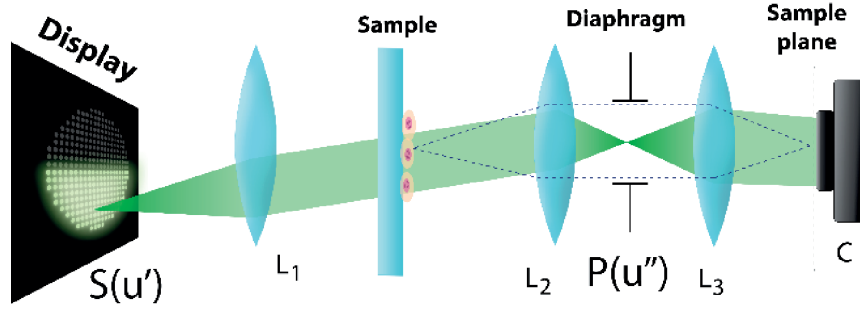


Figure 3.1

Transmission setup (from [105]) for phase contrast obtained through oblique illumination. The system consists of a display of LEDs used to illuminate a sample. The display plane is conjugated to the diaphragm plane, while the sample plane is conjugated to the camera plane. The sample plane lays in the Fourier plane of the display.

The suggested setup is shown in Figure 3.1, where a transmission illumination system is shown. The setup is that of a standard microscope, except for the fact that the illumination might not be asymmetric. The illumination source $S(\mathbf{u}')$ is composed of an array of light emitting diodes (LEDs). Each source is incoherent with respect to the others. Then, the image at the camera plane result from the intensity superposition integral [105]:

$$I_{[S,P]}(\mathbf{x}_c) = \iint \left| \iiint \left\{ [Q(\mathbf{x})O(\mathbf{x})] \exp[-j(\mathbf{x} \cdot \mathbf{u}'')] d^2\mathbf{x} \right\} P(\mathbf{u}'') \exp[-j(\mathbf{x}_c \cdot \mathbf{u}'')] d^2\mathbf{u}'' \right|^2 d^2\mathbf{u}'' \quad (3.1)$$

Where $I_{[S,P]}(\mathbf{x}_c)$ is the image function, \mathbf{x}_c is the spatial coordinate of the image plane, P is the pupil function, O is the object function, \mathbf{x} the spatial coordinate at the object plane, \mathbf{u}'' the spatial coordinate at the Fourier plane and $Q(\mathbf{x})$ represents the propagation of plane waves from the display plane to the sample plane:

$$Q(\mathbf{x}) = \sqrt{S(\mathbf{u}')} \exp(j\mathbf{u}' \cdot \mathbf{x}) \quad (3.2)$$

For each function, I am placing the spatial coordinates between round brackets (\sim) and other functions or parameters that can affect the function as a subscript. For more details on the used notation, please, read the section “Symbols and notation.”

Successively, Tian linearized equation (3.1) by the use of the weak object approximation (WOA) [105, 142]. This approximation considers the absorption $\mu(\mathbf{x})$ and the phase $\phi(\mathbf{x})$ term of

the object $O(\mathbf{x}) = e^{-\mu(\mathbf{x}) + j\phi(\mathbf{x})}$ as smaller than 1. Thus, by approximating the object function as $O(\mathbf{x}) \sim 1 - \mu(\mathbf{x}) + j\phi(\mathbf{x})$ it is possible to write the image as:

$$\hat{I}_{[S,P]}(\mathbf{u}) = B_{[S,P]}\delta(\mathbf{u}) + H_{[S,P]}(\mathbf{u})\tilde{\mu}(\mathbf{u}) + G_{[S,P]}(\mathbf{u})\tilde{\phi}(\mathbf{u}) \quad (3.3)$$

Where the hat “ \sim ” represents the Fourier transform (FT), B is a scalar value representing the average Intensity at the camera, $\delta(\mathbf{u})$ is the Dirac’s delta function, H is the weak object transfer function (WOTF) of the absorption function and G is the WOTF of the phase function. These last three terms can be obtained, in case of an aberration-free system, as:

$$\begin{cases} B_{[S,P]} = \iint S(\mathbf{u}')|P(\mathbf{u}')|^2 d^2\mathbf{u}' \\ H_{[S,P]}(\mathbf{u}) = -\iint S(\mathbf{u}')[P(\mathbf{u}')P(\mathbf{u}' - \mathbf{u}) + P(-\mathbf{u}')P(\mathbf{u}' + \mathbf{u})]d^2\mathbf{u}' \\ G_{[S,P]}(\mathbf{u}) = j\iint S(\mathbf{u}')[P(\mathbf{u}')P(\mathbf{u}' - \mathbf{u}) - P(-\mathbf{u}')P(\mathbf{u}' + \mathbf{u})]d^2\mathbf{u}' \end{cases} \quad (3.4)$$

This form is more convenient than the original one expressed in (3.1) since it expresses the relationship between phase and the final image as a linear system. This allows for the analysis of the system transfer function, similarly to what is commonly done for the modulation transfer function (MTF) and point spread function (PSF).

Another interesting result from (3.4) is the link between B and H :

$$H_{[S,P]}(0) = 2B_{[S,P]} \quad (3.5)$$

From now on, I will further develop Tian’s model to understand how the illumination function affects the transfer functions.

From (3.4) we can obtain how different part of the illumination function affect the transfer functions. Indeed, by taking an even and real pupil function (i.e. $P(-\mathbf{u}') = P(\mathbf{u}') = \text{Real}[P(\mathbf{u}')]])$ and by decomposing the illumination function into its even and odd part as: $S(\mathbf{u}') = S_{ev}(\mathbf{u}') + S_{odd}(\mathbf{u}')$ we obtain:

$$\begin{cases} B_{[S_{ev},P]} = \iint S_{ev}(\mathbf{u}')|P(\mathbf{u}')|^2 d^2\mathbf{u}' \\ H_{[S_{ev},P]}(\mathbf{u}) = -2\iint S_{ev}(\mathbf{u}') P(\mathbf{u}')P(\mathbf{u} - \mathbf{u}') d^2\mathbf{u}' \\ G_{[S_{odd},P]}(\mathbf{u}) = 2j\iint S_{odd}(\mathbf{u}')P(\mathbf{u}')P(\mathbf{u} - \mathbf{u}') d^2\mathbf{u}' \end{cases} \quad (3.6)$$

Here, one observes that H (and consequently also B) is not affected by the odd part of the illumination function and that G does not depend on the even part. For future discussion it is convenient to introduce the normalized transfer functions h and g as:

$$\begin{cases} h_{[S_{ev},P]}(\mathbf{u}) \triangleq \frac{H_{[S_{ev},P]}(\mathbf{u})}{B_{[S_{ev},P]}} \\ g_{[S,P]}(\mathbf{u}) \triangleq \frac{G_{[S_{odd},P]}(\mathbf{u})}{B_{[S_{ev},P]}} \end{cases} \quad (3.7)$$

In this way, I can introduce the normalized image function J as:

$$\hat{J}_{[S,P]}(\mathbf{u}) \triangleq \frac{\hat{I}_{[S_{ev},P]}(\mathbf{u})}{B_{[S_{ev},P]}} = \delta(\mathbf{u}) + h_{[S_{ev},P]}(\mathbf{u})\hat{\mu}(\mathbf{u}) + g_{[S,P]}(\mathbf{u})\hat{\phi}(\mathbf{u}) \quad (3.8)$$

Such an expression is convenient for future analysis, since it provides a constant background normalized to 1 for every image. In this way, the amplitude of h and g are directly linked to the contrast. Indeed, doubling the g amplitude of g , in case of no variation on ϕ , implies also doubling the phase contrast. This is not the case for G function.

It is also interesting to notice that the WOA depends on the illumination function within the pupil aperture only. Indeed, S appears only as a product with P , as $S(\mathbf{u}')P(\mathbf{u}')$. This means that the value of $S(\mathbf{u}')$ where $P(\mathbf{u}')$ is zero have no influence on the final image. This is not the case of illuminations such as in dark field, for which the direct illumination is never collected (i.e. $S(\mathbf{u}')P(\mathbf{u}') = 0$ for every \mathbf{u}').

Another remarkable fact of such an imaging modality is that the phase information is a weak signal on a background. This means that, in the raw image, the contrast would be much smaller than one, and in some cases, the desired signal could be below signal noise or below the camera's bit depth. Because of that it is relevant to find what are the key parameters that can be used to maximize the phase contrast.

3.1.2 Ramp approximation

As we will see in the next sections (3.2.1 for simulations and 3.3.2 for experimental data), in the retina it is reasonable to approximate the illumination function as a linear function. To avoid confusion with the WOA (that is also based on a linear approximation) I will call this approximation "ramp

approximation.” Furthermore, the ramp approximation will be useful to understand the key parameters that improves phase contrast.

I will now define the linear illumination function S° as:

$$S_{q,m,\varphi}^\circ(\mathbf{u}') = q + m (\mathbf{v}_\varphi \cdot \mathbf{u}') \quad (3.9)$$

Where \mathbf{u}' is the spatial frequency, q is the value for $\mathbf{u}' = 0$, m is the amplitude of the gradient, “ \cdot ” is the scalar product and \mathbf{v}_φ is the unit vector of the form $\mathbf{v}_\varphi = \cos(\varphi)\hat{\mathbf{x}} + \sin(\varphi)\hat{\mathbf{y}}$, with $\hat{\mathbf{x}}$ and $\hat{\mathbf{y}}$ being orthogonal unit vectors. Let us also consider the case of a circular pupil aperture $p'_a(\mathbf{u}')$ of radius a , such that:

$$p'_a(\mathbf{u}') \triangleq \begin{cases} 1 & \text{for } |\mathbf{u}'| < a \\ 0 & \text{otherwise} \end{cases} \quad (3.10)$$

In Appendix A, I show that, by substituting these two functions into (3.6) the following expressions for B , H and G are obtained:

$$\begin{cases} B_{q,a}^\circ = qa^2\pi \\ H_{q,a}^\circ(\mathbf{u}) = -2qa^2h'\left(\frac{\mathbf{u}}{a}\right) \\ G_{m,a,\varphi}^\circ(a\mathbf{u}) = 2jma^3g'_\varphi\left(\frac{\mathbf{u}}{a}\right) \end{cases} \quad (3.11)$$

Where the circle on B , H and G is used to show that they have been obtained with the ramp approximation, h' is a function which depends only on the spatial frequency coordinate and g'_φ depends on both φ and the spatial frequency coordinate (more details in Appendix A). To be more precise, the only effect of φ is a rotation of the function g'_φ . It is also important to notice that the effect of q and m is a linear modulation of the amplitude of H and G . Instead, a produces both a modulation and a rescaling of the spatial frequency coordinate.

In order to simplify the normalized transfer functions, it is then convenient to introduce the ratio of m and q as:

$$r \triangleq \frac{m}{q} \quad (3.12)$$

By substituting this into (3.11) I obtain h° and g° as:

$$\left\{ \begin{array}{l} \frac{H_{q,a}^\circ(\mathbf{u})}{B_{q,a}} = \frac{-2}{\pi} h' \left(\frac{\mathbf{u}}{a} \right) = h_a^\circ(\mathbf{u}) \\ \frac{G_{m,a,\varphi}^\circ(\mathbf{u})}{B_{q,a}} = r a \frac{2j}{\pi} g' \left(\frac{\mathbf{u}}{a} \right) = g_{r,a,\varphi}^\circ(\mathbf{u}) \end{array} \right. \quad (3.13)$$

It is interesting to notice how h is independent of the illumination function, while g is proportional to r , which is linked to the illumination function. **Thus, maximizing r results in maximizing the phase contrast** for all frequencies. The aperture of the diaphragm a induces a spatial rescaling on both h° and g° , however, a is also a linear modulation for g° (i.e. the maximum of g° becomes smaller for smaller values of a).

Here it is convenient also to relate contrast to the two transfer functions. Details on the calculation are provided in appendix A. To simplify the notation, I analyze the case of one-dimensional functions, however, the two-dimensional analysis shows the same results. I now suppose μ and ϕ as sinusoids of frequency u_0 , i.e. $\sin(u_0 x)$. Then, I find that the inverse Fourier transform of $\tilde{\mu}(u)h^\circ(u)$ and $\tilde{\phi}(u)g^\circ(u)$ are respectively $h^\circ(u_0)\sin(u_0 x)$ and $\frac{g^\circ(f)}{j} \cos(fx)$. Since $g^\circ(f)$ is a complex function, both quantities are real. Furthermore, besides a phase shift, both terms are still sinusoid whose amplitude are rescaled by the two terms $h^\circ(u_0)$ and $|g^\circ(u_0)|$. Thus, absorption and phase contrast are proportional to the two transfer functions.

3.2 Simulations

3.2.1 Monte Carlo Simulations of backscattering

In order to estimate the illumination function caused by backscattered light in the eye, I simulated the light scattering process in the retina. I used Monte Carlo simulations to trace photons in and out of the retina and to obtain the emission direction of the backscattered photons. For each simulation, all photons are delivered with the same angle on the same spot on the substrate, as if the light was composed of a single beam of zero diameter. Figure 3.2 shows the simulations for a 70° incoming beam on a substrate of Retina Pigmented Epithelium (RPE) laying on top of the choroidal layer. The distribution of the backscattered light can be considered as the spatial intensity measured at a plane in the far field of the scattering media. The key parameters for the simulation (the scattering coefficient, the absorption coefficient and the anisotropy parameter) have been obtained from literature in the case of 633 nm illumination for bovine RPE and choroid [143-146].

	Anisotropy	Scattering coefficient [mm ⁻¹]	Absorption coefficient [mm ⁻¹]
RPE	0.84	114	102
Choroid	0.979	87	0.287

Table 3.1

The intensity spectrum obtained from the simulations is shown in Figure 3.2a and its central cross section is shown in Figure 3.2b, together with an illustration of the illumination and backscattering. The profile becomes approximately linear for a small numerical aperture (reduced values of k_x and k_y), which is close to the linear illumination approximation discussed in the previous section. Simulations for different incoming beams showed similar behavior for angles greater than 40°.

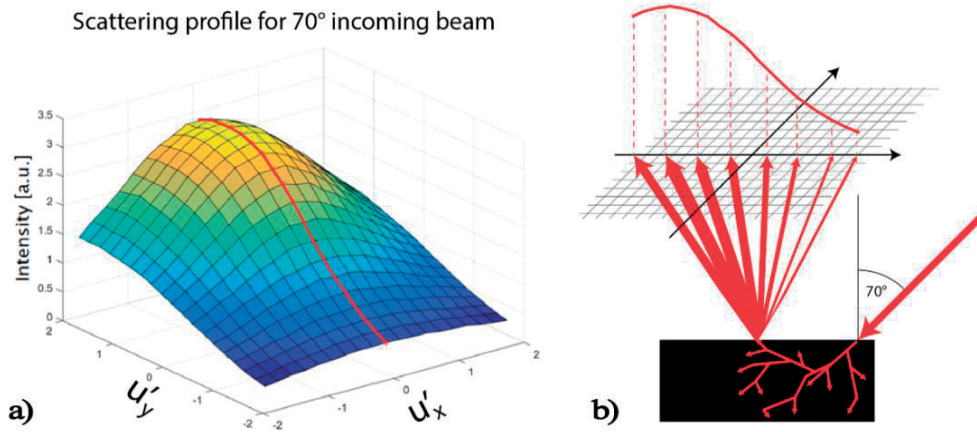


Figure 3.2

Simulations for a 70° illumination of a RPE sample on choroid. a) Profile of the backscattered light in the Fourier plane and b) illustration of the illumination and backscattered light. The profile is approximately linear close to the center.

3.2.2 Shape of the transfer function

In this section, I analyze the shape of the two normalized transfer functions g and h . This will help us analyze the contrast for different spatial frequencies and how different parameters can affect such a contrast. Transfer functions h and g have been calculated in MATLAB using (3.4), obtained from Tian's work. The illumination function is chosen linear (S°) and the pupil function P is chosen as a circular, aberrations-free, fully transmitting aperture. Since in the integrals, S° appears always

multiplied by P , in the following, I show the product of the two as in Figure 3.3. Because of that, negative values of the illumination function S° are not a problem as long as they do not appear in the SP product.

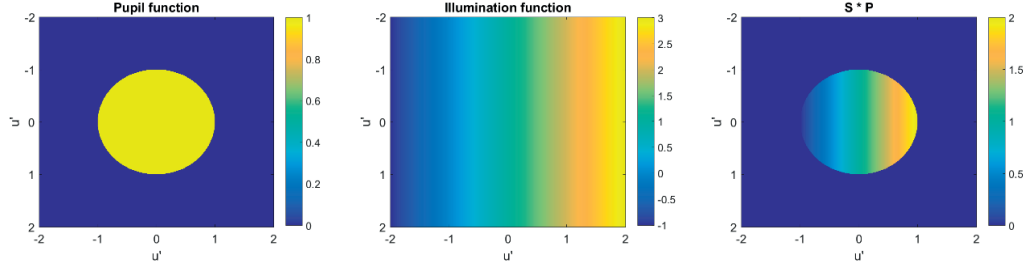


Figure 3.3

Left) circular, fully transmissive, aberration free pupil function. Center) Linear illumination function with $r = 1$. The function presents also negative values. Right) product PS° , representing the only relevant part of S° . Here only non-negative values can be present.

The normalized absorption transfer function h° has the same shape as the modulation transfer function for the case of an incoherent illumination (Figure 3.4). Indeed, from (3.6), h° is obtained as the convolution of two pupil functions. It is circularly symmetric (and so independent on the illumination angle φ) and has a maximum at the origin and an almost linear decrease towards the periphery. Also, the radius of its base is twice the radius of the pupil. Meaning that the frequencies that can be recorded are doubled that of the coherent illumination case. This is common for the case of incoherent illumination. Also, the point spread function derived from h° resembles the standard shape in the case of incoherent illumination.

The normalized transfer function for phase is rather different. Its maximum is not 2, as it was for h° , but ~ 0.4 in the case of $a = r = 1$. Its value is zero for all frequencies perpendicular to the gradient of S° . Also, while h° is all positive, the imaginary part of g shows two lobes with opposite sign. This can be compared with the transfer function of a partial derivative $\frac{\partial}{\partial x}$ that, thanks to the properties of the Fourier transfer function, is equal to ju_x [147]. So, we see that for low frequencies the transfer function is similar to a partial derivative, however, instead of keeping increasing for higher frequencies, g° reaches a maximum and then starts decreasing almost linearly. The differential behavior discussed for low frequencies (and further discussed in section 3.2.5) can

also be seen in the shape of the point spread function that is almost equivalent to the partial derivative of the PSF of h° .

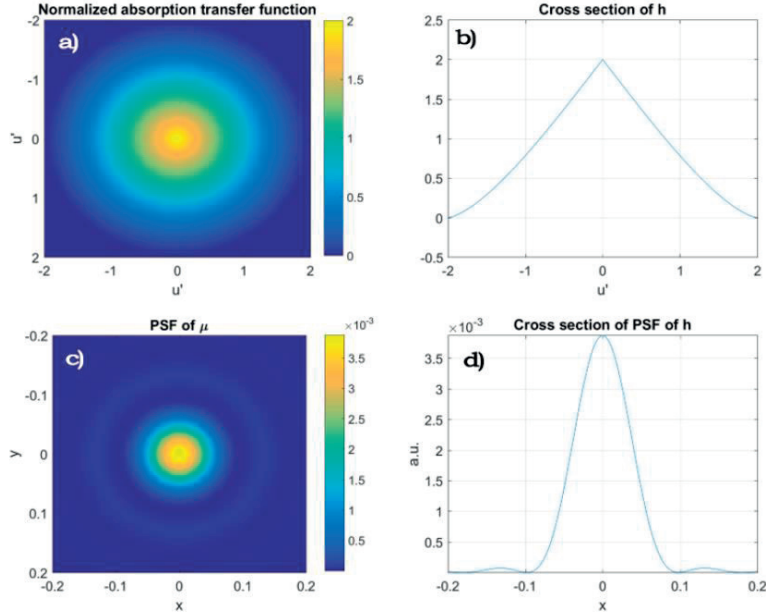


Figure 3.4

a) absorption transfer function and b) its cross section passing through the center. c) PSF derived from h and d) its cross section passing through the center.

We can now observe the effect of the different parameters on the two transfer functions. As expected from 3.1.2, h° is dependent only by the radius of the pupil function a , which only induces a shrinkage or expansion in the function. Indeed, the larger the pupil, the more spatial frequencies are collected. A similar effect is present also for g , even if a does not only introduce a shrinkage, but also multiply the function. In this way, moving from $a = 1$ to $a = 0.5$ decreases the maximum of g by a factor 2. As previously discussed, φ introduces only a rotation in g . While the effect of r is a modulation of g .

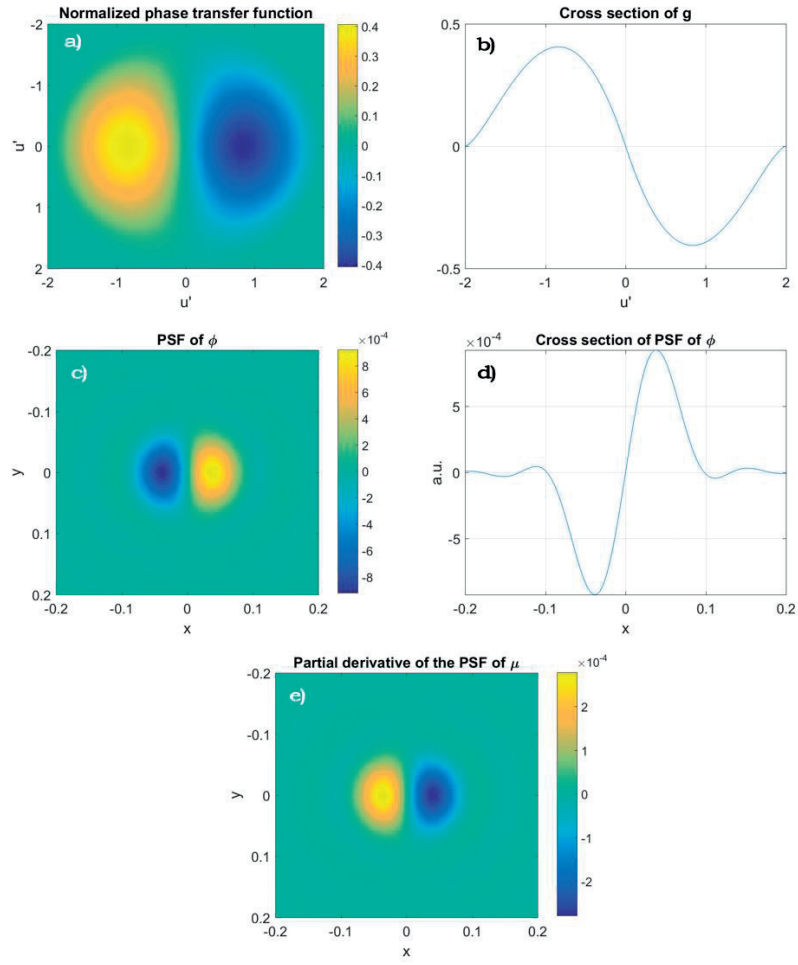


Figure 3.5

a) phase transfer function and b) its horizontal cross section passing through the center. c) PSF derived from g° and d) its horizontal cross section passing through the center. e) partial derivative of the PSF of h° .

This means that, if the phase contrast needs to be maximized for a specific frequency \mathbf{u}' , it is convenient to orient the illumination in such a way that \mathbf{v}_ϕ is parallel to \mathbf{u}' . Also, the higher r the larger the contrast. Regarding a , we notice that reducing the pupil aperture without changing the illumination function (and so same r) results in an illumination of reduced amplitude (whose intensity is between 0.5 and 1.5 instead of between 0 and 2).

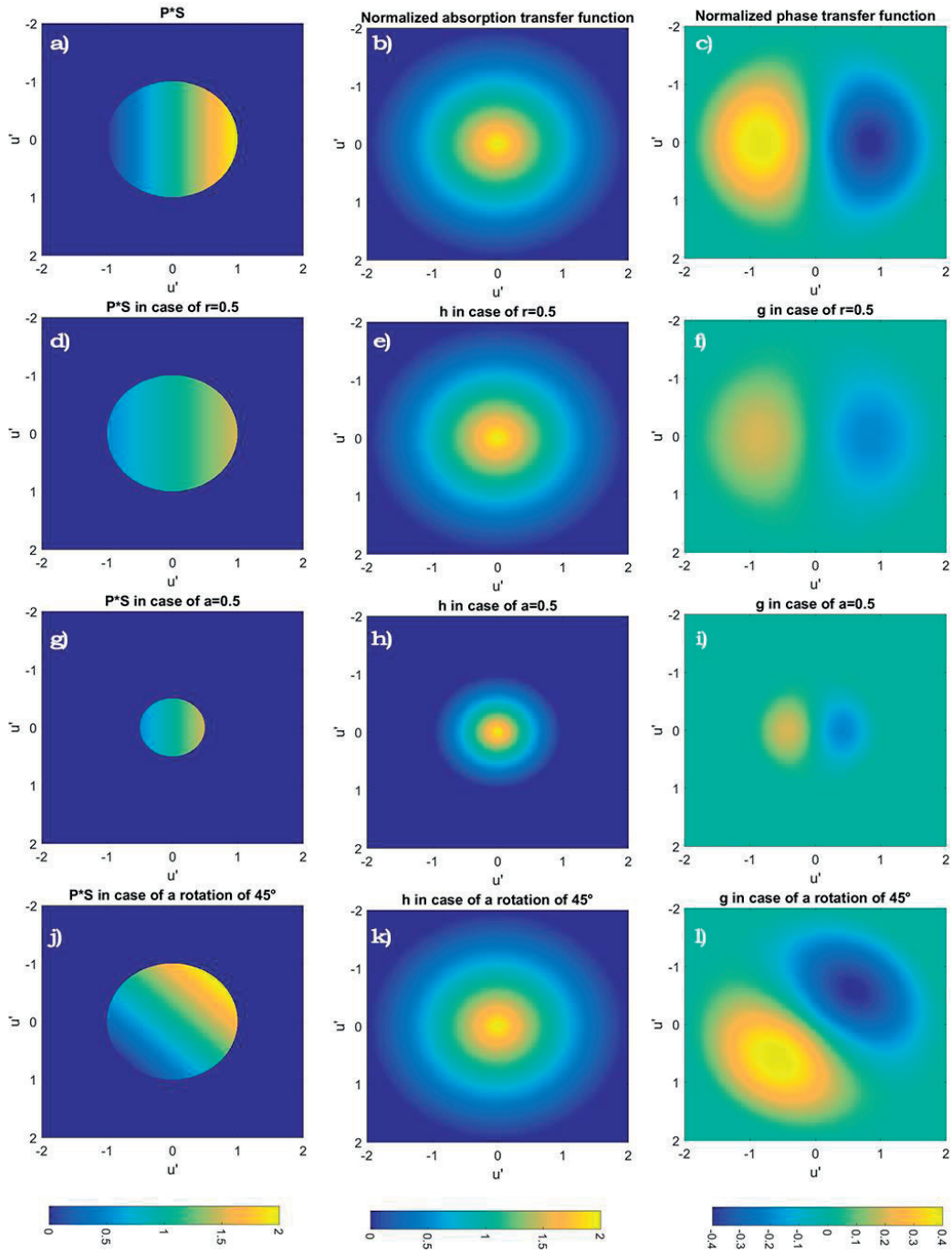


Figure 3.6

a) Product SP and the resulting b) h° transfer function and c) g° transfer function. d-f) same set of images in the case $r = 0.5$. g-i) same set of images in the case $a = 0.5$. j-l) same set of images in the case of a change in φ of 45° .

In Figure 3.7, several cross sections of g° are analyzed. Specifically, by renormalizing each cross section it is possible to observe always the same curve as illustrated in (Figure 3.7c).

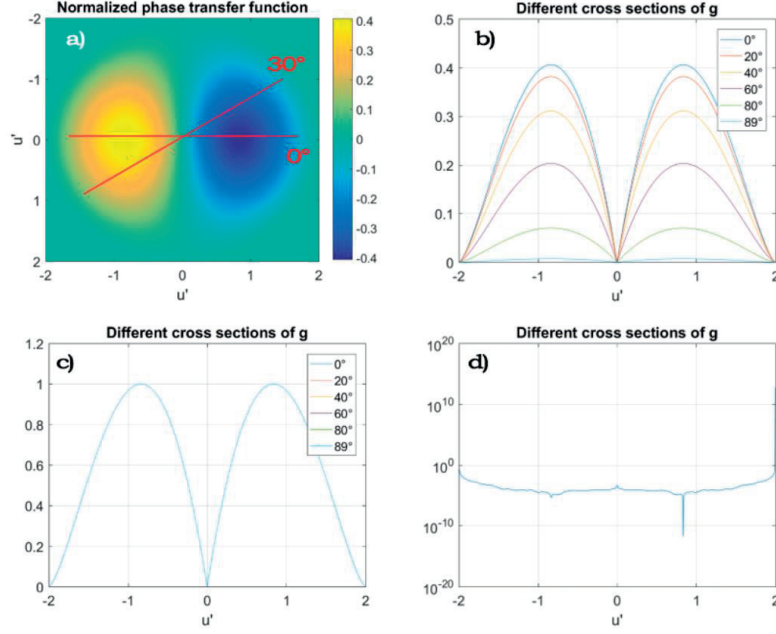


Figure 3.7

a) g° function on which two lines are drawn representing the different cross sections. b) cross section obtained for different angles. c) renormalized cross section curves. d) normalized standard deviation for the curves showed in c).

This means that g° can be approximated as a product between a radial and an angular function. Thus writing:

$$g_{a,r,\varphi}(u', \theta) = a r \gamma_a(u') l_\varphi(\theta) \quad (3.14)$$

Where $u' = |\mathbf{u}'|$, θ is the angular coordinate, $\gamma_a(u')$ is a radial function and $l_\varphi(\theta)$ an angular one. Furthermore, by plotting the maximum for different cross sections (Figure 3.8) it is possible to observe a cosine-like behavior. Thus, it is possible to write:

$$l_\varphi(\theta) \sim 0.4 \cos(\theta - \varphi) \quad (3.15)$$

Thus, $l_\varphi(\theta)$ shows the relatively small sensitivity of the phase contrast with respect to the angle φ . Indeed, $\theta - \varphi$ need to exceed 25° to have a drop of 10% and 60° to have a drop of 50%. This means that the **contrast is not affected by a small misalignment** in the illumination function.

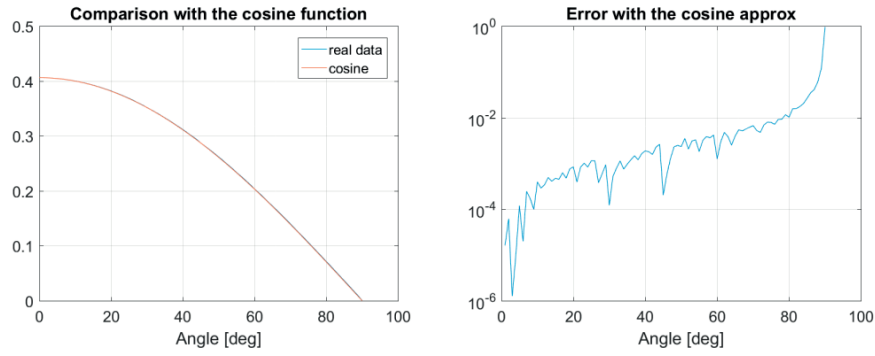


Figure 3.8

Left) Maximum of the cross section for different angles and cosine approximation. The cosine function has been multiplied by the maximum of the real data curve. The two curves are almost perfectly overlapped. Right) Difference between the two curves divided by their mean value.

Another interesting property of h° and g° that can be analyzed is that g° can be obtained from h° as:

$$\text{Imag}\{g_{a,r,\varphi}^\circ(\mathbf{u}')\} \sim -0.5 S^\circ(\mathbf{u}') h^\circ(\mathbf{u}') \quad (3.16)$$

Meaning that g° can be obtained by h° just by multiplying it by a ramp. This can be seen in Figure 3.9 where g° and the $S^\circ h^\circ$ product are plotted. Also, the pixelwise difference between the two gives a flat image.

Such a result correlates with what I showed before for the PSF. Furthermore, it is interesting for the deconvolution. Indeed, we know that deconvolving the resulting image with the transfer function h° , will produce a transfer function for the phase that is equivalent to a partial derivative.

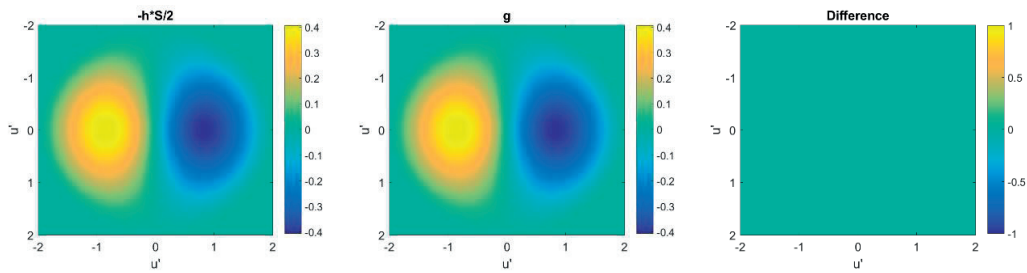


Figure 3.9

Left) the $S^\circ h^\circ$ product multiplied by -0.5. Center) Imaginary part of g° . Right) difference between the two functions

3.2.3 Alternative pupil functions

In the previous section, I analyzed the shape of the transfer functions in the case of the ramp approximation, showing how the three main parameters (a , φ and r) affect g° and h° . For doing that, I assumed a circular pupil even if, as discussed in chapter 1, some phase contrast techniques use different pupil shape. Because of that, in this section I will analyze the effect of different pupil functions on g and h within Tian's model, showing how some pupil shapes maximize contrast for specific frequencies.

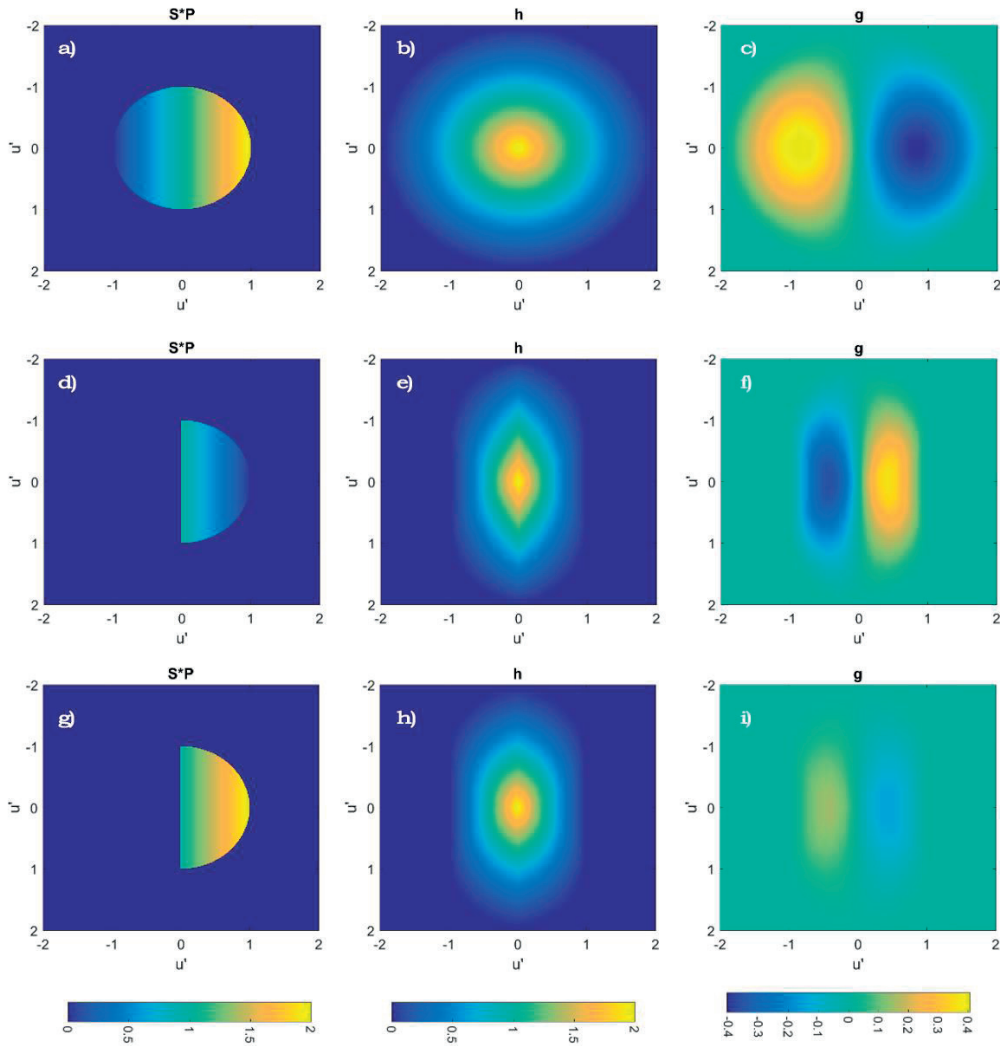


Figure 3.10

a) Product SP. b) Resulting g transfer function. c) Resulting h transfer function. d-f) same set of images in the case of half disc pupil function and an illumination function with the maximum on the right. g-i) same set of images in the case of half disc pupil function and an illumination function with the maximum on the left.

The first type of pupil that I investigate is the half-disc pupil, as showed in Figure 3.10. From Figure 3.10 it is possible to observe how such a shape produces transfer functions elongated along the vertical axis. Indeed, the vertical axis of the pupil presents a numerical aperture that is twice that of the horizontal axis. This means that, compared to a full pupil, such a technique reduces the range of recorded frequencies.

It is also relevant to notice that, by flipping S , two illumination conditions are possible: with the maximum on the right or on the left. Such a condition is non-symmetrical, producing higher contrast in the second case.

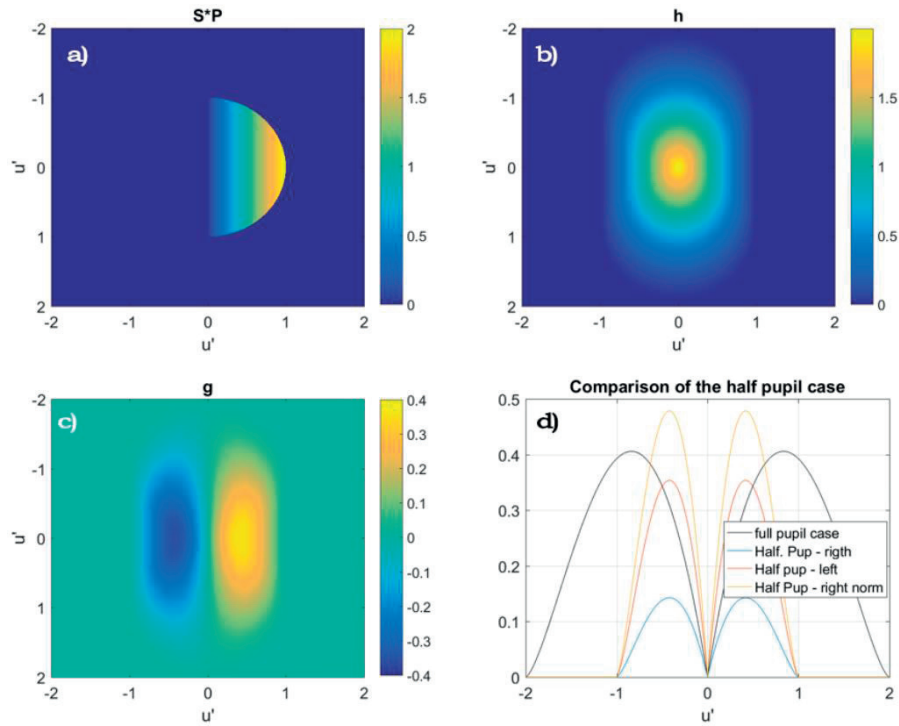


Figure 3.11

a) SP product in the case of optimized contrast and the consequent b) absorption transfer function and c) phase transfer function. d) Horizontal cross section of the different half-disc transfer functions. It is possible to see how they can be used for improving lower frequencies despite losing half of the frequency range.

It is interesting to notice that, in one case, the contrast of the illumination function within the pupil aperture $(max - min)/(max + min)$ is equal to 1, while in the flipped case, it is smaller. Then, by maximizing the contrast of the illumination function it is found a more intense transfer function (as shown in Figure 3.11). However, such a configuration would require the ability to reshape the illumination function having 0 intensity for $u'_x = 0$.

Figure 3.11 d shows a comparison of the horizontal cross section between the different cases and the case of a circular pupil. Despite the fact that half disc configuration diminishes the range of achievable frequencies we can notice how such a configuration improves the contrast at small frequencies.

The other case I analyze is the quarter circular pupil. Two illumination conditions are possible, and improving the contrast of the illumination increases the intensity of the transfer function. Figure 3.12 shows a comparison between the different cases. The range of collected frequencies is smaller, however and the achievable gain for small frequencies is less than the case of half disc pupil.

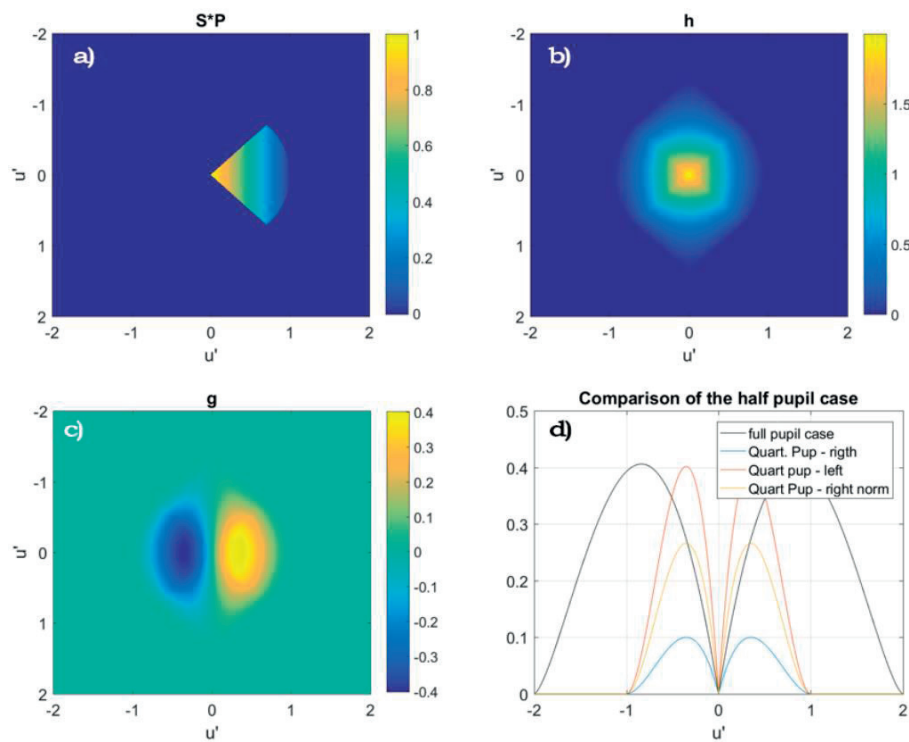


Figure 3.12

a) SP product in the case of quarter of disc pupil and the consequent b) absorption transfer function and c) phase transfer function. d) Horizontal cross section of the different quarter-disc transfer functions. Also in this case there is a decrease in the base of the function respect to the full pupil case and also in this case the transfer function improves lower frequencies. However, the increase is smaller than the one achieved in the half disc case.

If a specific spatial frequency needs to be collected, it is possible to filter out all the other frequencies by using a ring aperture. However, for partially coherent illumination the resulting effect is more complex. From Figure 3.13, it is possible to see that a ring in the pupil plane produces

also a ring in the transfer functions, but with double frequency. Specifically, by calling a_i the inner radius of the ring, we can see that for increasing a_i the resulting ring in g becomes thinner and more squeezed to higher frequencies.

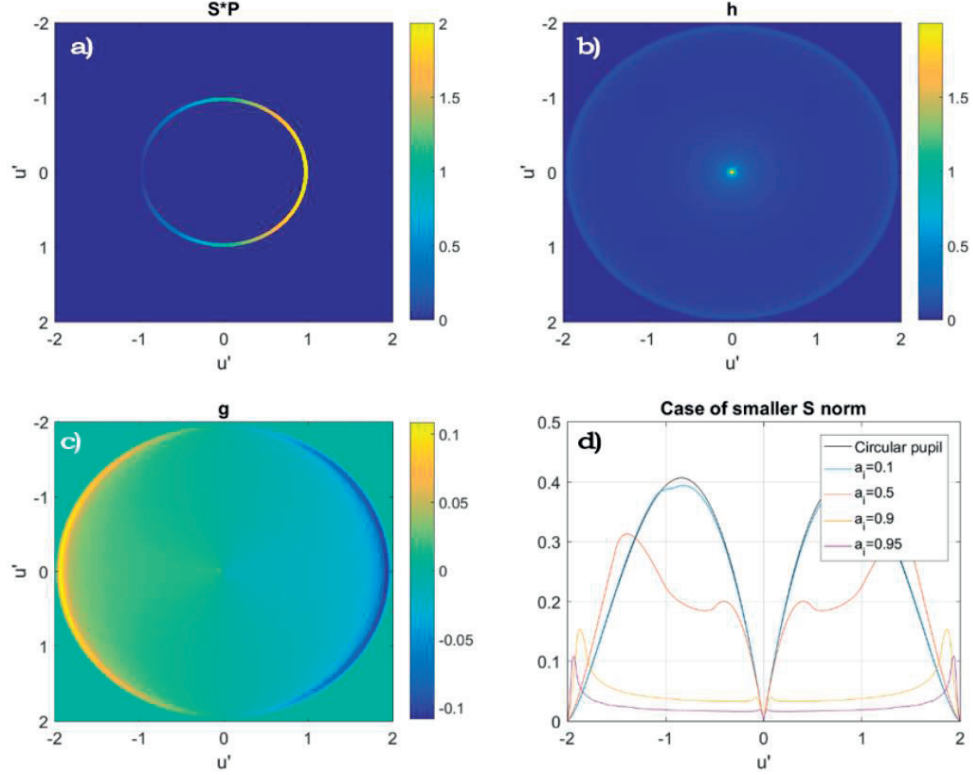


Figure 3.13

a) SP product in the case of a ring pupil and the consequent b) absorption transfer function and c) phase transfer function. d) Horizontal cross section of the different ring transfer functions. As the internal radius tends to the external one, the peak of the transfer function moves to higher frequencies.

It is possible to further improve the selectivity of the spatial frequency by blocking part of the ring. Mathematically this is equivalent of multiplying the ring aperture with a slit aperture P' of the type:

$$P'_{a_v}(\mathbf{u}') = \begin{cases} 1 & \text{for } |u'_y| < a_v \\ 0 & \text{elsewhere} \end{cases} \quad (3.17)$$

This is shown in Figure 3.14 where the parameter a_i has been chosen to be 0.95 and a_v , which represents the aperture of the slit, is varied. We can see how such a filtering improves dramatically the modulation of the high frequency components and thus producing an increase of more than an order of magnitude.

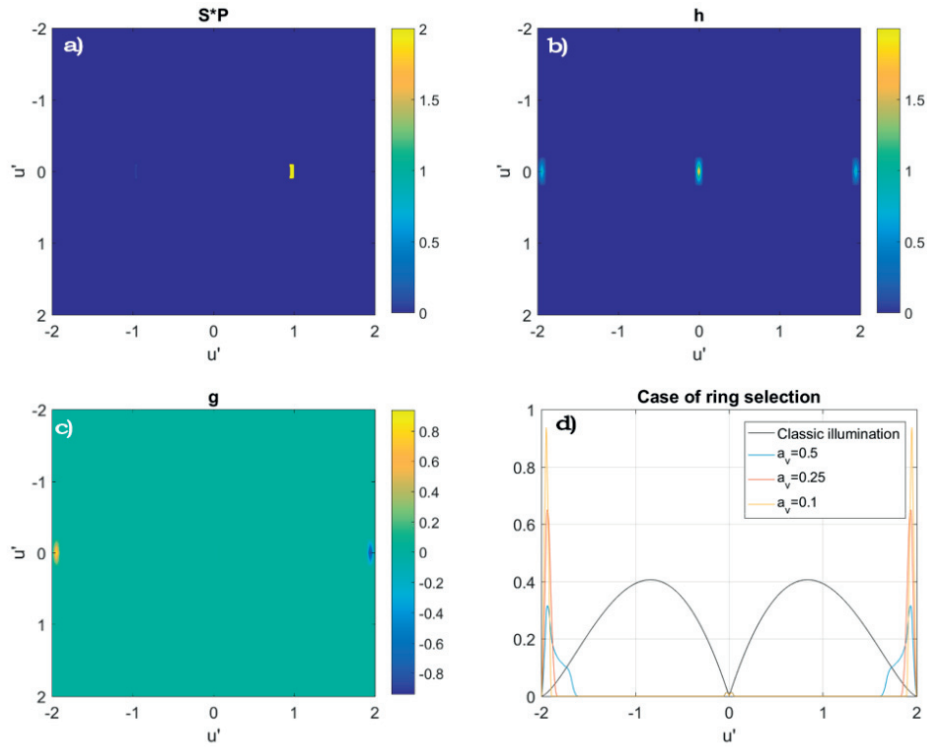


Figure 3.14

a) SP product in the case of a slit-ring pupil and the consequent b) absorption transfer function and c) phase transfer function. d) Horizontal cross section of the different slit-ring transfer functions. As the slit aperture a_v diminishes, the contrast of high frequencies increases.

Another technique that is worth analyzing (and that was already presented by Tian) regards the use of a smaller illumination, instead of a smaller pupil. Even if this still results in a smaller SP product, it is important to remark that this is not equivalent to having a smaller pupil. Indeed, the integrals used for calculating g contain both the product $S P$ and a shifted pupil function P .

From Figure 3.15, we can see how such a configuration produces a g that is zero almost everywhere, except for a ring close to the frequencies of $u' = 1$.

Figure 3.16 illustrates the effect of different radius for the illumination function (called a') showing that as a' tends to 0 the ring of g becomes thinner and thinner. Furthermore, just reducing the radius (without changing r) produces also a flatter illumination function and a less intense g (Left side of Figure 3.16). While, if the product $a'r$ is kept constant to 1 (this product is similar to the contrast), the maximum of the g function keeps increasing, even if such an increase is relatively small.

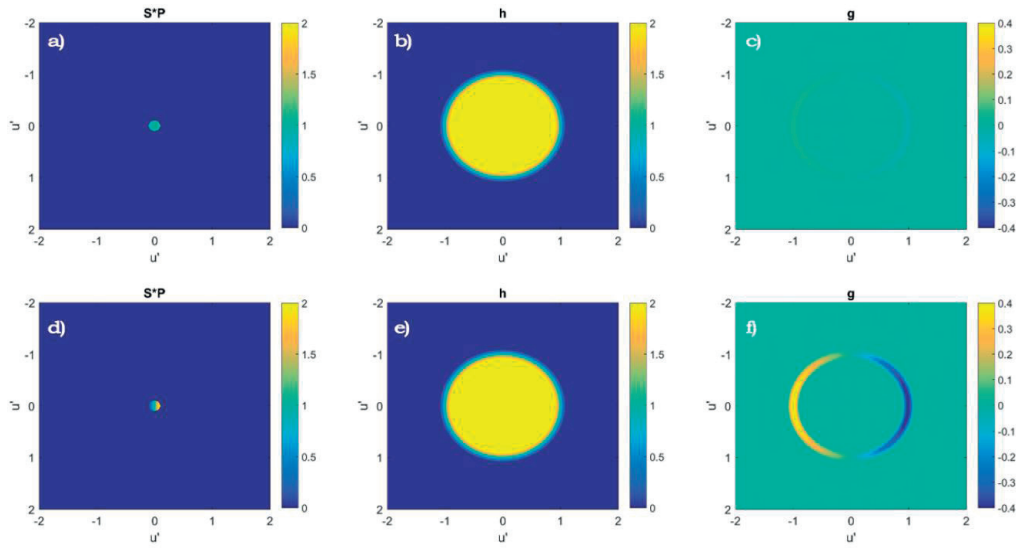


Figure 3.15

a) SP product in the case of a smaller illumination function (radius 1/10 of the pupil's one) and the consequent b) absorption transfer function and c) phase transfer function. e-g) the same set of figures in the case where the illumination's contrast has been reduced of a factor 10.

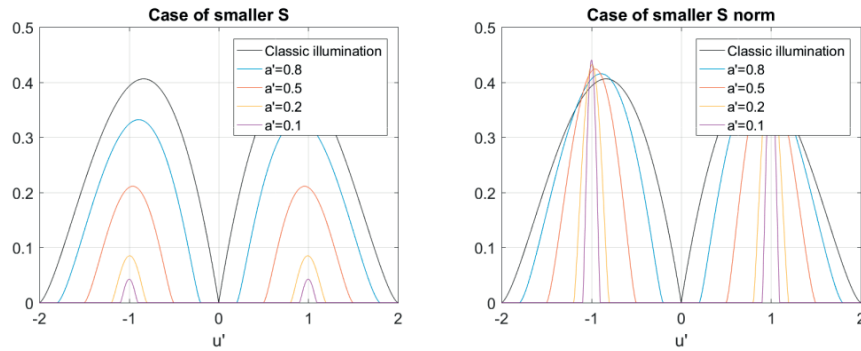


Figure 3.16

Left) Cross section of the phase transfer functions for different a' in the case of fixed r . Right) Cross section of the phase transfer functions for different a' in the case $a'r = 1$.

Figure 3.17 shows a comparison of the previous pupil functions. It is possible to observe that both the case of half and quarter of circle aperture improve low frequencies. Using a smaller base for illumination improves middle frequencies, but the gain is extremely small. Furthermore, all these solutions require also a change in the illumination to be able to provide an improvement in the transfer function. This is not the case of ring and slit-ring apertures which appear to improve the high frequencies. Furthermore, the ring-slit shows an increase of almost 2 orders of magnitude. The main drawback of such a technique is the small amount of transmitted power. Indeed,

an aperture as the one used for obtaining the curve in Figure 3.17 has a transmittance equal to 0.64 % of the transmittance of the full pupil.

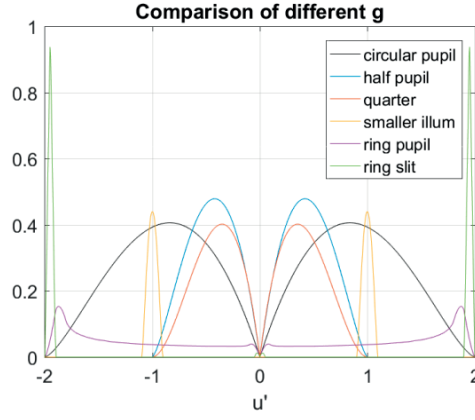


Figure 3.17

Comparison of the cross section of the previously shown pupil function.

3.2.4 Non-linear illumination function

Results up to now have been obtained under the assumption of a linear illumination function. In practice, the illumination caused by backscattering in a full retina sample (including sclera and RPE) will likely show some deviations from linearity. Thus, in this section, I investigate the effect of non-linear illumination functions. This will show how stable the ramp approximation is when the illumination function deviates from linearity.

Different g functions cannot be directly compared pixel by pixel, since their amplitude is modulated by r . Because of that, in this section, instead of g , I will compare a function called \bar{g} , obtained as g/r . However, up to now r has been defined only for linear function. Because of that, here I will define a more general definition of r as:

$$r = \frac{\text{Slope}[S_{odd}(\mathbf{u}')]]}{\text{Mean}[S_{ev}(\mathbf{u}')]]} \quad (3.18)$$

With $\text{Slope}[\]$ being the gradient of the linear interpolation, $\text{Mean}[\]$ being the average value and with S_{odd} and S_{ev} calculated as:

$$\begin{cases} S_{odd}(\mathbf{u}') = \frac{S(\mathbf{u}') - S(-\mathbf{u}')}{2} \\ S_{ev}(\mathbf{u}') = \frac{S(\mathbf{u}') + S(-\mathbf{u}')}{2} \end{cases} \quad (3.19)$$

In the following, I will use several different illumination functions, each one depending on different free parameters. Thus, for the sake of readability, I will neglect the parameters in the subscript and put just a number as a reference. i.e. instead of S_{a_1, φ_1, r_1} I will directly write S_1 . The same notation will be used for the \bar{g} functions. The function \bar{g}_0 will denote the transfer function obtained in the case of the linear illumination s ($a = r = 1$). I also define the pixelwise error $\varepsilon_p\{\sim\}$ between two functions $f_i(\mathbf{u}')$ and $f_j(\mathbf{u}')$ as:

$$\varepsilon_p\{f_i(\mathbf{u}'), f_j(\mathbf{u}')\} \triangleq \frac{\sum_{\mathbf{u}'} \text{abs}(f_i(\mathbf{u}') - f_j(\mathbf{u}'))}{\sum_{\mathbf{u}'} \text{abs}(f_i(\mathbf{u}')) + \text{abs}(f_j(\mathbf{u}'))} \quad (3.20)$$

With $\sum_{\mathbf{u}'}(\sim)$ being the sum on all the pixels \mathbf{u}' .

In Figure 3.18, I compared the transfer functions \bar{g}_i obtained for different illumination functions S_i . The tested illumination functions are: linear functions (Figure 3.18a), linear function with added random noise (Figure 3.18b), piecewise linear (PL) functions (Figure 3.18c) and sinusoidal functions (Figure 3.18d). From Figure 3.18e-h, we notice that all illumination functions S resulted in similar \bar{g}_i functions. The difference of the phase transfer functions $\text{abs}\{\bar{g}_i(\mathbf{u}) - \bar{g}_0(\mathbf{u})\}$ is illustrated in Figure 3.18i-n.

As expected, the difference between \bar{g}_0 and the \bar{g} obtained with linear illumination is zero for all tested linear illuminated functions. However, the difference starts to increase when the illumination function deviates from the linear case. Figures o and p, show plots of the deviation from linearity of the illumination function and the error on the transfer function \bar{g}_0 . The illumination functions used for this analysis are:

$$\begin{cases} S_2(\mathbf{u}') = s(\mathbf{u}') + \alpha N(\mathbf{u}') \\ S_4(\mathbf{u}') = 1 + \text{Sin}(\alpha \pi u'_x) \end{cases} \quad (3.21)$$

Where α is a free parameter between 0 and 1 and $N(\mathbf{u}')$ being the two-dimensional white noise, whose values are distributed between 0 and 1.

Even when the deviation from linearity in the illumination function is large (e.g. 35%), the error in the phase transfer function is still relatively small (6% in the same condition).

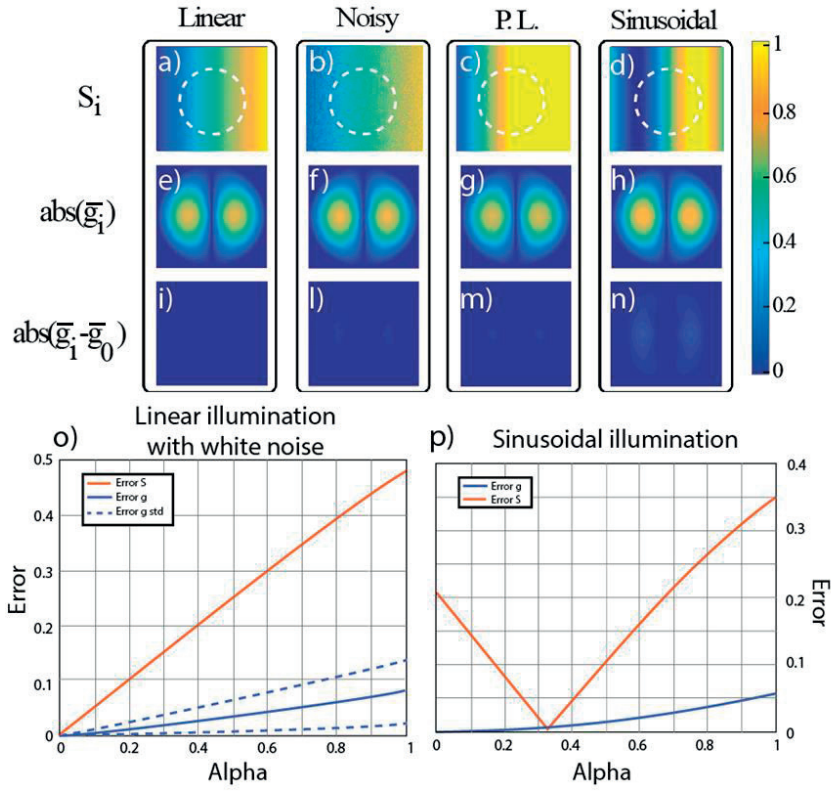


Figure 3.18

a-d) illumination function in the case of linear, linear plus white noise, piecewise linear and sinusoidal profiles. b) and d) have been obtained for $\alpha = 1$. The dashed circle represents the size of the pupil function. e-h) respective transfer functions. i-n) subtractions of the obtained transfer function and the transfer function obtained for S_0 (perfectly linear case). o-p) error between S_i and S_0 and between g_i and g_0 in case of sinusoidal and noisy illumination function. In o), the blue curve has been averaged and the dashed curves represent the mean value plus or minus the standard deviation.

For this section, I conclude that the transfer function corresponding to a linear ramp illumination can be considered approximately valid also for illumination functions that differ from the ideal linear illumination function which we will find in practice. Hence, maximizing r for increasing phase contrast also holds for non-linear illumination functions.

3.2.5 Phase contrast images

In this section, I analyze how the previously discussed transfer functions affect the resulting image. Since h° is the transfer function of an unaberrated optical system with incoherent illumination, the expected result is just a blurring of the image. The results of g° , instead, is more complex and it needs a more detailed analysis.

Figure 3.19 show the Siemens star, used as target, after its convolution with \tilde{h}° and \tilde{g}° . As expected, the convolution with \tilde{h}° generates a blurred version of the image (in which the central region is not visible anymore). The convolution with \tilde{g}° also shows blurring the central part of the image. However, it is possible to see how the edges have been enhanced depending on their orientation. Indeed, the contrast is maximal for vertical edges and zero for horizontal ones (since illumination is along the x axis).

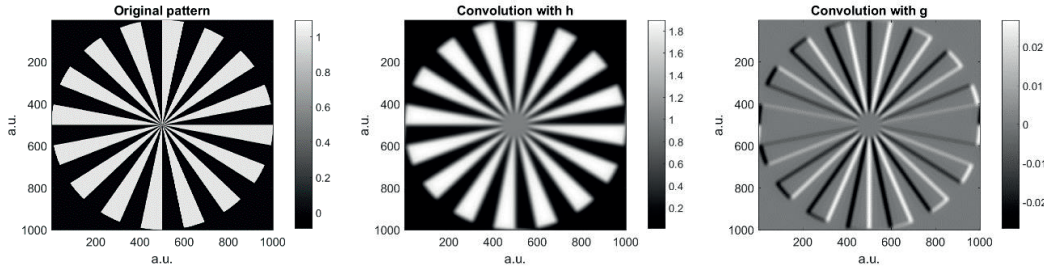


Figure 3.19

Left) Siemens star used as target and the corresponding Center) convolution with \tilde{h}° and Righ) convolution with \tilde{g}° .

To provide a better insight, I analyze here the effect of such a transfer function on a pattern composed of bars. Figure 3.20 shows the result for three different spatial frequencies. For comparison purposes, g° has been rescaled between the three cases. We can observe that, for low frequencies, g° acts as a partial derivative, enhancing the edges. For higher frequencies, the pattern is turned into sinusoids. Finally, for high frequencies the sinusoid is strongly distorted. This is comparable with what we saw in 3.2.2, where it was shown that convolution with \tilde{g}° is equivalent to the partial derivative of the convolution with \tilde{h}° .

It is also interesting to notice that for h° , the contrast of the resulting image is a measurement of the intensity of the transfer function. However, this is not the case for g° since, as shown in Figure 3.20, the contrast is the same for the different frequencies. This is due to the derivative-like behavior of g° which, for low frequencies bars, enhances more the edges than the carrier frequency.

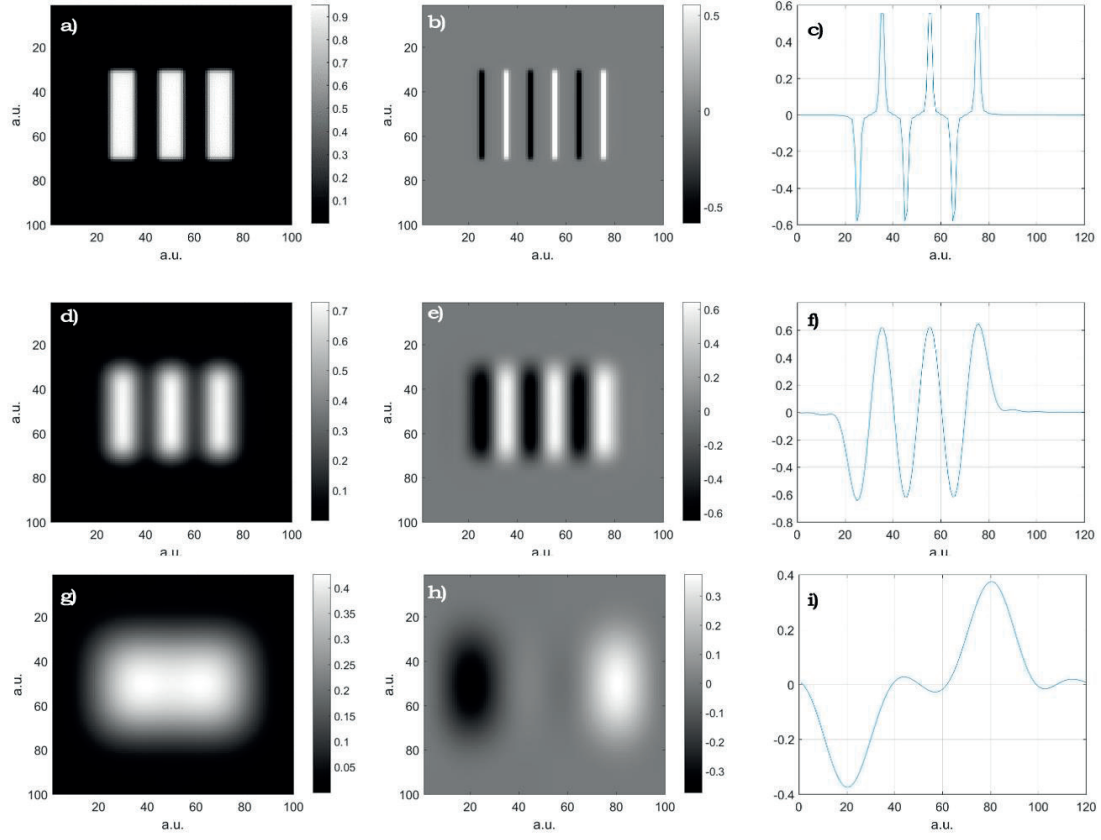


Figure 3.20

a) Bar plot with carrier frequency $u' = 0.1$ convolved with \tilde{h}^0 , b) with \tilde{g}^0 and c) its cross section. d-f) same plots for a carrier frequency $u' = 1$ and g-i) in the case $u' = 2.5$.

3.3 Experimental validation

In this section, I use ex-vivo experimental samples of human eye to test the effect of the slope on the contrast. This will be conducted both by using the backscattering properties of the retina and by using specific illumination pattern.

The most straightforward solution consists in illuminating the RPE with a non-uniform pattern (as shown in Figure 3.21). In this way the RPE acts as the display plane discussed in 3.1.1 and so S coincides with the intensity at the RPE plane. The main drawback of such a method is that different retinal points are illuminated with a different intensity. This means that the product SP is not shift invariant.

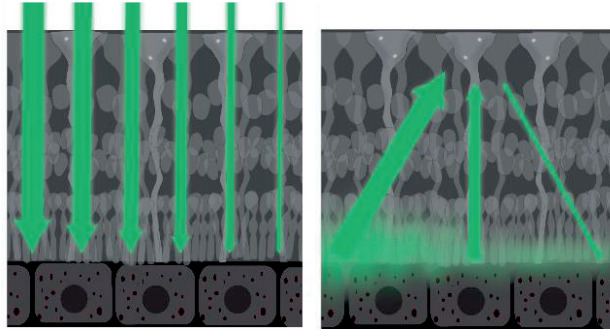


Figure 3.21

Left) Non-uniform illumination of the RPE and Right) the resulting backscattered illumination.

An alternative way consists in using uniform oblique illumination. In this case the light backscattered from the RPE is not symmetric, thus, providing phase contrast. Furthermore, if all the RPE points are illuminated with the same angle also the backscattered light maintains the same profile for different retinal points. It is however important to notice how, in this case, S is not the intensity at a physical plane, but rather the angular spectrum of the backscattered light.

3.3.1 Experimental setup

In order to experimentally validate the proposed model, I built the optical setup shown in Figure 3.22a. It consists in two main imaging arms: one in which the camera plane is conjugated with the object plane (sample camera) and the second one in which the camera plane is conjugated with the Fourier plane (pupil camera), which is directly the illumination profile in spatial frequency coordinates. The cameras used as sample camera and pupil camera are respectively DCC3240M from Thorlabs and camera C9100-23B from Hamamatsu.

Illumination is provided with either the back-reflection illumination (S1) or with the transmission illumination (S2). Back-reflection illumination is obtained by using commercial LEDs. Transmission illumination is obtained by displaying pattern on an active matrix organic light emitting diode (AMOLED) display, Samsung Galaxy J5. To provide non-uniform illumination of the sample a lens has been placed between the LED and the sample.

The biological samples used in the following experiment are samples of human eye. The human eye has been given by the Fondation Asile des aveugles, Lausanne, Switzerland. Samples have been fixed with 4% paraformaldehyde (PFA) for 24 hours.

A calibrated United State Air Force (USAF) phase target positioned on top of a scattering layer (white paper) is used to quantify the quality of the obtained phase image. The USAF target is etched in glass with a groove depth of 200 nm.

Furthermore, all the images coming from the sample camera have been normalized according to the formula:

$$J_s(\mathbf{x}) \triangleq \frac{I_s(\mathbf{x})}{\text{Low}\{I_s(\mathbf{x})\}} \quad (3.22)$$

Where $\text{Low}\{\sim\}$ is a two-dimensional lowpass filter. Such a normalization method will be discussed in detail in chapter 4.

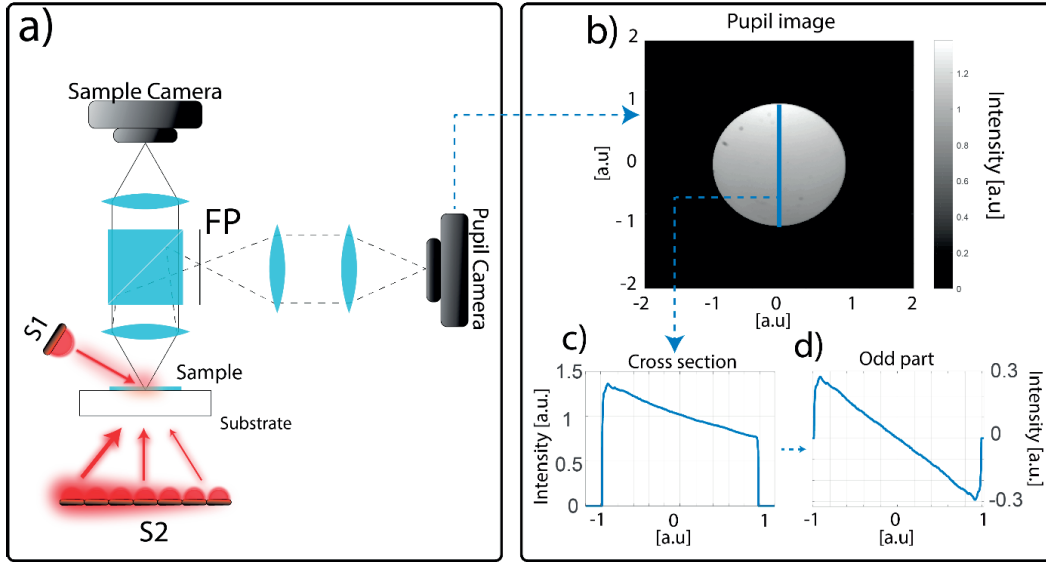


Figure 3.22

a) Imaging system used for system validation. Illumination can be provided in reflection, using illumination S1, or in transmission, using illumination S2. The sensor of the Sample Camera is conjugated with the object plane, while the pupil camera is conjugated with its Fourier plane (FP). b) pupil image in case of choroid human sample illuminated in backreflection (S1), c) its cross section and d) its odd part. The odd part appears to be more linear than its original profile.

The objective used for collection is a 10x, 0.25 NA from Olympus (RMS10X). A choroidal human sample illuminated in backreflection, provides an image on the pupil camera (figure 2b) which corresponds to the illumination function. Figure 2c and 2d show the cross section of the illumination function obtained from a choroidal sample. We notice that the odd part is approximately linear and thus a good approximation to the linear model developed in section 3.1.2.

3.3.2 Relationship between slope and contrast

In the previous sections, the ramp approximation showed a proportionality between illumination's r parameter and the phase contrast. Such a model, obtained for a transmission configuration, is here tested using the source S2 of the previously shown setup. The illumination functions are programmed as linear for which q is kept constant and only the slope m is changed (and so also r).

Figure 3.23 shows the results for a calibrated USAF phase target. The oblique linear illumination function of the phase target transforms phase contrast into intensity contrast. The intensity contrast (modulation depth) in the image increases, in accordance with the model, linearly with the parameter r . Here, the parameter r is normalized in such a way that the maximum value is equal to 1.

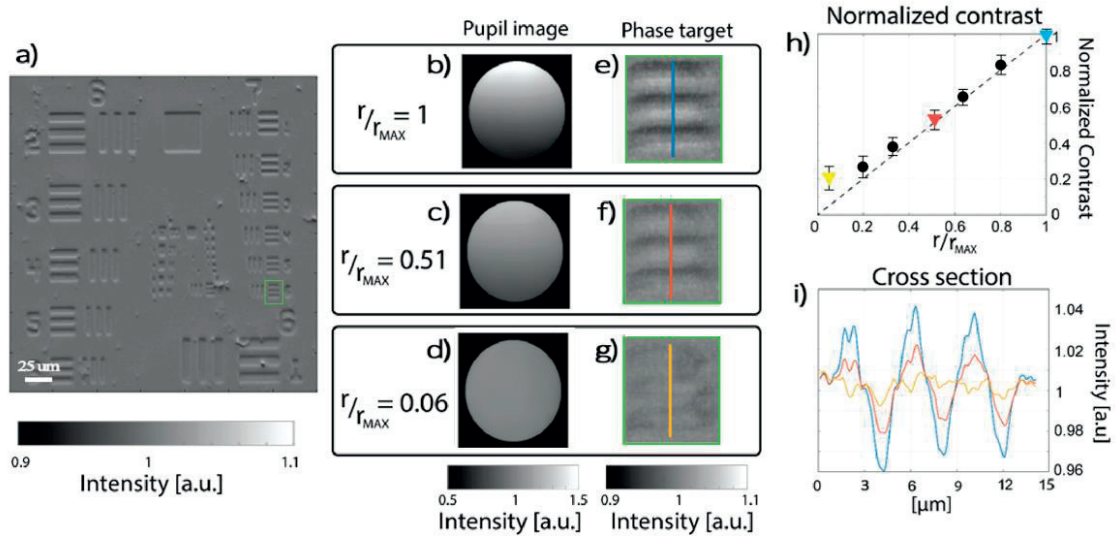


Figure 3.23

Experimental validation of the model. a) Phase image of the USAF target used for the measurement. b-d) pupil function for 3 different illumination cases obtained with a 0.25 NA objective. e-g) bars of a USAF target for the same illumination condition. It is possible to observe that as the illumination function becomes steeper (and so r larger), the contrast increases. The imaged area is a square of $110 \times 110 \mu m^2$. h) normalized contrast versus normalized r value. The colored triangles represent the values from the corresponding images. It is possible to observe that the experimental data follow the theoretical curve except for small values of r . i) cross section of the target images.

3.3.3 Backscattering of choroid

When oblique illumination is used as source of backscattered light, the illumination angle is the only free parameter. Thus, it is interesting to see how different angles of illumination affect r .

Experiments have been conducted on samples of fixed human on which the retinal layer was removed. The analyzed range of illumination angles is between 40 and 85°.

For each measurement, the position of the illumination source S2 was changed. For each sample, the curve r versus illumination angle was reproducible (error < 10%), but from sample to sample the resulting curve was strongly different (standard variation larger than 50% for some angles). Even if the ramp approximation holds for the experimental samples, the results differ from the Monte Carlo simulations. This can be explained from the fact that the used scattering parameters are the one coming from bovine eyes. This choice has been made since a complete set of data is not available for human tissues.

Figure 3.24 shows an average of 10 sample curves. Since the standard deviation is relatively large, it is not possible to know a priori what is the best illumination angle for a specific sample. However, the curve shows a decrease in r as the illumination angle increases. This means that, without extra sample knowledge, **the best illumination condition is obtained for small angles**.

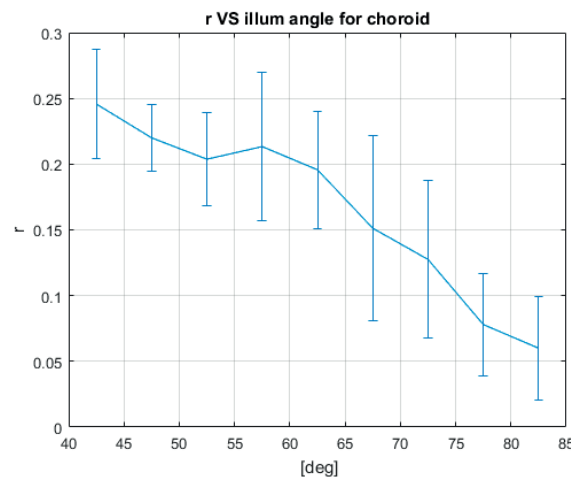


Figure 3.24

Dependence of the r parameter on the illumination angle for 10 different choroidal samples. The size of the error bars shows a big difference in the profile depending on the analyzed sample. However, the curve appears to provide the maximum r in the interval 40-60°.

3.3.4 Phase contrast of retina sample

In previous sections, I have shown that oblique illumination of RPE and choroid provides linear backscattered light, and that under this illumination condition, the intensity image shows a contrast proportional to r . From these observations, it would be reasonable to expect the same

results in a thick eye sample (i.e. retina on a choroidal layer). However, it is important to notice that, by using an illumination configuration as shown in Figure 3.22, light passes twice through the retina. In this way, we can expect that a certain amount of light will be scattered by the retina features. Such a signal is expected to introduce some disturbance in the linearity of the backscattered illumination spectrum.

I performed the experiment by shining light on the eye sample and measuring both r (in the pupil camera image) and the contrast in the intensity image (in the sample camera image). Contrast has been estimated for the same cross section as $(Max - min)/(Max + min)$. Where Max and min are respectively the maximum and minimum values of the analyzed cross section. The slope of the illumination function is changed by modifying the incoming illumination angle.

The measurement has been repeated for 10 sample areas for different illumination angles (i.e. different parameter r). For representation purposes, data have been normalized with respect to the maximum value of contrast and of r . Results are shown in Figure 3.25. The overall trend is higher contrast for higher r . However, the variability in contrast in different areas (error bars) is probably due to the contribution of direct scattered light from the retinal structures.

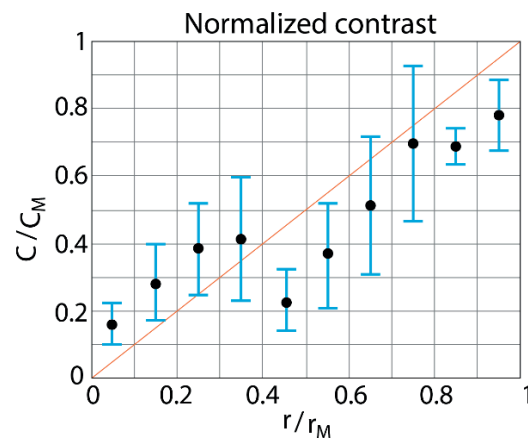


Figure 3.25

Normalized contrast versus normalized r . The size of the error bar shows a poor reproducibility between different analyzed areas of the same sample. This is expected to come from the contribution of backdiffracted light. The curve also shows that maximization of r brings, in general, a better contrast.

3.3.5 Gradient illumination

As discussed at the beginning of 3.3, it is also possible to shape S by shining the RPE with a non-uniform pattern. Figure 3.26 shows the result of such an illumination condition on a retina sample. It is important to notice that the background is not uniform. In order to obtain a weak modulation on a constant background (as previously analyzed), the image has been divided by its low-passed version.

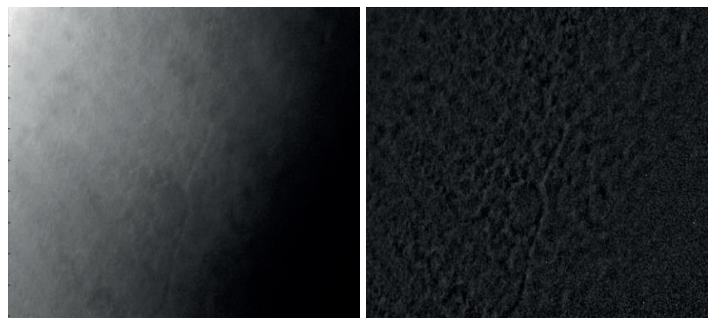


Figure 3.26

Left) Raw image obtained with non-uniform illumination of the RPE and Right) its renormalized version. Each image is $800 \times 800 \mu m^2$.

By using this method for providing contrast, it is possible to tune r without changing the illumination angle. This also means that the change in contrast due to backdiffraction of retinal features is expected to be negligible. In Figure 3.27, it is possible to observe how the contrast follows almost a linear behavior respect to the r parameter as expected from the mathematical model and simulations.

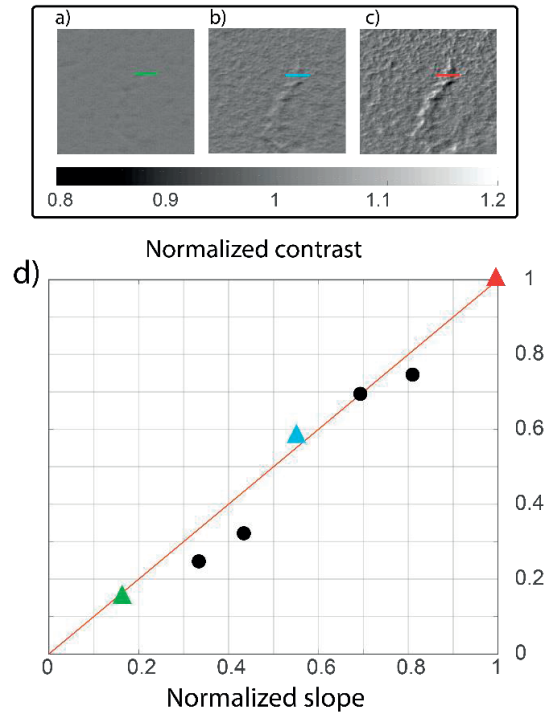


Figure 3.27

a-c) retina samples for different illumination condition. Each image is $240 \times 240 \mu m^2$. The colored bars are the areas used for calculating the contrast displayed in figure f. d) Plot of the measured contrast versus the normalized slope. The values coming from images a-c are shown as triangles, while the others are shown as black points. Error bar is smaller than the showed points. The continuous line is the expected theoretical model.

3.4 Conclusion

In this chapter, I studied how illumination affects phase contrast in retinal samples. The theoretical model has been developed based on the work of Tian. Within the model, the phase transfer function has been analyzed under different conditions and resulted in isolating the parameter r (the ratio between the illumination's slope and its average) as proportional to the image contrast. This has been tested also with simulations, showing the same behavior for different pupil shape and also for non-linear illuminations.

Experiments have been conducted on human eye samples using two different type of illumination. Oblique illumination has been used to provide a constant illumination function along the retina. Even if the direct proportionality between r and retinal contrast has been showed for a transmission configuration, the configuration in reflection provided poor linearity. Indeed, probably due

to the effect of backdiffraction of retinal features, retinal contrast followed strongly non-linear pattern. It was however possible to show how, on average, by increasing r also the contrast increases.

The linear behavior in reflection has been showed by using non-uniform illumination of the RPE. In this case, by means of a linear illumination, it was possible to tune r without changing the illumination angle, and so backdiffraction of the retinal features stayed constant.

For the following ex-vivo and in-vivo experiments, oblique illumination will be used.

Chapter 4 Image reconstruction

In this chapter, I study how the phase profile can be reconstructed quantitatively (up to a constant factor) from the qualitative phase contrast images analyzed in the previous section. Indeed, with the knowledge of the transfer functions and the assumption of a ramp-like illumination and the WOA, it is possible to reconstruct a quasi-quantitative phase image.

In section 4.1, I discuss the reconstruction technique proposed by Tian and why this is not directly applicable to retinal imaging. In 4.2 and 4.3, I modify Tian's model for image formation and adapt it to the retinal case. In section 4.4, I show how the reconstruction method can be used to acquire high quality quasi quantitative phase images of different retinal structures in ex-vivo samples. These ex-vivo images have been obtained in collaboration with Dr. Timoth   Laforest.

This chapter contains work described in the arXiv publication: "A new microscopy for imaging retinal cells." A version has been sent to a peer reviewed journal for publication in January 2018.

4.1 Tian's method for reconstruction

Tian's reconstruction method starts with the non-normalized image, modeled as:

$$\tilde{I}_{[S,P]}(\mathbf{u}) = B_{[S,P]}\delta(\mathbf{u}) + H_{[S,P]}(\mathbf{u})\tilde{\mu}(\mathbf{u}) + G_{[S,P]}(\mathbf{u})\tilde{\phi}(\mathbf{u}) \quad (4.1)$$

Assuming we know B , H and G , the two unknowns are the two functions μ and ϕ . This is a linear system with two unknowns, so it can be solved by two linearly independent equations. Furthermore, if we are only interested in the phase ϕ , it is possible to use the symmetry of the two illumination functions S_1 and S_2 such that $S_1(\mathbf{u}') = S_2(-\mathbf{u}')$. The resulting transfer functions are then: $H_{[S_1,P]}(\mathbf{u}) = H_{[S_2,P]}(\mathbf{u})$ and $G_{[S_1,P]}(\mathbf{u}) = -G_{[S_2,P]}(\mathbf{u})$. By subtracting the two images, the resulting image depends only on the phase term ϕ as:

$$\tilde{I}_{[S_1,P]}(\mathbf{u}) - \tilde{I}_{[S_2,P]}(\mathbf{u}) = 2G_{[S_1,P]}(\mathbf{u})\tilde{\phi}(\mathbf{u}) \quad (4.2)$$

Here, Tian defines the differential phase contrast (DPC) image as:

$$I_{DPC}(\mathbf{x}) \triangleq \frac{I_{[S_1,P]}(\mathbf{x}) - I_{[S_2,P]}(\mathbf{x})}{I_{[S_1,P]}(\mathbf{x}) + I_{[S_2,P]}(\mathbf{x})} \quad (4.3)$$

Such an expression is obtained by assuming that the absorption and phase have weak modulations. Consequently, the sum at the denominator can be approximated in the real space as: $I_{[S_1,P]}(\mathbf{x}) + I_{[S_2,P]}(\mathbf{x}) \sim 2B$. This results in the product between ϕ and the normalized transfer function:

$$\tilde{I}_{DPC}(\mathbf{u}) \sim \frac{G_{[S_1,P]}(\mathbf{u})}{B} \tilde{\phi}(\mathbf{u}) = g_{[S_1,P]}(\mathbf{u}) \tilde{\phi}(\mathbf{u}) \quad (4.4)$$

Such a problem is analogous to an image deconvolution problem, in which direct inversion (i.e. dividing \tilde{I}_{DPC} by g) has been shown to be highly prone to noise [148]. Indeed, direct inversion results in a strong amplification of the frequencies whose amplitudes are close to 0, amplifying not only the signal, but also the image noise. Furthermore, g is zero for all the frequencies \mathbf{u} perpendicular to \mathbf{v}_ϕ . This means that the data obtained from the two images are not sufficient for the reconstruction of all frequencies.

Tian solved this problem by acquiring at least two couple of images (with each couple showing symmetrical illumination) and by using a least square minimization problem. Indeed, by calling the n -th DPC image $\hat{I}_{DPC,n}(\mathbf{u})$ and $g_n(\mathbf{u})$ its normalized phase transfer function, the reconstructed phase ϕ_{reg} satisfies the condition:

$$\min \sum_n |\tilde{I}_{DPC,n}(\mathbf{u}) - G_n(\mathbf{u}) \tilde{\phi}(\mathbf{u})|^2 + \psi |\tilde{\phi}_{reg}(\mathbf{u})|^2 \quad (4.5)$$

Where ψ is a parameter used for regularization. This problem can then be rewritten as:

$$\tilde{\phi}_{reg}(\mathbf{u}) = \frac{\sum_n G_n^*(\mathbf{u}) \tilde{I}_{DPC,n}(\mathbf{u})}{\sum_n |G_n(\mathbf{u})|^2 + \psi} \quad (4.6)$$

It is important to remark that such a solution is not directly applicable to the retinal case. Indeed, Tian uses an illumination coming from a display far enough to obtain a plane wave of uniform intensity in the object plane. This is not the case for the retina, where the non-uniformity of the background (due to both illumination and different reflectance of eye regions) produces a non-uniform intensity at the object's plane. Furthermore, the effect of backdiffraction of the retina, due to the reflection configuration should be taken into account for a proper analysis. This will be further discussed in the following section.

4.2 Retinal image formation model

In this section, I show a modified version of Tian's model for image formation adapted for retinal imaging in reflection. This is done by taking into account the proximity of the RPE to the retina and by considering that light passes twice through the volume to be imaged. To do this it is convenient to analyze the path of light through the retina.

When light arrives on an object plane within the retina, its intensity can be modeled as a spatial profile $i(x)$. Here, two different signals are generated: the backdiffracted $D(x)$ and transmitted light. When the transmitted light arrives at the RPE plane it can be described by a new intensity map that is, in general, different from i . However, due to the high transmittance of the neuroretina and the proximity between the object plane and the RPE plane, the intensity profiles at the two planes can be considered similar, up to a lateral translation (see Figure 4.1). In the following, I will assume i to be a slowly varying function (i.e. $i(x) \sim i(x + \delta x)$) and thus the effect of the lateral shift is neglected. This is, for example, the case of transscleral illumination, which diffuses light in a relatively uniform way. Thus, by using x' as the spatial coordinate of the RPE plane, the intensity at the RPE plane will be then written as $i(x')$.

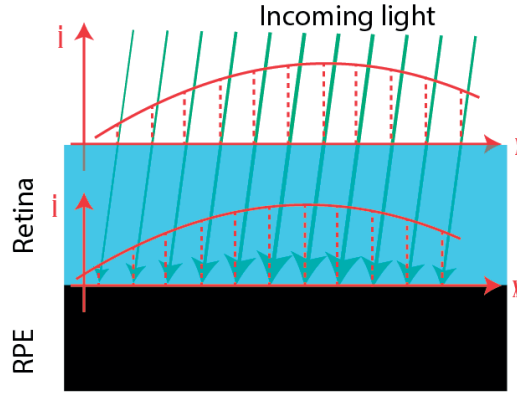


Figure 4.1

Intensity at the retina plane and at the RPE plane. It is possible to observe a small shift between the two.

At the RPE plane, each point x' generates backscattered light with an angular profile $b_{x'}(u')$. x' represents the spatial coordinate over the RPE plane, while u' is the angular coordinate (or, equivalently the spatial coordinate of a parallel plane in the far field, as shown in Figure 4.3). The light backscattered from the RPE is also modulated in its intensity by the local reflectance $\rho(x')$. This

means that each point in the RPE is considered as a new source of intensity $\rho(x') i(x')$ and angular spectrum $b_{x'}(\mathbf{u}')$.

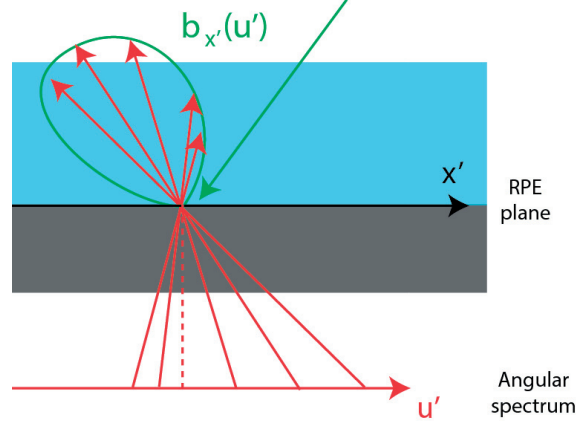


Figure 4.2

Graphical representation of the angular spectrum $b_{x'}$ of the light scattered from RPE point x' .

A point x on an object plane in the retina receives an illumination of angular frequency \mathbf{u}' from the RPE point $x' = x + d'\mathbf{u}'$, where d' is the distance between the object plane and the RPE plane (see Figure 4.3). The angular spectrum which illuminates the point x can be written as $S_x(\mathbf{u}') = \rho(x + d'\mathbf{u}') i(x + d'\mathbf{u}') b_{x+d'\mathbf{u}'}(\mathbf{u}')$. To have a better understanding of the contributions to the angular spectrum, it is convenient to analyze it for the two imaging modalities discussed in chapter 3.

If ρ and i are constant and b does not depend on the angle coordinate, then $S(\mathbf{u}') = \rho i b(\mathbf{u}')$. This is the case of the uniform illumination of the background where the shape of the illumination function coincides with the one of the light backscattered from a single point.

If ρ and b are constant (at least for small values of \mathbf{u}'), then $S_x(\mathbf{u}') = \rho b i(x + d'\mathbf{u}')$. By limiting our attention to the case $x = 0$, the angular spectrum coincides with the intensity at the RPE plane. This is the case of gradient-illumination analyzed in chapter 3. This also similar to Tian's formulation, since for Tian, the LED plane is far away respect to the object plane. Indeed, if $x \ll d'\mathbf{u}'$ then $x' \sim d'\mathbf{u}'$.

This is equivalent to consider image formation for different small areas separated by a distance greater than Δ . Since each area presents the same s , the difference between each section is the local modulation \bar{S} .

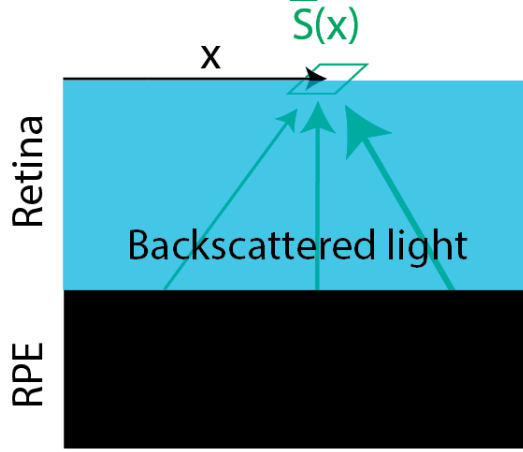


Figure 4.4

Representation of \bar{S} for a point x .

Furthermore, the final image contains also the contribution of the scattered light from the cellular structure within the retina (on the first light pass), which is modulated by the initial intensity i . So, the resulting image can be written as:

$$I_{[S,P,i]}(x) = \bar{S}(x)[B_{[S,P]} + \tilde{H}_{[S,P]}(x) * \mu(x) + \tilde{G}_{[S,P]}(x) * \phi(x)] + i(x)D(x) \quad (4.11)$$

This model is used in the following section to understand image normalization and phase reconstruction.

4.3 Normalization

In this section, I describe how an image of the form of (4.11) can be normalized to obtain a DPC expression similar to Tian in (4.3).

I split the analysis in two parts. In section 4.3.1, I analyze how the spatial modulation of the image $\bar{S}(x)$ affects the results and which normalization method can be used. In 4.3.2 I analyze the effect of backdiffraction (the term $i(x)D(x)$) on the reconstruction.

In the next sections, the dependence on the pupil will not be written, so that functions like $G_{[S,P]}$ are written as $G_{[S]}$. Furthermore, I will now introduce the functions H' and G' to keep the formulas compact:

$$\begin{aligned} H'_{[S]}(\mathbf{x}) &\triangleq B_{[S]} + \tilde{H}_{[S]}(\mathbf{x}) * \mu(\mathbf{x}) \\ G'_{[S]}(\mathbf{x}) &\triangleq \tilde{G}_{[S]}(\mathbf{x}) * \phi(\mathbf{x}) \end{aligned} \quad (4.12)$$

4.3.1 Effect of the illumination intensity modulation

Since the image formation in reflection does not have the same form as introduced by Tian for transmission, I will first analyze how this will affect Tian's normalization method. This is achieved by taking the images (4.10) (with the term " $i(\mathbf{x})D(\mathbf{x})$ " removed for now) and forming the DPC image I^{DPC} with two different illumination S_1 and S_2 , such that $s_1(\mathbf{u}') = s_2(-\mathbf{u}')$. Furthermore, the two \bar{S} are, in general, different. So I^{DPC} can be written as:

$$I^{DPC}(\mathbf{x}_c) = \frac{[\bar{S}_1(\mathbf{x}) - \bar{S}_2(\mathbf{x})]H'_{[S_1]}(\mathbf{x}) + [\bar{S}_1(\mathbf{x}) + \bar{S}_2(\mathbf{x})]G'_{[S_1]}(\mathbf{x})}{[\bar{S}_1(\mathbf{x}) + \bar{S}_2(\mathbf{x})]H'_{[S_1]}(\mathbf{x}) + [\bar{S}_1(\mathbf{x}) - \bar{S}_2(\mathbf{x})]G'_{[S_1]}(\mathbf{x})} \quad (4.13)$$

Where H' and G' are the functions defined in (4.12).

Unless $\bar{S}_1(\mathbf{x}) \sim \bar{S}_2(\mathbf{x})$ this result is different to what is obtained by Tian. This means that it cannot be used in (4.6) to reconstruct the original phase and that a different method should be found. Since \bar{S} is a low frequency modulation, if μ and ϕ are high frequency function, then by low-passing the image it is obtained:

$$Low\{I_{[S]}(\mathbf{x})\} \sim \bar{S}(\mathbf{x})B_{[S]} \quad (4.14)$$

Then, the normalized image can be obtained as:

$$\frac{I_{[S]}(\mathbf{x})}{Low\{I_{[S]}(\mathbf{x})\}} = 1 + \tilde{h}_{[S]}(\mathbf{x}) * \mu(\mathbf{x}) + \tilde{g}_{[S]}(\mathbf{x}) * \phi(\mathbf{x}) = J_{[S]}(\mathbf{x}) \quad (4.15)$$

Then, since J is already correctly normalized, it is possible to define a J^{DPC} as the difference of two J functions and obtain:

$$J^{DPC}(\mathbf{x}) = \tilde{g}_{[S_1]}(\mathbf{x}) * \phi(\mathbf{x}) \quad (4.16)$$

Where the two illumination functions are such that $s_1(\mathbf{u}') = s_2(\mathbf{u}')$.

Such an expression is equivalent to Tian's I^{DPC} , so it can be used to reconstruct the phase in (4.6). In the following, this method will be used to reconstruct the phase profile.

4.3.2 Effect of the backdiffraction from the first pass illumination

In this section, the backdiffraction term D is taken into account. If the lowpass image is not affected by the diffraction term (i.e. D contains only higher frequencies than the filter's cutoff frequency), the normalized imaged can be written as:

$$\frac{I_{[s_1]}(\mathbf{x})}{Low[I_{[s_1]}(\mathbf{x})]} = 1 + \tilde{h}_{[s_1]}(\mathbf{x}) * \mu(\mathbf{x}) + \tilde{g}_{[s_1]}(\mathbf{x}) * \phi(\mathbf{x}) + \frac{i_1(\mathbf{x})}{\bar{S}(\mathbf{x})B_{[s_1]}} D_1(\mathbf{x}) \quad (4.17)$$

Since S is proportional to i , with i as a slowly varying function, it is possible to write \bar{S} as:

$$\bar{S}(\mathbf{x}) \sim i(\mathbf{x}) \beta_{[\rho, b, P]}(\mathbf{x})$$

Where β is a function that depends only on the sample parameters (ρ and b) and on the pupil function P . Thus (4.17) can be written as:

$$\frac{I_{[s_1]}(\mathbf{x})}{Low[I_{[s_1]}(\mathbf{x})]} = 1 + \tilde{h}_{[s_1]}(\mathbf{x}) * \mu(\mathbf{x}) + \tilde{g}_{[s_1]}(\mathbf{x}) * \phi(\mathbf{x}) + \frac{D_1(\mathbf{x})}{\beta(\mathbf{x})B_{[s_1]}} \quad (4.18)$$

This solution, in general, do not guarantee a DPC image containing only the phase term, as (4.15). Indeed, the diffraction term D depends on the angle of illumination. Thus, two different illumination points can produce two different diffraction terms. This is consistent with the strong contrast variations measured in 3.3.4.

4.3.3 Phase reconstruction simulations

In this section, I will simulate phase reconstruction for a uniform and non-uniform illumination. Simulations have been performed using MATLAB. Both the values for the phase image ϕ and for the values of the absorption image μ range between 0 and 1. The chosen phase image is a series of bars. High frequency has been chosen to avoid overlap with the slow frequency modulation. After convolving μ with h and ϕ with g , the two images are summed on a uniform background and then multiplied by the image \bar{S} (from (4.11)). The resulting image in the following is called "phase contrast image." In the case of uniform illumination, \bar{S} is constant along the space. The phase reconstruction used in this section has four images obtained with four different illumination functions. Each

illumination function s is rotated by 90° with respect to the previous one. The final image is the normalized between 0 and 1.

The same process is repeated for all the four illumination functions, obtaining four different phase contrast images. The four images are then renormalized using either Tian's normalization (I^{DPC} from (4.2)), or with the low-pass renormalization (J^{DPC} from (4.16)).

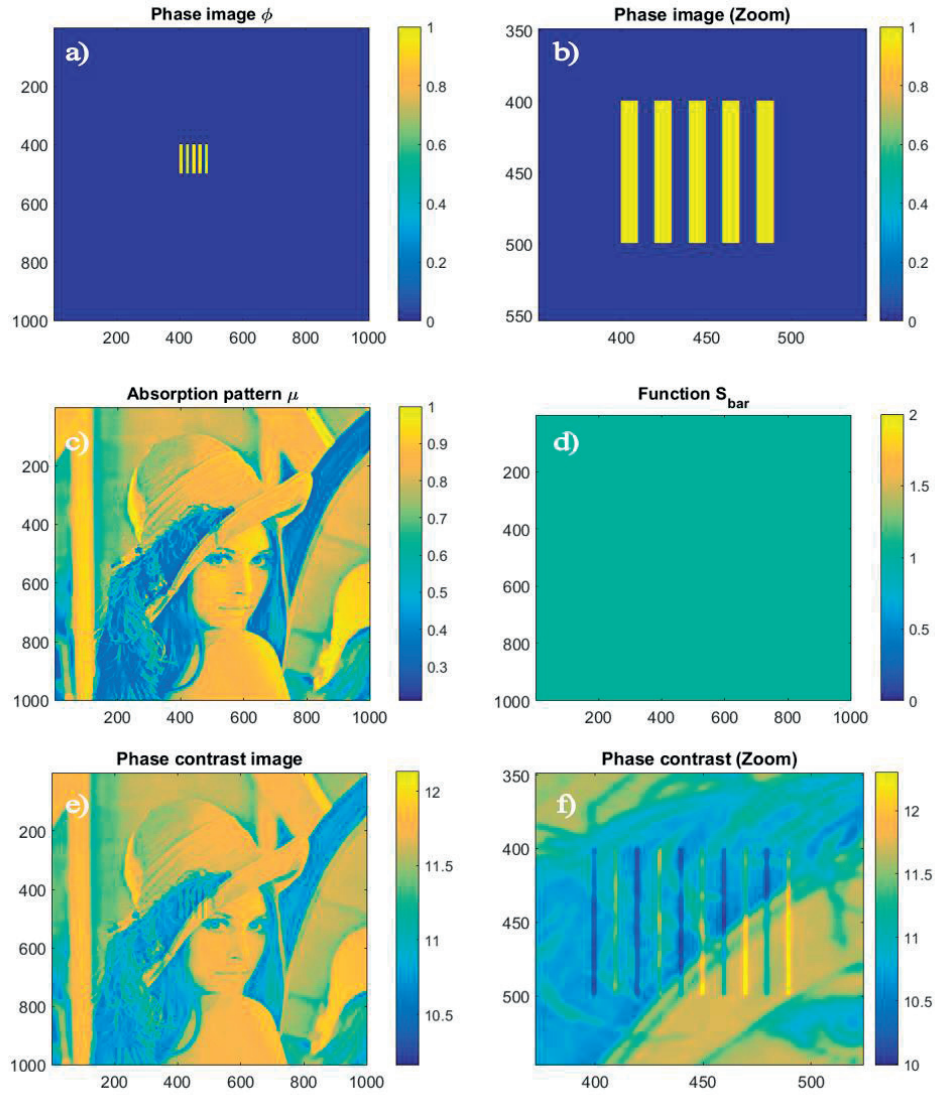


Figure 4.5

a) Phase term ϕ . b) Zoomed phase term. c) Absorption term μ . d) \bar{S} function. e) phase contrast image. f) Zoomed phase contrast image.

Figure 4.6 shows the result in case of uniform illumination. Since the phase image contains also some low frequencies it is affected by the filter, which produces some distortion in the reconstructed image (darker area around the bars).

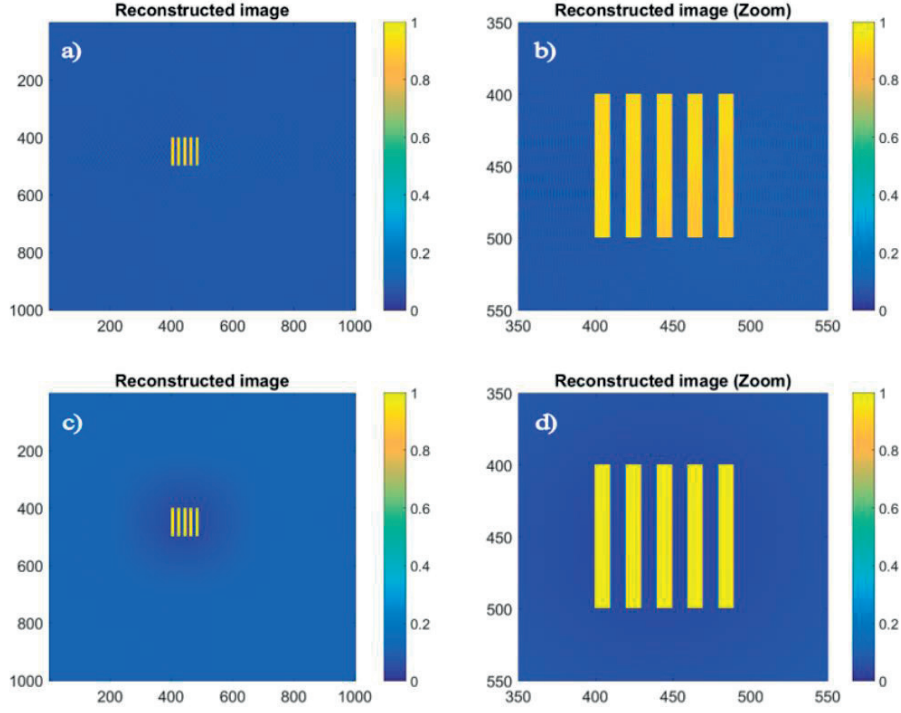


Figure 4.6

a-b) reconstructed image with Tian's normalization in case of uniform illumination. c-d) Reconstruction with lowpass filtering. The filtering process introduces a small distortion close to the target.

In the case of non-uniform illumination, \bar{S} is chosen as a linear function, whose orientation is randomly chosen. This is done to simulate different illumination conditions depending on the illumination direction. One of the used \bar{S} and the obtained phase contrast image are showed in Figure 4.7.

Figure 4.8 shows the reconstructed images in the two cases. None of the images contain the absorption term. However, the image normalized with Tian's method still contains a low frequency signal which strongly distorts the final result. This is not the case for the low-pass method, which still contains some distortions, but strongly decrease their contribution. Since the reconstructed images have been normalized between 0 and 1, their amplitude is only proportional to the real phase.

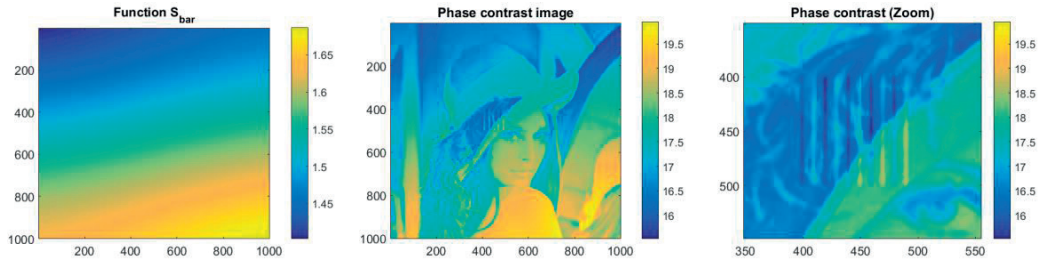


Figure 4.7

Left) \bar{S} in case of non-uniform illumination. Center) The obtained phase contrast image. Right) Zoom of the phase contrast image.

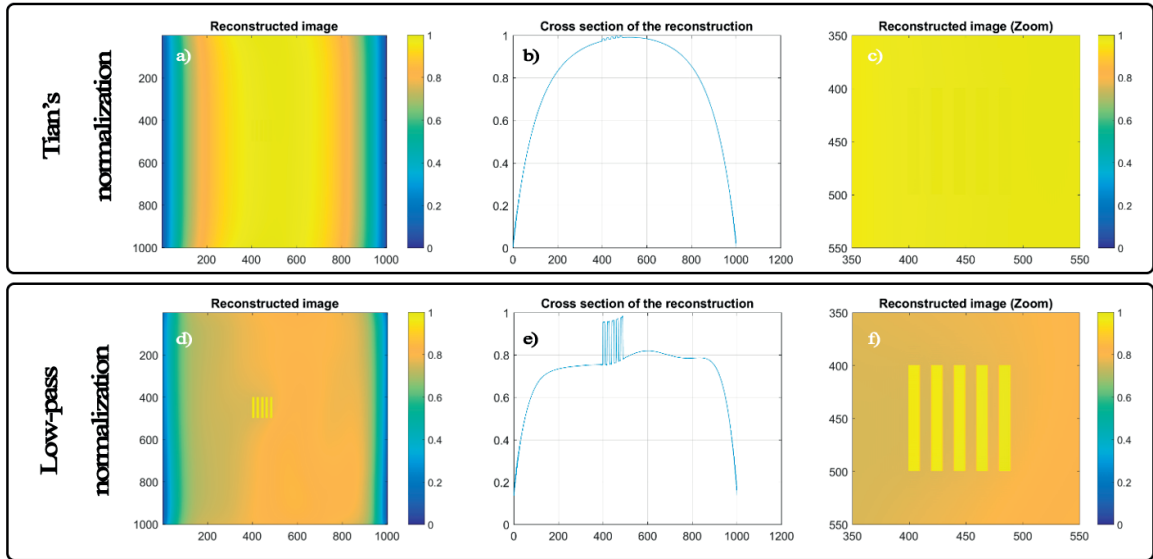


Figure 4.8

a) DPC image using Tian's method. b) Its cross section. c) Zoomed image. d-f) Same set of images in by using low-pass normalization.

In this section, I showed how J^{DPC} can be used to recover a quasi-quantitative phase image. In the following the normalization by the low-passed image is used for reconstruction.

4.4 Ex-vivo experiments

In this section, the acquisition system is tested on ex-vivo retinal samples and compared with other state of the art imaging techniques. I would like to acknowledge Dr. Timoth   Laforest at LAPD with whom I collaborated for the acquisition of the images of this section.

All the acquired images have been renormalized using the previously discussed low-pass method. To provide better contrast, retinal images have been reconstructed with an 8-points reconstruction (4 axis instead of 2). For each illumination point, 100 images have been averaged together to produce a higher SNR image.

The first set of images have been acquired on sections of a pig's neuroretina sample with a 10X, 0.25 NA objective. This numerical aperture has been chosen because it is close the numerical aperture of a fully dilated human eye (~ 0.24 NA). The Light Emitting Diodes (LEDs) have a 50 nm spectral bandwidth centered around a wavelength of 650 nm. A sheet of paper has been placed on the bottom of the microscope slide as the scattering layer.

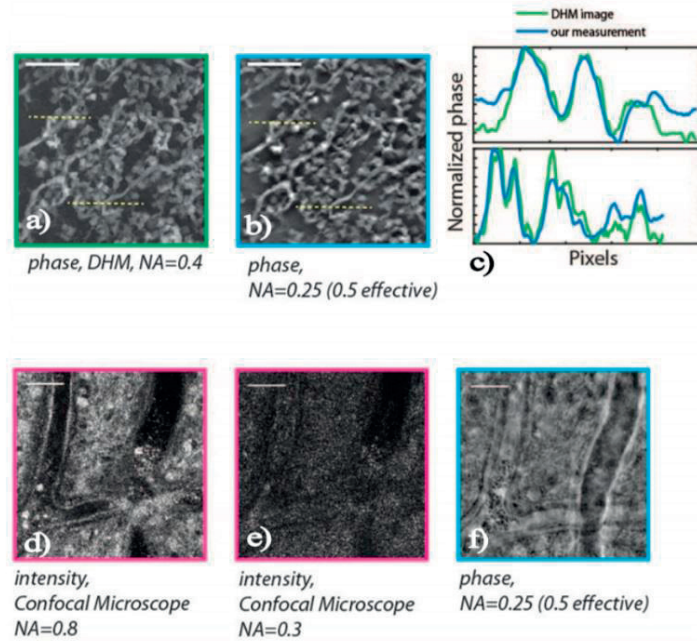


Figure 4.9

a) Phase image of a 10 μm thick slice of pig retina inner nuclear layer obtained with a DHM. b) Phase image obtained with the proposed method. c) Horizontal cross section plot of quantitative phase comparison. Scale bars = 30 μm . d-e) Confocal image of a flat-mounted human choroid and retina taken with a 0.8 NA and 0.3 NA objective respectively. f) Corresponding phase image with 0.25 NA objective, corresponding to a 0.5 effective NA. Scale bars = 50 μm .

Images of the same samples were acquired also with a digital holographic microscope (DHM), a coherent imaging method which produces quantitative phase images. Images from the DHM are taken with a 0.4 NA microscope objective to compare it with the effective 0.5 NA of the oblique illumination. Indeed, since this method uses incoherent illumination, it presents an effective numerical aperture that is twice the one of the microscope objective. This can be also seen from the fact that even if the pupil function has a maximum radius of a , the two transfer functions are non-zero up to $2a$.

Figure 4.9 shows a comparison with an image taken with confocal microscopy in reflection. This image has been acquired on a human retina-choroid complex. Confocal images were acquired with both a 0.3 and a 0.8 NA objective, while the phase image was acquired with a 0.25 NA objective. Also in this case, images were normalized with the low-pass method. The phase image shows comparable results with the 0.8 NA confocal.

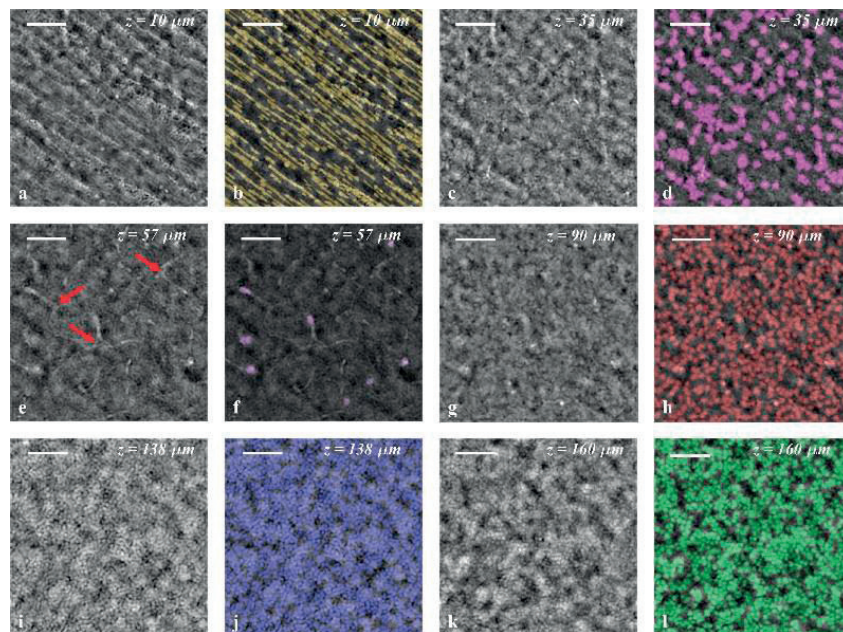


Figure 4.10

Scan in depth of flat-mounted choroid and retina of a pig's eye. a, c, e, g, i, k: raw phase images. b, d, f, h, j, l: phase images with digitally tagged cells and structures. Nerve fiber layer ($z = 10 \mu\text{m}$) a, b. Ganglion cells layer ($z = 35 \mu\text{m}$) c, d. Inner plexiform layer, with microglia (red arrows) ($z = 57 \mu\text{m}$) e, f. Inner nuclear layer ($z = 90 \mu\text{m}$) g, h. Outer nuclear layer ($z = 138 \mu\text{m}$) i, j. Inner and outer photoreceptors segments interface ($z = 160 \mu\text{m}$) k, l. Scale bars = $50 \mu\text{m}$.

Figure 4.10 shows a series of images acquired at different depth of a pig's choroid complex in the region called *area centralis*. In this case, the backscattered light come from the RPE-choroid layers and no paper was placed on the glass slide.

Images of different layers have been digitally stained to identify nuclei and to estimate cellular density. From the data, a ganglion cell density of $2'260 \text{ cells/mm}^2$ and a mean cone density of $20'930 \text{ cells/mm}^2$ has been estimated. This data is consistent with the ganglion cell densities (1500 to 4000 cells/mm^2 , [149]) and the cones densities (19'000 [150] to 22'600 [151] cells/mm^2) that have been reported in the literature.

Imaging of ganglion cells and pericytes was also tested in immunostained rat neuroretina. Phase images were acquired with a 0.4 NA microscope objective (thus, with 0.8 effective NA), while fluorescent images were acquired using a 0.8 NA objective. LEDs were placed in such a way as to provide a uniform sample illumination. Nuclei of the ganglion cells (showed in blue in the fluorescent image) are clearly visible also in the phase contrast image. Furthermore, it is possible to observe some area of stronger signal (marked with red arrows) where pericytes are present.

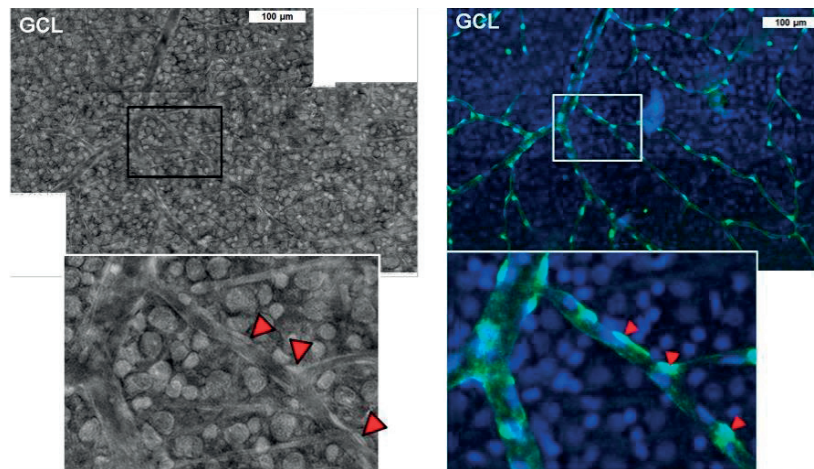


Figure 4.11

Correlation between phase and fluorescence imaging of the pericytes, shown with red triangles, and ganglion cells.

This analysis shows that such a system can be used to obtain quasi-quantitative images of ex-vivo retina samples.

Chapter 5 In-vivo experimentation

In this chapter, I discuss the case of in-vivo imaging. These measurements present major challenges that were not present in ex-vivo imaging namely: the maximum possible exposure (MPE) to light without damaging the eye, eye optical aberrations and eye motion. In this chapter, I discuss how these challenges can be solved for in-vivo imaging while using transscleral illumination. This illumination modality has been chosen to provide angled illumination.

In section 5.1, I will discuss eye safety for transscleral illumination. In 5.2 I will discuss the in-vivo results and in 5.3, I will draw my conclusions.

5.1 Eye safety for transscleral illumination

When dealing with the living eye, special care should be taken to avoid damages. Because of that, safety standards have been introduced when dealing with skin and retinal safety. These standards can be found in documents such as the guidelines from the International Commission on Non-Ionizing Radiation Protection (ICNIRP). However, these guidelines are not designed for transscleral illumination, thus a way to adapt these standards is here analyzed. The analysis discussed in this section has been used as part of a protocol approved by the Cantonal Ethics Committee of Vaud (Switzerland).

5.1.1 Introduction on Eye safety

Safety standards for visible and invisible radiation are used to determine the maximum possible light exposure (MPE) for eye and skin. This section only describes how to relate illumination safety to the case of transscleral illumination. For a detailed description of the safety regulations for infrared radiation, I suggest to read the ICNIRP guidelines and their adaptation to medical instruments [152, 153].

All wavelength may produce thermal damage. Meaning that the temperature rise due to light absorption can result in tissue damage. For ultraviolet and visible radiation, photochemical reactions may also produce retinal damage. However, in the following, the analysis will be conducted for infrared radiation only. This is chosen because infrared provides higher transmittance of the sclera than visible wavelength. Furthermore, it is an invisible radiation, thus making a diagnostic instrument more comfortable.

The exposure time and size of the illuminated retinal area are key parameters in safety standards. The exposed area is usually considered circular and identified by its diameter d_r . More often, safety standards do not directly use the spot diameter, but rather the angle under which it is subtended: ω (see Figure 5.1)

Different MPE values are given in the ICNIRP guidelines depending on the size of ω and the exposure time. Regarding the area, the most restrictive ranges are the one in which the exposed area exceeds 0.1 rad . Indeed, in small areas, heat diffusion lowers the local rise of temperature, better than for large exposed areas.

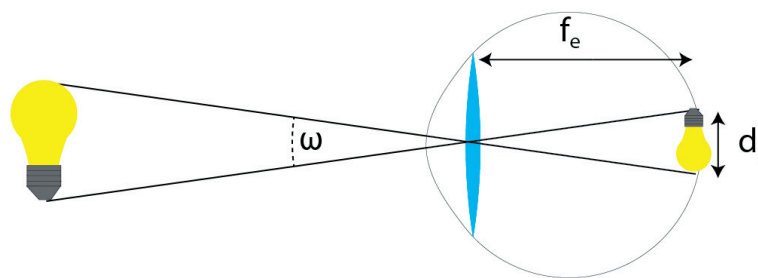


Figure 5.1

Representation of the scheme used in the ICNIRP guidelines.

In the case of transscleral illumination, light will pass through the retina twice (see Figure 5.2). In case of a collimated or diverging beam, due to strong scattering contribution, the first illuminated retinal area is smaller than the second (in the figure $A_1 < A_2$). Thus, by defining the irradiance as the radiant flux (or power) per unit area, the first surface on the sclera A_1 has a higher retinal irradiance than the second surface on the retina. This can be estimated also by supposing Lambertian emission at the surface. Let us call E_1 the irradiance at the first area A_1 and E_3 the irradiance over an area A_3 (see Figure 5.2). Choosing identical size for both areas ($A_3 = A_1$), the irradiance at the retina E_3 can be obtained as [154]:

$$E_3 = E_1 \sin^2(\theta) \quad (5.1)$$

Where θ is the angle under which A_3 is subtended (see Figure 5.2).

Then by using a diameter of 2 mm and a distance between the two surfaces of 17 mm , the ratio E_3/E_1 is equal to 0.34% . Because of that, in the following, the effects on the second area will be neglected. The limiting MPE is thus determined by the first surface A_1 . Although this decreases

the maximum possible irradiance on the imaged area of the retina, I will show that it is still sufficient to acquire retinal images.

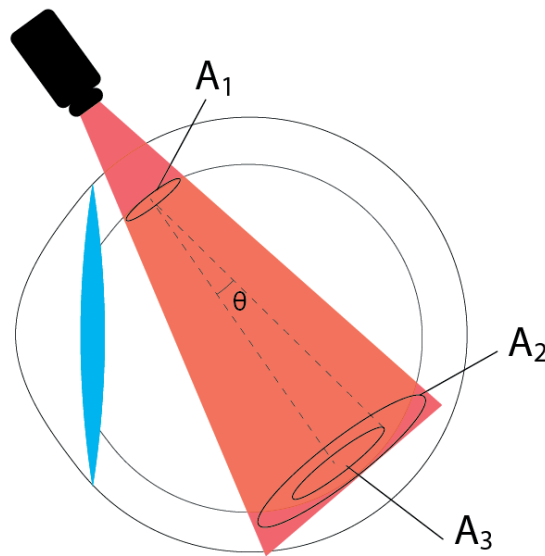


Figure 5.2

Representation of the scheme used in the ICNIRP guidelines.

The value of MPE in the ICNIRP guidelines for the irradiance needs to be first multiplied by a so-called “hazard function”. Such a function depends only on the illumination wavelength λ . Different hazard functions are used in the case of thermal and photochemical effects. However, since this analysis will focus on the infrared case, only the thermal hazard function will be considered.

5.1.2 MPE for transscleral illumination

In the following I will use the term “transscleral illumination” to mean an illumination method in which light passes through the sclera. An illumination method in which light is transmitted through the eyelid (and so also through the sclera) is referred as “transpalpebral illumination.” Since the calculations for the MPE are almost identical for the two cases, I will make my analysis on the transscleral case, pointing out which parameters should be adapted for the transpalpebral case.

Here, MPE for transscleral illumination are obtained from transpupillary illumination standards. The irradiance and the exposed area are computed for transscleral illumination. These values

can directly be used to estimate the MPE from the guideline. Figure 5.3 shows graphically the equivalence of the two cases.

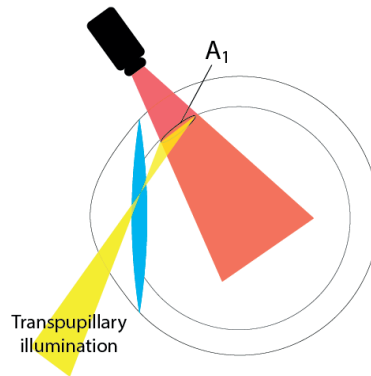


Figure 5.3

Transpupillary and transscleral illumination

To estimate the exposed retinal area and the irradiance, let us introduce the following quantities:

- d_s , the diameter of the illumination spot at the skin
- d_r , the diameter of the illumination spot at the retina
- θ_0 , divergence angle of the source in free space
- θ_s , divergence of light inside the media
- T_s , thickness of the biological medium (sclera and eventually skin)
- τ , is the transmittance of the biological medium (sclera and eventually skin)
- A_1 , the exposed retinal area
- E_{ret} , retinal irradiance in the exposed area (measured in $\left[\frac{W}{m^2}\right]$)
- E_{MPE} , the maximum possible irradiance obtained from the guidelines.

I will now introduce some approximations to perform calculations for the worst-case scenario (e.g. non-absorbing eye media). The approximations are the following:

1) The diameter of the spot inside the retina d_r is calculated for a flat surface placed 0.5 mm after the sclera (or, for transpalpebral illumination, 1.5 mm after the skin). This is a good approximation when $d_r \ll f_e$ (where f_e , the focal distance of the eye is shown in Figure 5.1).

2) Skin, muscles and sclera are approximated as perfectly transmissive, non-scattering media. This means that light reaches the retina with the same angular distribution as the one in air. Since these media have a scattering angle $\theta_s > \theta_0$, the assumption that $\theta_s = \theta_0$ represents an overestimation for the delivered irradiance.

3) Absorbance of skin, sclera and choroid is considered equal to 0. This is represented by the transmission parameter τ set equal to 1. In real eyes $\tau < 1$, so this assumption generates an overestimation of the retinal irradiance at the eye.

4) Thermal effects on sclera (and eventually eyelids) are modeled from thermal effects on skin. Meaning that thermal damage can occur only when the irradiance of these surfaces exceeds the maximum possible exposure for skin presented in the ICNIRP guidelines. This appears to be a reasonable assumption, since the ICNIRP guidelines presents no distinction or special case for the different external surfaces of the body.

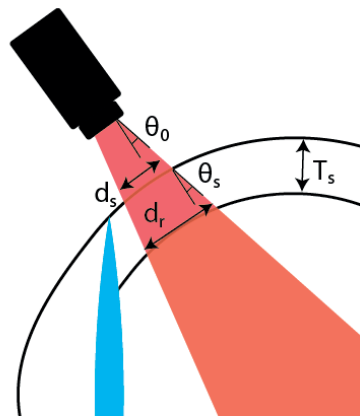


Figure 5.4

Scheme of the geometrical parameters used for analyzing the MPE in the case of transscleral illumination.

To summarize, the hypothesis 1 to 3 **overestimate** the delivered irradiance at the eye. This is visible also in different illumination configurations as showed in Figure 5.5.

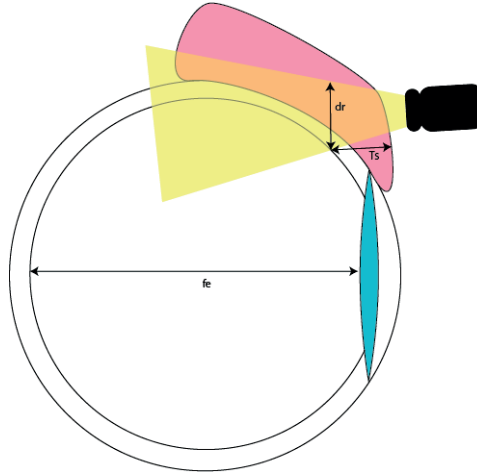


Figure 5.5

Special case of transpalpebral illumination in which part of the light is not passing through the eye. If the power density is calculated at distance T_s , it is clear how the estimated power density could only be higher than the real power density at the retina.

By taking into account the previous approximations, the retinal spot diameter and area can be calculated just as:

$$\begin{cases} d_r = d_s + T_s \tan(\theta_s) \\ A_r = \pi \left(\frac{d_r}{2} \right)^2 \end{cases} \quad (5.2)$$

Since the transmission of the biological layers has been set to 1 ($\tau = 1$), the (overestimated) delivered irradiance can be calculated as the beam's power divided by A_r .

As mentioned in the introduction, the obtained value needs to be weighted with the thermal hazard function. The MPE values in the case of large exposed areas (worst case) are summarized in Table 5.1 for different time ranges.

	$t < 10 \text{ s}$ [W/cm ²]	$t > 10 \text{ s}$ [W/cm ²]
E_{therm}	$5.88 t^{-0.25}$	0.71

Table 5.1

Maximum possible exposure for thermal and photochemical calculated for large sources [152].

5.1.3 Comparison with known cases

Even if no standards for transscleral illumination are proposed in the main guidelines, transscleral and transpalpebral illumination methods are already used in some studies and devices. Here, I report the case of a device called Panoret-1000 [131, 133]. This device has been approved by the American Food and Drugs Administration (FDA). Furthermore, its use appears in scientific publications from groups operating in the United States of America [155, 156] and in Switzerland [131].

The second relevant case is a study on transpalpebral illumination [133]. In this case the study was approved by the Institutional Review Board of Antalya Training and Research Hospital and was declared in compliance with the Declaration of Helsinki.

	Transmission media	Skin irradiance* ¹ [w/cm ²]	Sclera irradiance* ¹ [w/cm ²]	Weighted retinal photothermal irradiance [w/cm ²]
Panoret-1000 [156, 131]	Sclera	/	1* ³	0.87* ⁴
Toslak [133]	Skin and sclera	0.07	/	0.06 * ⁵
MPE limits (from the analysis in section 5.1.2)	/	0.35	0.35	0.71

Table 5.2

*1 Calculated without taking into account the hazard function

*2 Calculated by weighting the exposure with the aphakic hazard curve (that is more restrictive or equal to the values of the blue hazard function).

*3 Estimated for a power of 200 mW exiting a 5 mm diameter rod (both values declared in the manual)

*4 Estimated for a diverging angle of 40° (not specified in the manual)

*5 Obtained from the values declared in the article and considering a transmittance equal to 1 (instead of the 2% transmittance considered in the article).

The values from the two cases are summed up in Table 5.2 and compared with the maximum exposure discussed in the previous section. The study on transpalpebral illumination reports values well below the MPE, while the values from Panoret-1000 exceeds it. This may come either from the overestimation of the calculated irradiance (discussed in previous section) or from the use of

different standards. The approval of a device whose values are calculated to be higher than the MPE computed in the previous section is a confirmation that such MPE values are conservative.

5.2 Experimental tests

An in-vivo setup has been realized in collaboration with Dr. Timoth   Laforest and Mr. Mathieu Kunzi to test the technique in-vivo. This section contains work described in the arXiv publication “A new microscopy for imaging retinal cells” [157]. A version has been sent to a peer reviewed journal for publication in January 2018.

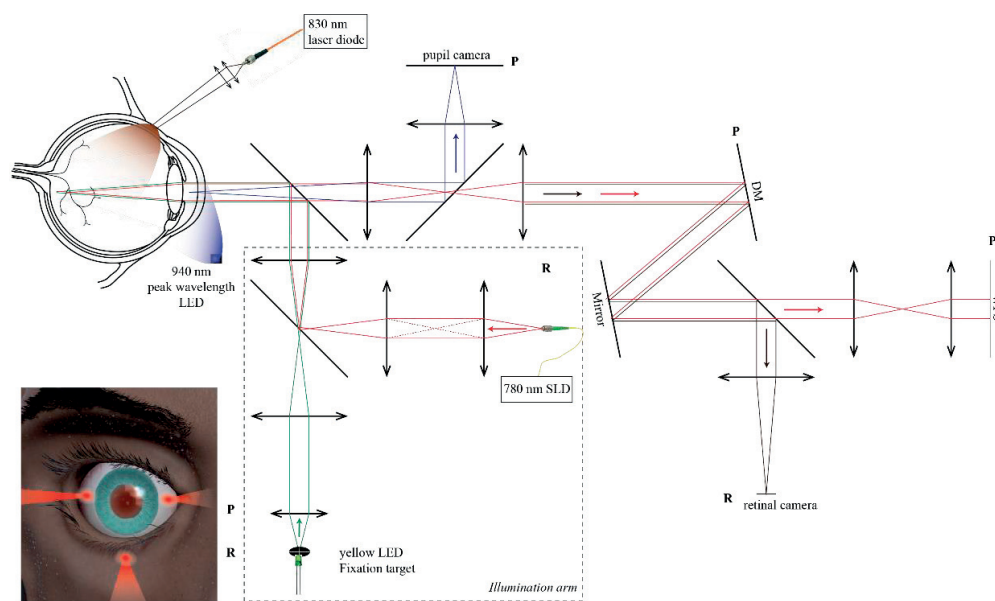


Figure 5.6

Schematic of the in vivo phase imaging system. The digital photography represents transscleral and transpalpebral illuminations by means of a focused beam on the sclera or on the skin of the inferior eye lid. Light is then transmitted inside the eyeball. After scattering off the eye fundus, the light passing through the retinal cell layers is collected through the pupil of the eye. The optical setup includes an adaptive optics loop to correct the aberration of the eye. DM, Deformable mirror; LED, light-emitting diode; SLD, superluminescent diode; WFS, wavefront sensor.

For the in vivo demonstration, the angled illumination on the retina is produced by two laser diode beams illuminating the sclera successively on the temporal side and the nasal side of the sclera, at a 15 mm distance from the pupil center (see Figure 5.6). The obtained angle of illumination is therefore approximately 40°. The illumination arm is also composed of a yellow fixation target, of a 780 nm Superluminescent Diode (SLD) providing a point source at the retina plane and of an

infrared LED for illuminating the pupil uniformly. The imaging arm integrates a pupil camera and an adaptive optics feedback loop (Mirao 52e deformable mirror and associated wavefront sensor, Imagine Eyes). The retinal sCMOS camera (ORCA Flash, Hamamatsu) collects the light from the transscleral illumination to image the eye fundus with a sampling of $1\ \mu\text{m}/\text{pixel}$.

Once the eye is aligned to the setup, the retinal camera, mounted on a translation stage, is adjusted to focus on a retina layer. The depth sectioning is here limited by the depth of field, which is given by the pupil size and the aberrations of the eye. For instance, for an aberration free 6 mm pupil, the depth of field is 27 μm , for a lateral resolution of 2.9 μm .

The single center study aiming at validating the performances of the phase imaging device adheres to the tenets of the Declaration of Helsinki. The protocol involving healthy human subjects was approved by the local Ethics Committee of the Swiss Department of Health on research involving human subjects (CER-VD N°2017-00976). The present study reports the examination of one 49-year-old male subject, with a healthy retina.

A sequence of approximately five thousand images, covering twelve different layer depth in the retina, is acquired by turning successively the laser diode spots ON and OFF with an 8 ms exposure time and a frame rate of 16 Hz. The distance between successive depths is 12 μm (half of the depth of field) to have a best focused image of each layer. A single layer takes 25 seconds to image which is suitable for clinical application. The images from each illumination point are averaged after computing the shift due to eye motion using a registration algorithm [158]. The phase image is reconstructed using the normalization method introduced in chapter 4.

Figure 5.7 shows the eye fundus observed with the experimental in vivo phase imaging device (Figure 5.7 b-e). The processed images from one illumination point are acquired at the nerve fiber layer (Figure 5.7 b, e), and the RPE layer (Figure 5.7 d, g). Thanks to oblique illumination, the RPE layer appears well contrasted avoiding the Stiles-Crawford effect [30] that occurs in standard transpupillary illumination [159]. I attribute the high RPE contrast to the oblique illumination which is highly transmitted through the photodetector layer and, at the same time, the boundaries of the RPE cells diffuse light which is collected by the pupil. Figure 5.8 shows the in-vivo RPE cells at different eccentricity from the fovea. The graphs on the right in Figure 5.8. show the RPE density and area. These values are comparable to previously reported values [107], as well as the row to row spacing extracted from the Fourier analysis, shown in Figure 5.9. Figure 5.10 shows the

enhancement of the contrast over noise ratio (CNR) with respect to the number of frame averaged. Figure 5.11 is a comparison of dark field images of RPE cells obtained in-vivo on human and ex-vivo on pig.

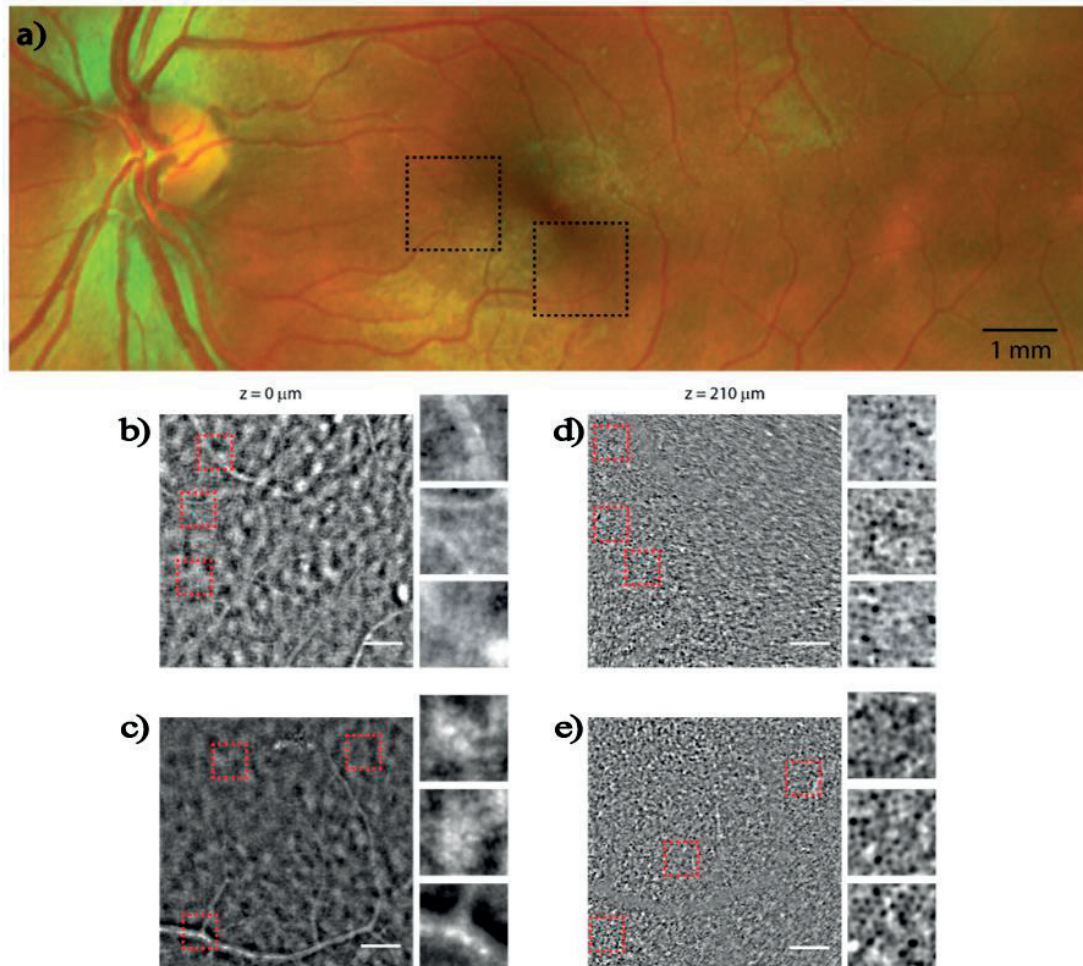


Figure 5.7

In vivo retina imaging of one healthy volunteer. (a) Left eye fundus on scanning laser ophthalmoscope (Optos). (b-c) in vivo phase images of the two areas highlighted with black squares on the eye fundus, at 1.5 mm eccentricity from the fovea, at three different depths into the retina: nerve fiber layer (d, e) and retinal pigment epithelium. Scale bars = 200 μm . The patches are 125 μm x 125 μm . Acquisition was performed with a non-mydratic pupil of 4 to 6 mm diameter, in dark room conditions.

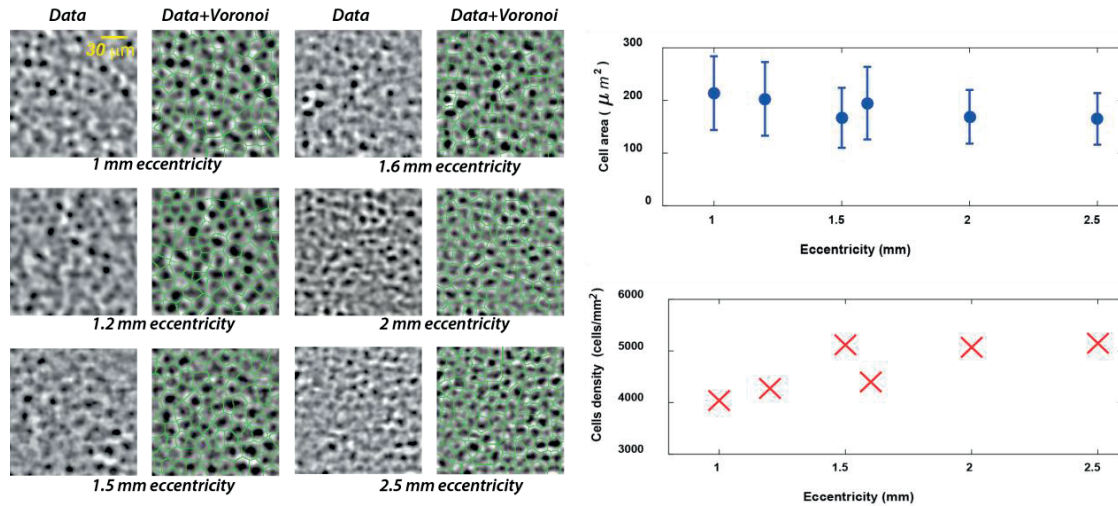


Figure 5.8

Density and area analysis of the RPE cells. Data and overlap with a Voronoi filter at different eccentricities (Left). Cells density and Area (Right).

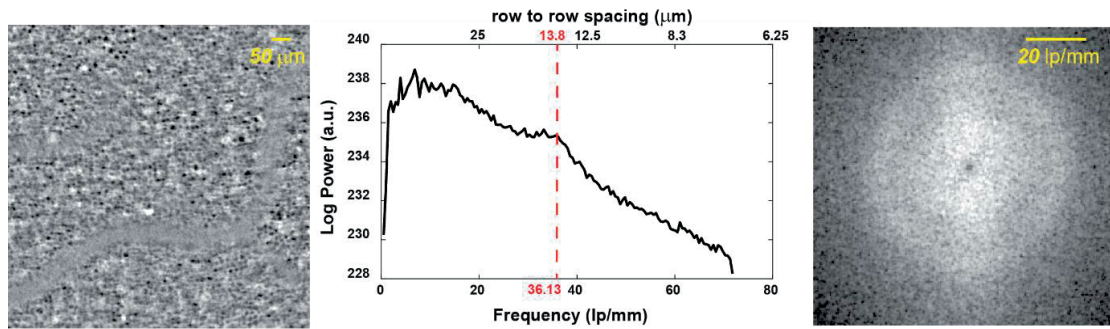


Figure 5.9

Fourier analysis of the RPE layer image centered at 7° from the fovea. Dark field image high pass filtered to enhance the visualization (Left). Axial profile of the spectrum (Center). Spectrum of the left image cropped at 6.8 μm row to row spacing (Right). The peak signature of the RPE signal is located at 13.8 μm , which is consistent with the values found in the literature.

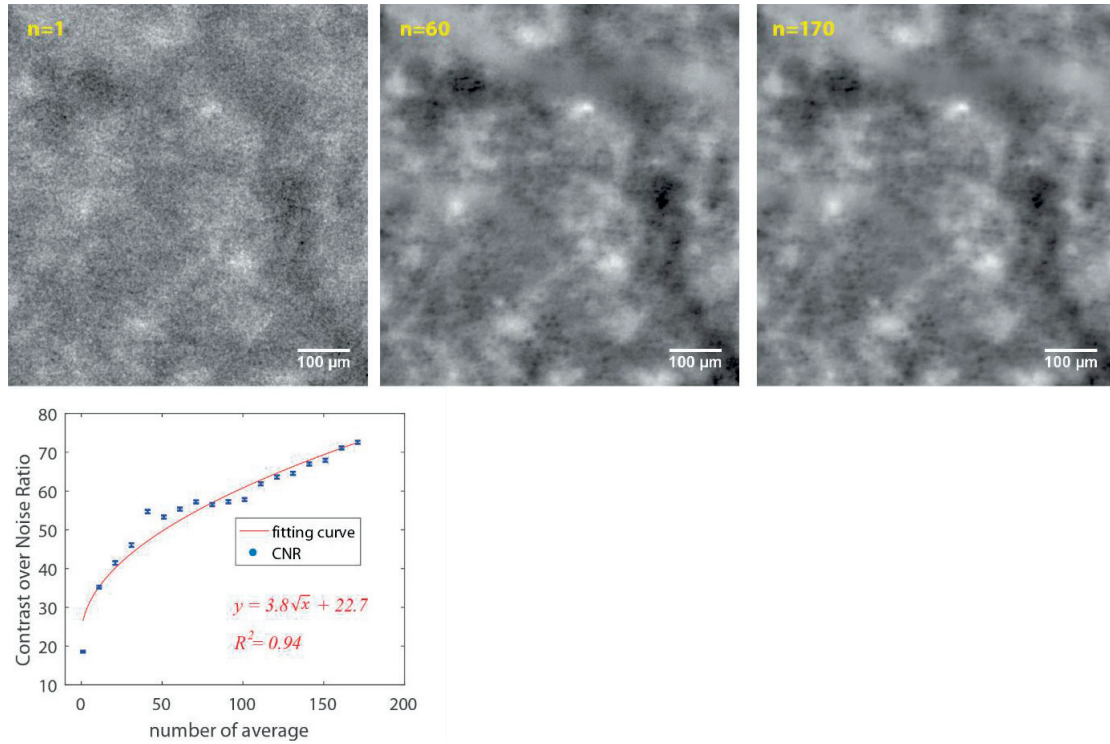


Figure 5.10

Figure 11. Averaging of the RPE layer image centered at 7° from the fovea. Dark field images are aligned before averaging.

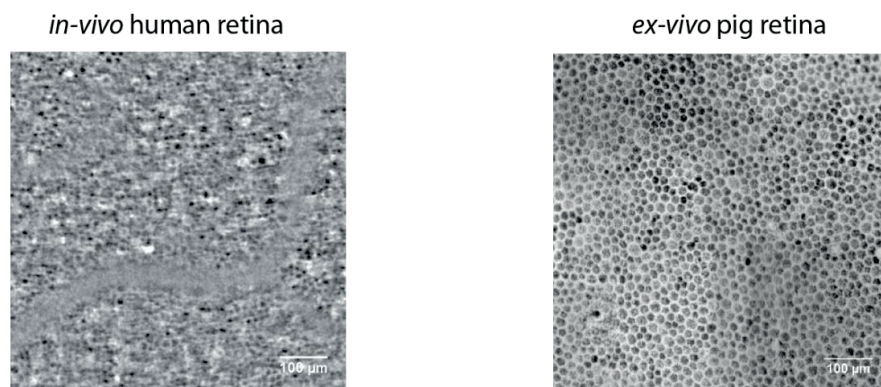


Figure 5.11

In-vivo and ex-vivo comparison of dark field images of the RPE layer. In-vivo human RPE with ~ 5 mm diameter pupil, illumination with 830 nm peak wavelength laser diode (Left). Ex-vivo pig RPE registered with 0.4 NA 20X microscope objective illumination with 850 nm peak wavelength LED (Right).

5.3 Conclusion

In this chapter, I discussed the use of transscleral illumination to provide in-vivo phase contrast. In the first part, I discussed eye safety for this specific configuration, adapting the ICNIRP standards. The resulting method has been used as part of a protocol approved by the Cantonal Ethics Committee of Vaud (Switzerland).

In vivo tests have been performed. Current results show the possibility of fast acquisition of absorption retinal features (such as RPE cells). Phase structures have not yet been well resolved. With further optimization of the instrument such as higher SNR raw images combined with automated image processing for averaging the images, I expected to obtain in vivo images showing phase structures. The proposed method could be complementary to OCT and the combination of both may result in accelerating our understanding of retinal diseases and validating morphological endpoint for therapeutic evaluation, but also the understanding of other neuro degenerative diseases.

Chapter 6 Conclusion

In this thesis, I proposed and analyzed a system and an instrument and method for *en face* retinal imaging. The system is a wearable scanning ophthalmoscope which has been tested through simulations and with a proof of concept setup. The instrument and method use the backscattered light from the RPE to provide phase contrast either by means of oblique illumination or by non-uniform illumination of the eye fundus. Here, I will discuss my achieved results in these two fields and what we may expect from future developments.

6.1 Achieved results

The wearable ophthalmoscope has been studied with simulations and a proof of concept setup. Good agreement between theory and experiment has been found, showing an imaging lateral resolution of $\sim 15 \mu m$. The setup has been realized in such a way that the key components (holographic plate and micromirror) are placed at the same distance as they would be in wearable glasses. The holographic plate allows for a see-through system. However, it also distorts the beam which is the main reason that the fundus images were not diffraction limited. This distortion could be compensated during the hologram writing and also by designing a custom illumination for the read-out. The system has been used to acquire a full frame of an ex-vivo eye sample in 3 seconds. Such a time scale would be too slow for eye-tracking in practice. However, if instead of a full frame, the acquisition is reduced to a circle of 0.5 mm diameter (as done in some eye tracking systems [101]), the acquisition speed can rise up to 150 Hz which would then be sufficiently fast.

The instrument and method for phase imaging required a more complex analysis and represented the bulk of this thesis. This has been done thanks to the use of a mathematical model initially developed by Tian for a transmission like microscope. Due to the scattering properties of the eye fundus, the illumination was approximated to a linear function. It was then possible to extract the key parameters linked to phase contrast. The robustness of this approximation was tested with simulations (also outside the ramp approximation) and experiments.

Quasi quantitative phase image reconstruction was also studied by modelling and experiments. Non-uniform illumination of the retina occurs in practice due non-uniform reflectivity of the eye fundus. I showed by theory and simulations that it produced artifacts in the reconstructed

image. However, thanks to a renormalization by a low pass filter, it was possible to strongly decrease the non-uniform illumination effect.

The in vivo case has been studied taking into account eye safety. The use of an adaptive optics loop in the in vivo system compensated for eye aberrations. The exposure time of 8 ms was chosen to strongly decrease motion artifacts. The system has then been tested in vivo in a human subject demonstrating enough resolution to observe, for the first time to my knowledge, images of in-vivo human RPE cells obtained in less than 25 seconds.

6.2 Future development

For the wearable system, the proposed scanning system has been developed to work with a 515 nm wavelength (green). For a completely disturbance free system, a wavelength in the infrared should be used. However, the possibility of having it in a system strongly depends on the photopolymer. Indeed, a photopolymer sensitive to the infrared should be developed.

Another limitation of the implemented system regards the range of ocular shift that still allow image acquisition. Indeed, the beam enters in the eye cavity thanks to the pupil aperture and, when the eye moves, the pupil is also shifted with respect to the beam. This means that some eye orientation would not allow the beam to enter the eye. If tracking over a wide range of angles is needed, a different solution should be found. Resonant micromirrors could be also used to improve acquisition speed.

Regarding the phase contrast imaging method, the in-vivo system showed the possibility of observing intensity pattern at cellular resolution (RPE and photoreceptors). However, the phase signal has still not been well resolved, meaning that more research is still needed. This can be done either by improving the current system (e.g. finding better illumination conditions to improve the SNR of raw images), or by testing alternative solutions (such as non-uniform transpupillary illumination).

The use of polarization has not yet been used. It is known that some cellular layers in the retina are bi-refrigent and thus rotate the polarization of the light. Thus, by polarizing the illumination light and placing a polarizer in front of the camera, one could expect to obtain a better contrast in some cellular layers.

A detailed study on the anatomy of the eye could also provide a more efficient approach. Indeed, the thickness of the different eye layers is not uniform. Thus, by detecting eye regions with higher transmittance, the SNR could be improved.

The effect of aberrations can also be studied. This could be either an alternative to the adaptive optics loop or an improvement. Indeed, depending on the speed and precision of the loop, many acquired images may still not be diffraction limited. Thus, by knowing the aberrated transfer function, it would be possible to deconvolve the images to obtain a diffraction limited resolution.

References

- [1] W. L. Wong, X. Su, X. Li, C. M. Cheung, R. Klein, C. Cheng, T. Y. Wong “Global prevalence of age-related macular degeneration and disease burden projection for 2020 and 2040: a systematic review and meta-analysis” *Lancet Glob Health.* 2(2), 2014.
- [2] J. W. Crabb, M. Miyagi, X. Gu, K. Shadrach, K. A. West, H. Sakaguchi, M. Kamei, A. Hasan, L. Yan, M. E. Rayborn, R. G. Salomon, and J. G. Hollyfield “Drusen proteome analysis: An approach to the etiology of age-related macular degeneration,” *Proc Natl Acad Sci U.S.A.*, 99(23), 2002
- [3] M. Koronyo-Hamaoui, Y. Koronyo, A. V. Ljubimov, C. A. Miller, M. K. Ko, K. L. Black, M. Schwartz, and D. L. Farkas, “Identification of amyloid plaques in ex vivo retinas of Alzheimer's patients and noninvasive in vivo imaging of retinal plaques in the mouse model,” *Neuroimage*, 54(Supplement 1), S204-S2017, 2011.
- [4] L. R. Molnar, J. V. Odom, B. G. DeRoos, and C. J. Kolanko, “Ocular scanning instrumentation: rapid diagnosis of chemical threat agent exposure,” in *Proceedings of SPIE 5403, Sensors, and Command, Control, Communications, and Intelligence (C3I) Technologies for Homeland Security and Homeland Defense III*, E.D. Carapezza, ed. (SPIE, 2004)
- [5] J. Lemos, G. R. Sadeghnia, I. Olafsdottir, and O. Jensen, “Measuring Emotions Using Eye Tracking”, in *Proceedings of Measuring Behavior*, A. Spink et al., ed. (Noldus, 2008)
- [6] M. Vidal, J. Turner, A. Bulling, H. Gellersen “Wearable eye tracking for mental health monitoring,” *Computer Communications* 35, 2012.
- [7] L. Zhang, X. Y. Li, W. Huang, K. Liu, S. Zong, X. Jian, P. Feng, T. Jung, and Y. Liu “It Starts with iGaze: Visual Attention Driven Networking with Smart Glasses” in *MobiCom’14 Proceedings of the 20th annual international conference on Mobile computing and networking*, ed. (ACM, 2014).
- [8] S. G. Schuman, A. F. Koreishi, S. Farsiu, S. Jung, J. A. Izatt, C. A. Toth, “Photoreceptor Layer Thinning over Drusen in Eyes with Age-related Macular Degeneration Imaged In Vivo with Spectral Domain Optical Coherence Tomography,” *Ophthalmology*. 116(3), 2009.
- [9] D. A. Antonetti, R. Klein, T.W. Gardner, “Diabetic retinopathy.” *N. Engl. J. Med.* 366(13) 2012.
- [10] Z. Liu, K. Kurokawa, F. Zhang, J. J. Lee, and D. T. Miller “Imaging and quantifying ganglion cells and other transparent neurons in the living human retina,” *PNAS* 114(48), 2017.

- [11] H. Jonas, "The nobility of sight," *Philosophy and Phenomenological Research* Vol. 14(4), 1954 .
- [12] T. Cronin "Seeing without eyes," *Scientific American* 13 August 2017.
- [13] R. S. Snell, M. A. Lemp, "Clinical Anatomy of the Eye, Second Edition," Blackwell Science Ltd, 2013
- [14] B. Cassin, S. Solomon, "Dictionary of Eye Terminology," Triad Publishing Company, 1990.
- [15] R. A. Serway, J. W. Jewett, "Physics for Scientists and Engineers with Modern Physics, Fifth Edition," Saunders College Publishing, 2000.
- [16] J. W. Rohen, E. Lutjen-Drecol, C. Yokochi, "Color Atlas of Anatomy: A photographic study of the human body, 7th edition" LWW, 2010.
- [17] C. Clemente "Gray's Anatomy of the Human Body, 30th edition)," Lea & Febiger 1985
- [18] K. M. Meek, N. J. Fullwood, "Corneal and scleral collagens—a microscopist's perspective" *Micron*. 32(3), 2001.
- [19] P. Fratzl, "Collagen, structure and mechanics," Springer, 2008.
- [20] S. Peters, T. Lamah, D. Kokkinou, K. U. Bartz-Schmidt, U. Schraermeyer, "Melanin protects choroidal blood vessels against light toxicity," *Z. Naturforsch. C.*, 61(5-6), 2006.
- [21] S. Y. Schmidt, R. D. Peisch, "Melanin concentration in normal human retinal pigment epithelium. Regional variation and age-related reduction," *IOVS* 27(7), 1986.
- [22] J. J. Weiter, F. C. Delori, G.L. Wing, K. A. Fitch, "Retinal Pigment Epithelial Lipofuscin and Melanin and Choroidal Melanin in Human Eyes," *Invest Ophthalmol Vis Sci.*, 27(2), 1986.
- [23] R. Acharya, E. Y. K. Ng, J. S. Suri, "Image Modeling of the Human Eye," Artech House, 2008.
- [24] Ng, E. Y. K. "Human Eye Imaging and Modeling," CRC Press, 2012.
- [25] K. Franze, J. Grosche, S. N. Skatchkov, S. Schinkinger, Ch. Foja, D. Schild, O. Uckermann, K. Travis, A. Reichenbach, J. Guck, "Müller cells are living optical fibers in the vertebrate retina," *PNAS* 104(20), 2007.
- [26] A. Reichenbach, K. Franze, S. Agte, S. Junek, A. Wurm, J. Grosche, A. Savvinov, J. Guck, S. N. Skatchkov "Live Cells as Optical Fibers in the Vertebrate Retina," on *Optical Fiber Technology*, InTech, 2012.
- [27] D. Purves, G. J. Augustine, D. Fitzpatrick, F. C. Katz, A. LaMantia, J. O. McNamara, S. M. Williams, "Neuroscience, 2nd edition," Sinauer Associates, 2001.

- [28] D.A. Baylor, T. D. Lamb, K. W. Yau, "Responses of retinal rods to single photons." *J Physiol*, 288, 1979.
- [29] G. Wyszecki, W. S. Stiles, "Colour Science: Concepts and Methods, Quantitative Data and Formulae, 2nd edition," Wiley-Interscience, 1981.
- [30] W. S. Stiles, B. H. Crawford, "The luminous efficiency of rays entering the eye pupil at different points," *Proc. R. Soc. Lond.*, 112, 1933.
- [31] G. Westheimer, "Directional sensitivity of the retina: 75 year of Stiles-Crawford effect", *Proc Biol Sci.*, 275, 2008.
- [32] L. Erskine, E. Herrera, "Connecting the Retina to the Brain," *ASN Neuro.*, 6(6), 2014.
- [33] A. W. Dreher, K. Reiter, R. N. Weinreb, "Spatially resolved birefringence of the retinal nerve fiber layer assessed with a retinal laser ellipsometer," *Applied optics*, 19(31), 1992.
- [34] T. Y. P. Chui, H. Song, C. A. Clark, J. A. Papay, S. A. Burns, A. E. Elsner, "Cone Photoreceptor Packing Density and the Outer Nuclear Layer Thickness in Healthy Subjects," *Invest Ophthalmol Vis Sci.*, 53(7), 2012.
- [35] S. A. Baker, V. Kerov "Photoreceptor Inner and Outer Segments," *Current Topics in Membranes*, 72, 2013.
- [36] R. Mathew, R. Bafiq, J. Ramu, E. Pearce, M. Richardson, E. Drasar, S. L. Thein, S. Sivaprasad, "Spectral domain optical coherence tomography in patients with sickle cell disease," *Br J Ophthalmol.*, 99(7), 2015.
- [37] R. W. Baloh, A. W. Sills, W. E. Kumley, V. Honorubia, "Quantitative measurement of saccade amplitude, duration, and velocity," *Neurology.*, 25(11), 1975.
- [38] M. Rucci, P. McGraw, R. Krauzlis, "Fixational eye movements and perception". *Vision Research.*, 2016.
- [39] H. Collewijn, E. Kowler, "The significance of microsaccades for vision and oculomotor control," *J Vis.*, 8(14), 2008.
- [40] C. Cherici, X. Kuang, M. Poletti, M. Rucci, "Precision of sustained fixation in trained and untrained observers," *Journal of Vision*, 12(6), 2012.
- [41] M. Aytakin, J. D. Victor, M. Rucci, "The visual input to the retina during natural head-free fixation," *Journal of Neuroscience*, 34(38), 2014

- [42] P. J. Foster, Y. Jiang, "Epidemiology of myopia," *Eye (Lond.)*, 28(2), 2014
- [43] J. Wons, M. A. Wirth, N. Graf, M. D. Becker, S. Michels, "Comparison of Progression Rate of Retinal Pigment Epithelium Loss in Patients with Neovascular Age-Related Macular Degeneration Treated with Ranibizumab and Aflibercept," *J. Ophth.*, 2017, 2017.
- [44] T. Grüter, M. Grüter, C. Carbon, "Neural and genetic foundations of face recognition and prosopagnosia," *J Neuropsychol.*, 2(Pt.1), 2008.
- [45] S. Mehta "Age-Related Macular Degeneration," *Prim Care.*, 42(3), 2015.
- [46] Facts About Age-Related Macular Degeneration "https://nei.nih.gov/health/maculardegen/armd_facts," last review 21 Jan. 2018.
- [47] M. M. Engelgau, L. S. Geiss, J. B. Saaddine, J. P. Boyle, S. M. Benjamin, E. W. Gregg, E. F. Tierney, N. Rios-Burrows, A. H. Mokdad, E. S. Ford, G. Imperatore, K. M. Narayan, "The evolving diabetes burden in the United States," *Ann Intern Med.*, 140(11), 2004.
- [48] R. N. Weinreb, T. Aung, F. A. Medeiros, "The pathophysiology and treatment of glaucoma: a review," *JAMA*. 311(18), 2014.
- [49] S. Resnikoff, D. Pascolini, D. Etaya'ale, "Global data on visual impairment in the year 2002," *Bull World Health Organ.*, 82(11), 2004.
- [50] R. Conlon, H. Saheb, I. I. Ahmed, "Glaucoma treatment trends: a review," *Can J Ophthalmol.*, 52(1), 2017.
- [51] A. Sommer, J. M. Tielsch, J. Katz "Relationship between intraocular pressure and primary open angle glaucoma among white and black Americans. The Baltimore Eye Survey," *Arch Ophthalmol.*, 109(8), 1991.
- [52] P. Mitchell, W. Smith K. Attebo, P. R. Healey, "Prevalence of open angle glaucoma in Australia–The Blue Mountains Eye Study," *Ophthalmology*, 103(10), 1996.
- [53] R. S. Harwerth, L. Carter-Dawson, F. Shen, E. L. Smith, M. L. Crawford, "Ganglion cell losses underlying visual field defects from experimental glaucoma," *Invest Ophthalmol Vis Sci.*, 40(10), 1999.
- [54] M. F. Cordeiro, E. M. Normando, M. J. Cardoso, S. Miodragovic, S. Jeylani, B. M. Davis, L. Guo, S. Ourselin, R. A'Hern, P. A. Bloom, "Real-time imaging of single neuronal cell apoptosis in patients with glaucoma," *Brain.*, 140(6), 2017.
- [55] R. C. Eagle "Eye Pathology: An Atlas and Text Second Edition," LWW, 2011.

- [56] D. Goldenberg, J. Shahar, A. Loewenstein, M. Goldstein, "Diameters of retinal blood vessels in a healthy cohort as measured by spectral domain optical coherence tomography," *Retina.*, 33(9), 2013
- [57] A. London, I. Benhar, M. Schwartz, "The retina as a window to the brain—from eye research to CNS disorders." *Nature Reviews Neurology*, 9(1), 2013.
- [58] C. La Morgia, F. N. Ross-Cisneros, A. A. Sadun, V. Carelli, "Retinal Ganglion Cells and Circadian Rhythms in Alzheimer's Disease, Parkinson's Disease, and Beyond," *Frontiers in neurology*, 8, 2017
- [59] H. Leung, J. Wang, E. Rohtchina, T. Y. Wong, R. Klein, P. Mitchell, "Impact of current and past blood pressure on retinal arteriolar diameter in an older population," *J Hypertens.*, 22(8), 2004.
- [60] T. Y. Wong, R. Klein, B. E. K. Klein, M. S. Meuer, L. D. Hubbard, "Retinal Vessel Diameters and Their Associations with Age and Blood Pressure," *Invest Ophthalmol Vis Sci.*, 44(11), 2003.
- [61] C. J. Kolanko, L. Molnar, J. V. Odom, J. E. Smith, Patent US 8613710 B2 "Noninvasive method for determining the presence of systemic hypertension in a subject"
- [62] C. Simon, and I. Goldstein, "A New Scientific Method of Identification," *New York State Journal of Medicine*, 35(18), (1935).
- [63] L. Stefanis, " α -Synuclein in Parkinson's Disease," *Cold Spring Harb Perspect Med.*, 2(2), 2012.
- [64], I. Bodis-Wollner, P. B. Kozlowski, S. Glazman, S. Miri, " α -synuclein in the inner retina in parkinson disease," *Ann Neurol.*, 75(6), 2014.
- [65] L. T. Cheng, J. A. Robinson, "Personal Contextual Awareness Through Visual Focus," *IEEE Intelligent Systems*, 16(3), 2001.
- [66] M. Dorr, L. Pomarjansch, E. Barth, "Gaze beats mouse: A case study on a gaze-controlled breakout," *PsychNology Journal*, 7(2), 2009.
- [67] M.I. Posner, and S. Petersen, "The attention system of the human brain," *Annual Reviews of Neuroscience* 13, 1990.
- [68] C. E. Velazquez, K. E. Pasch, "Attention to Food and Beverage Advertisements as Measured by Eye-Tracking Technology and the Food Preferences and Choices of Youth," *Journal of the Academy of Nutrition and Dietetics*, 114(4), 2014.
- [69] TobiiPro, Tobii Pro Glasses 2: <http://www.tobii.com/product-listing/tobii-pro-glasses-2/>. Last review 21 Jan. 2018.

- [70] H. Hoerauf, C. Wirbelauer, C. Scholz, R. Engelhardt, P. Koch, H. Laqua, R. Birngruber, "Slit-lamp-adapted optical coherence tomography of the anterior segment," *Graefe's Archive for Clinical and Experimental Ophthalmology*, 238(1), 2000.
- [71] , N. B. Carlson, D. Kurtz (Autore), "Clinical procedures for ocular examination, 4th edition," McGraw-Hill Education, 2015.
- [72] Retinal cameras: <http://www.opthalmologyweb.com/Retina/5740-Digital-Retinal-Camera/>. Last review 21 Jan. 2018.
- [73] RTX1 datasheet: <http://www.imagine-eyes.com/wp-content/uploads/2017/10/M-DCP-019-c-rtx1-e-datasheet.pdf>. Last review 21 Jan. 2018.
- [74] M. B. Garnier, M. Flores, G. Debellemanni re, M. Puyraveau, P. Tumahai, M. Meillat, C. Schwartz, M. Montard, B. Delbosc, M. Saleh "Reliability of cone counts using an adaptive optics retinal camera," *Clin Exp Ophthalmol.*, 42(9), 2014.
- [75] R. H. Webb, G. W. Hughes, O. Pomerantzeff "Flying spot TV ophthalmoscope," *Applied Optics*, 19(17), 1980.
- [76] R. H. Webb, "Confocal optical microscopy," *Rep. Prog. Phys.*, 59(3), 1996.
- [77] R. H. Webb, G. W. Hughes, F. C. Delori "Confocal scanning laser ophthalmoscope" *Applied Optics*, 26(8), 1987.
- [78] A. Roorda, F. Romero-Borja, W. J. Donnelly, H. Queener, T. J. Hebert, M.C.W. Campbell, "Adaptive optics scanning laser ophthalmoscopy," *Opt. Exp.*, 10(9), 2002.
- [79] M. R. Hee, J. A. Izatt, E. A. Swanson, J. G. Fujimoto, "Femtosecond transillumination tomography in thick tissues," *Opt. Lett.*, 18(13), 1993.
- [80] J. Fujimoto, E. Swanson, "The Development, Commercialization, and Impact of Optical Coherence Tomography," *Invest Ophthalmol Vis Sci.*, 57(9), 2016.
- [81] R. Leitgeb, C. K. Hitzenberger, A. F. Fercher "Performance of fourier domain vs. time domain optical coherence tomography," *Opt. Expr.*, 11(8), 2003.
- [82] J. M. Schmitt, "Optical Coherence Tomography (OCT): A Review," *IEEE J. Sele. Quant. Elec.*, 5(4), 1999.
- [83] T. J. Wolfensberger, M. Gonvers, "Optical coherence tomography in the evaluation of incomplete visual acuity recovery after macula-off retinal detachments," *Graefes Arch Clin Exp Ophthalmol.*, 240(2), 2002.

- [84] T. E. de Carlo, A. Romano, N. K. Waheed, J. S. Duker, "A review of optical coherence tomography angiography (OCTA)," *Int. J. Ret. Vit.*, 1(5), 2015.
- [85] Eyequick digital ophthalmoscope: <http://bluerivermedical.com/digital-retinal-cameras/eyequick-digital-ophthalmoscope/>. Last review 21 Jan. 2018.
- [86] iExaminer: <https://www.welchallyn.com/content/welchallyn/americas/en/microsites/iexaminer.html>. Last review 21 Jan. 2018.
- [87] A. Russo, F. Morescalchi, C. Costagliola, L. Delcassi, F. Semeraro, "A novel device to exploit the smartphone camera for fundus photography," *Journal of ophthalmology*, 2015, 2015.
- [88] Retinai website: <https://www.retinai.com>. Last review 21 Jan. 2018.
- [89] M. Fiedewald, S. Wawrzyniak, F. Pallas, "Ein Beitrag zum datenschutzfreundlichen Entwurf biometrischer Systeme," *Datenschutz und Datensicherheit*, 38(7), 2014.
- [90] F. La Rocca, D. Nankivil, T. DuBose, C. A. Toth, S. Farsiu and J. A. Izatt "In vivo cellular-resolution retinal imaging in infants and children using an ultracompact handheld probe," *Nature Photonics* 10, 2016.
- [91] N. D. Shemonski, F. A. South, Y. Z. Liu, S. G. Adie, P. S. Carney, S. A. Boppart "Computational high-resolution optical imaging of the living human retina," *Nature Photonics*, 9, 2015
- [92] E. Lawson, J. Boggess, S. Khullar, A. Olwal, G. Wetzstein, R. Raskar, "Computational retinal imaging via binocular coupling and indirect illumination," in *ACM SIGGRAPH 2012 Posters*, ed. (ACM 2012), 2012.
- [93] A. Samaniego, V. Boominathan, A. Sabharwal, and A. Veeraraghavan, "mobileVision: A Face-mounted, Voice-activated, Non-mydratic "Lucky" Ophthalmoscope," in *proceedings of the Wireless Health 2014*, ed. (Association for Computing Machinery), 2014.
- [94] Vizix website: <https://www.vuzix.com>. Last review 21 Jan. 2018.
- [95] Google Glass website: <https://x.company/glass/>. Last review 21 Jan. 2018.
- [96] A. Bulling, "Wearable EOG goggles: Seamless sensing and context-awareness in everyday environments," *J. Amb. Int. Smart Env.*, 1(2), 2009
- [97] D. A. Robinson, "A Method of Measuring Eye Movement Using a Scieral Search Coil in a Magnetic Field," *IEEE Trans Biomed Eng.*, 10(3), 1963
- [98] J. Sigut, S. Sidha "Iris Center Corneal Reflection Method for Gaze Tracking Using Visible Light," *IEEE Trans Biomed Eng.*, 58(2), 1963.

- [99] Tobii eye tracking display: <https://www.tobii.com/product-listing/tobii-pro-spectrum/>. Last review 21 Jan. 2018.
- [100] K. V. Vienola, B. Braaf, C. K. Sheehy, Q. Yang, P. Tiruveedhula, D. W. Arathorn, J. F. de Boer, A. Roorda "Real-time eye motion compensation for OCT imaging with tracking SLO," *Biomed Opt Express*, 3(11), 2012.
- [101] D. X. Hammer, R. D. Ferguson, C. E. Bigelow, N. V. Iftimia, T. E. Ustun, and S. A. Burns, "Adaptive optics scanning laser ophthalmoscope for stabilized retinal imaging," *Opt. Express*, 14(8), (2006)
- [102] D. X. Hammer, R. D. Ferguson, J. Magill, M. White, A. Elsner, R. Webb, "Image stabilization for scanning laser ophthalmoscopy," *Opt. Expr.*, 10(26), 2002.
- [103] F. Zernike, "Phase contrast, a new method for the microscopic observation of transparent objects," *Physica*, 9(10), 1942.
- [104] S. Pavani, A. R. Libertun, S. V. King, C. J. Cogswell, "Quantitative structured-illumination phase microscopy," *Applied Optics*, 47(1), 2008.
- [105] L. Tian, L. Waller, "Quantitative differential phase contrast imaging in an LED array microscope," *Opt. Expr.*, 23(9), 2015.
- [106] L. Tian, J. Wang, L. Waller, "3D differential phase-contrast microscopy with computational illumination using an LED array," *Opt. Lett.*, 39(5), 2014.
- [107] Z. Liu, L. Tian, S. Liu, L. Waller, "Real-time brightfield, darkfield, and phase contrast imaging in a light-emitting diode array microscope," *J. Biomed. Opt.*, 19(10), 2014.
- [108] S. B. Mehta, C. J. Sheppard, "Quantitative phase-gradient imaging at high resolution with asymmetric illumination-based differential phase contrast," *Opt. Lett.* 34, 34(13), 2009.
- [109] H. Lu, J. Chung, X. Ou, C. Yang "Quantitative phase imaging and complex field reconstruction by pupil modulation differential phase contrast," *Optics Express*, 24(22), 2016.
- [110] F. Zernike, "Phase contrast, a new method for the microscopic observation of transparent objects part II" *Physica*, 9(10), 1942.
- [111] F. Zernike "How I Discovered Phase Contrast," *Science* 121(3141), 1955.
- [112] X. Yu, J. Hong, C. Liu, M. K. Kim, "Review of digital holographic microscopy for three-dimensional profiling and tracking," *Opt. Eng.*, 53(11), 2014.

- [113] M. Pluta, “Nomarski’s DIC microscopy: a review,” *Proc. SPIE 1846, Phase Contrast and Differential Interference Contrast Imaging Techniques and Applications*, (3 May 1994).
- [114] H. Ooki, Y. Iwasaki, J. Iwasaki, “Differential interference contrast microscope with differential detection for optimizing image contrast,” *Appl. Opt.* 35(13), 1996.
- [115] P. Bon, G. Maucort, B. Wattellier, S. Monneret, “Quadriwave lateral shearing interferometry for quantitative phase microscopy of living cells,” *Opt. Expr.*, 17(15), 2009.
- [116] Z. F. Phillips, M. Chen, L. Waller, “Single-shot quantitative phase microscopy with color-multiplexed differential phase contrast (cDPC),” *Plos one*, 12(2), 2017.
- [117] R. Kasprowicz, R. Suman, P. O’Tooleb, “Characterising live cell behaviour: Traditional label-free and quantitative phase imaging approaches,” *Int. J. Biochem. Cell Biol.*, 84, 2017.
- [118] A. B. Parthasarathy, K. K. Chu, T. N. Ford, J. Mertz, “Quantitative phase imaging using a partitioned detection aperture,” *Opt. Lett.*, 37(19), 2012.
- [119] T. N. Ford, K. K. Chu, J. Mertz, “Phase-gradient microscopy in thick tissue with oblique back-illumination,” *Nat. Methods* 9, 2012.
- [120] J. D. Giese, T. N. Ford, J. Mertz, “Fast volumetric phase-gradient imaging in thick samples,” *Opt. Expr.*, 22(1), 2014.
- [121] A. Guevara-Torres, D. R. Williams, and J. B. Schallek, “Imaging translucent cell bodies in the living mouse retina without contrast agents,” *Biomed. Opt. Express*, 6(6), 2015.
- [122] W. B. Amos, S. Reichelt, D. M. Cattermole, and J. Laufer, “Re-evaluation of differential phase contrast (DPC) in a scanning laser microscope using a split detector as an alternative to differential interference contrast (DIC) optics,” *J. Microsc.* 210(2), 2003.
- [123] D. Cuneffare, R. F. Cooper, B. Higgins, D. F. Katz, A. Dubra, J. Carroll, Sina Farsiu, “Automatic detection of cone photoreceptors in split detector adaptive optics scanning light ophthalmoscope images,” *Biomed. Opt. Express*, 7(5), 2016.
- [124] Y. N. Sulai, D. Scoles, Z. Harvey and A. Dubra, “Visualization of retinal vascular structure and perfusion with a nonconfocal adaptive optics scanning light ophthalmoscope,” *J. Opt. Soc. Am. A.*, 31(3), 2014.
- [125] T. Y. P. Chui, D. A. VanNasdale, Stephen A. Burns, “The use of forward scatter to improve retinal vascular imaging with an adaptive optics scanning laser ophthalmoscope,” *Biomed. Opt. Express*, 3(10), 2012.

- [126] T. Y. P. Chui, T. J. Gast, S. A. Burns, "Imaging of Vascular Wall Fine Structure in the Human Retina Using Adaptive Optics Scanning Laser Ophthalmoscopy," *Invest. Ophthalmol. Vis. Sci.*, 54(10), 2013.
- [127] E. A. Rossi, C. E. Granger, R. Sharma, Q. Yang, K. Saito, C. Schwarz, S. Walters, K. Nozato, J. Zhang, T. Kawakami, W. Fischer, L. R. Latchney, J. J. Hunter, M. M. Chung, D. R. Williams, "Imaging individual neurons in the retinal ganglion cell layer of the living eye," *PNAS*, 114 (3), 2017.
- [128] R. S. Jonnal, O. P. Kocaoglu, R. J. Zawadzki, Z. Liu, D. T. Miller, J. S. Werner "A Review of Adaptive Optics Optical Coherence Tomography: Technical Advances, Scientific Applications, and the Future" *Investigative Ophthalmology & Visual Science*, 57(9), 2016.
- [129] L. C. Shields, M. Materin J. A. Shields, "Panoramic Imaging of the Ocular Fundus," *Arch. Ophth.*, 121(11), 2003.
- [130] H. Heimann, F. Jmor, B Damato, "Imaging of retinal and choroidal vascular tumours," *Eye (Lond).*, 27(2), 2013.
- [131] A. Schalenbourg, L. Zografos, "Pitfalls in colour photography of choroidal tumours," *Eye (Lond).*, 27(2), 2013.
- [132] R. Rönnerstam, "Fundus examination using transscleral illumination," *Albrecht Von Graefes Arch Klin Exp Ophthalmol.*, 201(3), 1977.
- [133] D. Toslak, D. Thapa, Y. Chen, M. Erol, R. V. Chan, X. Yao, "Trans-palpebral illumination: an approach for wide-angle fundus photography without the need for pupil dilation," *Opt. Lett.*, 41(12), 2016.
- [134] W. A van den Bosch, I. Leenders, P. Mulder, "Topographic anatomy of the eyelids, and the effects of sex and age," *Br J Ophthalmol.*, 83(3), 1999.
- [135] M. Tidwell, R. S. Johnston, D. Melville, and T. A. Furness, "The Virtual Retinal Display - A Retinal Scanning Imaging System," in *Proceedings of Virtual Reality World '95*, ed. (IDG 1995), pp. 325-333.
- [136] M. Guillaumée, S. P. Vahdati, E. Tremblay, A. Mader, V. J. Cadarso, J. Grossenbacher, J. Brugger, R. Sprague, and C. Moser "Curved transreflective holographic screens for head-mounted display," in *Proc. SPIE 86430*, 864306, (2013).
- [137] F. W. Campbell, R.W. Gulbisch, "Optical quality of the human eye" *J. Physiol.*, 186(3), 1966.
- [138] W.J. Smith, "Modern Optical Engineering 4th edition," McGraw-Hill, 2007.
- [139] H. Kogelnik, "Coupled wave theory for thick hologram gratings," *Bell labs technical journal* 48(9), 1969.

- [140] A. Heifez, J. T. Shen, S. C. Tseng, G.S. Pati, J.-k. Lee and M.S. Shahriar, “Angular directivity of diffracted wave in Bragg-mismatched readout of volume holographic gratings” *Optics Communications*, 280(2), 2007.
- [141] Laser Institute of America, American National Standard for Safe Use of Lasers, ANSI
- [142] N. Streibl, “Phase imaging by the transport equation of intensity,” *Opt. Commun.*, 49(1), 1984.
- [143] G. Carles, G. Muyo, J. van Hemert, A. R. Harvey, “Combined high contrast and wide field of view in the scanning laser ophthalmoscope through dual detection of light paths,” *J. Biomed. Opt.*, 22(11), 2017.
- [144] M. Hammer, A. Roggan, D. Schweitzer, and G. Muller, “Optical properties of ocular fundus tissues — an in vitro study using the double-integrating-sphere technique and inverse Monte Carlo simulation,” *Phys. Med. Biol.*, 40(6), 1995.
- [145] M. Friebe, J. Helfmann, U. Netz, and M. Meinke, “Influence of oxygen saturation on the optical scattering properties of human red blood cells in the spectral range 250 to 2000 nm,” *J. Biomed. Opt.* 14(3), 2009.
- [146] A. N. Bashkatov, E. A. Genina, V. I. Kochubey, and V. V. Tuchin, “Optical Properties of Human Sclera in Spectral Range 370–2500 nm,” *Optics and Spectroscopy*, 109(2), 2010.
- [147] D. Kammler, “A First Course in Fourier Analysis,” Prentice Hall, 2000.
- [148] J. L. Starck, E. Pantin, “Deconvolution in Astronomy: A Review,” *Publications of the Astronomical Society of the Pacific*, 114(800), 2002.
- [149] M. Garcia, J. Ruiz-Ederra, H. Hernández-Barbáchano, E. Vecino “Topography of pig retinal ganglion cells,” *J Comp Neurol.*, 486(4), 2005.
- [150] M. J. Chandler, P. J. Smith, D. A. Samuelson, E. O. MacKay, “Photoreceptor density of the domestic pig retina,” *Vet Ophthalmol.*, 2(3), 1999.
- [151] C. G. Gerke, Y. Hao, F. Wong, “Topography of rods and cones in the retina of the domestic pig,” *Hong Kong Med*, 4, 1995.
- [152] ICNIRP guidelines on limits of exposure to incoherent visible and infrared radiation, *Health Physics*, 105(1), 2013.
- [153] D. Sliney et al. “Adjustment of guidelines for exposure of the eye to optical radiation from ocular instruments: statement from a task group of the International Commission on Non-Ionizing Radiation Protection (ICNIRP),” *Appl. Opt.* 44(11), 2005.

- [154] W.J. Smith, "Modern Optical Engineering 4th edition," McGraw-Hill, 2007.
- [155] W. J. Foster, A. Gupta, R. E. Engstrom, B. R. Straatsma, "Study of the PANORET–1000 wide–angle digital camera for use in imaging of choroidal tumors" *Investigative Ophthalmology & Visual Science*, 45(13), 2004.
- [156] J. B. Walsh, J. S. Garcia, J. C. Nieto, R. B. Rosen, P. T. Garcia, S. Fradin, "Wide-Angle Digital Fundus Photography: Panoret 1000 vs RetCam 120. *Investigative Ophthalmology & Visual Science*," 43(13), 2002.
- [157] T. Laforest, D. Carpentras, M. Kunzi, L. Kowalczyk, F. Behar-Cohen, C. Moser, "A new microscopy for imaging retinal cells," *Arxiv*, 2017.
- [158] P. Thévenaz, U. E. Ruttimann, M. Unser, "A Pyramid Approach to Subpixel Registration Based on Intensity," *IEEE Transactions on Image Processing*, 7(1), 1998.
- [159] M. Zacharria, B. Lamory, Nicolas Chateau, "Biomedical imaging: New view of the eye," *Nature Photonics*, 5(1), 2011.

Appendix A – Ramp approximation

Here I present a detailed version of the calculation used to derive (3.11) in section 3.1.2. For doing so, I need to introduce the circular, fully transmissive, aberration-free pupil function $p'_a(\mathbf{u}')$, defined as:

$$p'_a(\mathbf{u}') \triangleq \begin{cases} 1 & \text{for } |\mathbf{u}'| < a \\ 0 & \text{otherwise} \end{cases} \quad (\text{A.1})$$

By substituting this with the ramp approximation in (3.6) I obtain:

$$\begin{cases} B_{[S_{ev},P]} = q \iint |p'_a(\mathbf{u}')|^2 d^2\mathbf{u}' \\ H_{[S_{ev},P]}(\mathbf{u}) = -2q \iint p'_a(\mathbf{u}') p'_a(\mathbf{u} - \mathbf{u}') d^2\mathbf{u}' \\ G_{[S_{odd},P]}(\mathbf{u}) = 2jm \iint (\mathbf{v}_\varphi \cdot \mathbf{u}') p'_a(\mathbf{u}') p'_a(\mathbf{u} - \mathbf{u}') d^2\mathbf{u}' \end{cases} \quad (\text{A.2})$$

It is then convenient to introduce $p(\mathbf{u}')$, the pupil function in the case of $a = 1$ and such that:

$$p'_a(\mathbf{u}) = p\left(\frac{\mathbf{u}}{a}\right) \quad (\text{A.3})$$

By substituting this function into the previous system of equations I obtain:

$$\begin{cases} B_{q,a} = q \iint \left| p\left(\frac{\mathbf{u}'}{a}\right) \right|^2 d^2\mathbf{u}' \\ H_{q,a}(\mathbf{u}) = -2q \iint p\left(\frac{\mathbf{u}'}{a}\right) p\left(\frac{\mathbf{u} - \mathbf{u}'}{a}\right) d^2\mathbf{u}' \\ G_{m,a,\varphi}(\mathbf{u}) = 2jm \iint (\mathbf{v}_\varphi \cdot \mathbf{u}') p\left(\frac{\mathbf{u}'}{a}\right) p\left(\frac{\mathbf{u} - \mathbf{u}'}{a}\right) d^2\mathbf{u}' \end{cases} \quad (\text{A.4})$$

Then, by performing the change of variables: $\mathbf{u} = a\mathbf{u}_2$ and $\mathbf{u}' = a\mathbf{u}_n$, the integrals can be written as independent of a :

$$\begin{cases} B_{q,a} = q \iint |p(\mathbf{u}_n)|^2 a^2 d^2\mathbf{u}_n \\ H_{q,a}(a\mathbf{u}_2) = -2q \iint p(\mathbf{u}_n) p(\mathbf{u}_2 - \mathbf{u}_n) a^2 d^2\mathbf{u}_n \\ G_{m,a,\varphi}(a\mathbf{u}_2) = 2jm \iint (\mathbf{v}_\varphi \cdot a\mathbf{u}_n) p(\mathbf{u}_n) p(\mathbf{u}_2 - \mathbf{u}_n) a^2 d^2\mathbf{u}_n \end{cases} \quad (\text{A.5})$$

Since $|p(\mathbf{u}_n)|^2 = p(\mathbf{u}_n)$, the double integral in B is just the area of a circle of radius 1, so:

$$\iint |p(\mathbf{u}_n)|^2 a^2 d^2 \mathbf{u}_n = \pi \quad (\text{A.6})$$

Regarding the integrals of H and G , it is possible to notice that they are independent on any variable, besides φ . It is then convenient to define two new functions:

$$\begin{cases} h'(\mathbf{u}_2) = \iint p(\mathbf{u}_n) p(\mathbf{u}_2 - \mathbf{u}_n) d^2 \mathbf{u}_n \\ g'_\varphi(\mathbf{u}_2) = \iint (\mathbf{v}_\varphi \cdot \mathbf{u}_n) p(\mathbf{u}_n) p(\mathbf{u}_2 - \mathbf{u}_n) d^2 \mathbf{u}_n \end{cases} \quad (\text{A.7})$$

By substituting them into (A.5) and by using again the change of variables $\mathbf{u} = a\mathbf{u}_2$ I obtain:

$$\begin{cases} B_{q,a} = qa^2\pi \\ H_{q,a}(\mathbf{u}) = -2qa^2 h'\left(\frac{\mathbf{u}}{a}\right) \\ G_{m,a,\varphi}(\mathbf{u}) = 2jma^3 g'_\varphi\left(\frac{\mathbf{u}}{a}\right) \end{cases} \quad (\text{A.8})$$

In this way it is shown that a affects the function by expanding or contracting them (since it is multiplied to the spatial variable).

Regarding the effect of φ it is convenient to consider each \mathbf{u}_2 and \mathbf{u}_n as complex number, such that a rotation of value θ can be introduced simply by multiplying the quantity by $e^{j\theta}$. This will simplify the following notation without the need of introducing a rotation operator. Then it is possible to write:

$$g'_\varphi(e^{j\theta}\mathbf{u}_2) = \iint (\mathbf{v}_\varphi \cdot \mathbf{u}_n) p(\mathbf{u}_n) p(e^{j\theta}\mathbf{u}_2 - \mathbf{u}_n) d^2 \mathbf{u}_n \quad (\text{A.9})$$

By introducing $\mathbf{u}_n = e^{j\theta}\mathbf{u}_3$ I obtain:

$$g'_\varphi(e^{j\theta}\mathbf{u}_2) = \iint (\mathbf{v}_\varphi \cdot e^{j\theta}\mathbf{u}_3) p(e^{j\theta}\mathbf{u}_3) p(e^{j\theta}\mathbf{u}_2 - e^{j\theta}\mathbf{u}_3) d^2 \mathbf{u}_3 \quad (\text{A.10})$$

Since $p(e^{j\theta}\mathbf{u}_3) = p(\mathbf{u}_3)$ and since $\mathbf{v}_\varphi \cdot e^{j\theta}\mathbf{u}_3 = \mathbf{v}_{\varphi-\theta} \cdot \mathbf{u}_3$ I obtain:

$$g'_\varphi(e^{j\theta}\mathbf{u}_2) = \iint (\mathbf{v}_{\varphi-\theta} \cdot \mathbf{u}_3) p(\mathbf{u}_3) p(\mathbf{u}_2 - \mathbf{u}_3) d^2 \mathbf{u}_3 = g'_{\varphi-\theta}(\mathbf{u}_2) \quad (\text{A.11})$$

So it is possible to see that a change in φ is equivalent to a rotation of the coordinate system (or equivalently, of the function respect to the coordinate system).

To estimate the relationship between transfer function and contrast it is convenient to analyze the case of sinusoidal functions. To simplify the notation, I analyze the one-dimensional case, however, the same analysis can be done by using the two-dimensional case. The two functions can be written as:

$$\begin{cases} \mu(x) = \sin(u_0 x) \\ \phi(x) = \sin(u_0 x) \end{cases} \quad (\text{A.12})$$

To obtain the terms of the final image, it is necessary to Fourier transform the two terms and multiply them by h° and g° . Since h° is an even function, while g° is an odd one, by using the properties of the Dirac's delta function, it is obtained:

$$\begin{cases} h^\circ(u) \tilde{\mu}(u) = \frac{\sqrt{2\pi}}{2j} h^\circ(u_0) [\delta(u - u_0) - \delta(u + u_0)] \\ g^\circ(u) \tilde{\phi}(u) = \frac{\sqrt{2\pi}}{2j} g^\circ(u_0) [\delta(u - u_0) + \delta(u + u_0)] \end{cases} \quad (\text{A.13})$$

The first term is just the Fourier transform of the sinusoid multiplied by $h^\circ(u_0)$, while the second term is the Fourier transform of a cosine multiplied by $\frac{g^\circ(u_0)}{j}$. Since g° is a complex quantity, both of the terms are real values. This means that the amplitude of a sinusoid of frequency u_0 is just rescaled of a factor $h^\circ(u_0)$ or $g^\circ(u_0)$.



First and last name: Dino Carpentras

Date of birth: 16.08.1989

Place of birth: Sassari (SS), Italy

Gender: Male

Nationality: Italian

Telephone: +41 21 69 35184 (office)

Mobile phone: +41 78 953 92 61

e-mail: dino.carpentras@epfl.ch

Studies

- High School at Liceo Scientifico Europa Unita, Porto Torres, Italy (2002-2008).
 - Final exam's score: 100/100.
- Bachelor: Ingegneria Fisica at Politecnico di Torino, Torino, Italy (2008-2011).
 - Thesis on quantum key distribution in the laboratory of dr. M. Genovese at the Italian institute of metrology.
 - Final score: 110L/110.
- Master: Nanotechnology for ICT at Politecnico di Torino, Torino, Italy (2011-2013).
 - Thesis on microvalve for Lab on a disc technology in the laboratory of prof. M. Madou at the University of California, Irvine.
 - Final score: 110L/110.
- PhD in the Doctoral Program in photonics (EDPO) at École Polytechnique Fédérale de Lausanne (2013-Now) in the laboratory of prof. C. Moser.

Skills

- Use of standard software for simulations and data analysis (Comsol, Matlab, ImageJ).
- Practical experience on optical setups.
- Mathematical skills.
- Ability to work in a team.

Interests

I like spending time with friends and doing sport (especially running or doing martial arts). I enjoy tv-series and I love reading comic books.

Languages:

- Italian: mother tongue.
- English: fluent in oral and written form. (C1)
- French: simple conversations (B1)

Conferences

D. Carpentras, T. Laforest, D. Psaltis and C. Moser, "Overcoming the resolution limit in ophthalmology for Adaptive Optics and Wavefront Control" in Adaptive Optics and Wavefront Control in Microscopy and Ophthalmology, Paris (France), October 2015

D. Carpentras and C. Moser, "Biomedical imaging with wearable smart eyeglasses" for Biophotonics Japan, Tokyo (Japan), October 2015

D. Carpentras, T. Laforest, D. Psaltis, C. Moser, "Overcoming the resolution limit in retinal imaging using the scattering properties of the sclera," in Photonics West, San Francisco, California. (in Proc. SPIE 9717, 2016).

D. Carpentras and C. Moser, "Wearable see-through ophthalmoscope for point of care," in Photonics West, San Francisco, California, February 2017.

D. Carpentras, T. Laforest, M. Künzi, L. Kowalczyk, F. Behar-Cohen and C. Moser, "A novel technique for phase imaging of ex-vivo retina," in Face2Phase, Delft, Netherlands, October 2017.

Publications

A. Avella, G. Brida, D. Carpentras, A. Cavanna, I. P. Degiovanni, M. Genovese, M. Gramegna, P. Traina "Report on proof-of-principle implementations of novel QKD schemes performed at INRIM" Proc. SPIE 8542, (2012).

D. Carpentras, L. Kulinsky, M. Madou, "A Novel Magnetic Active Valve for Lab-on-CD Technology," J. Microelectromechanical Systems (2015).

D. Carpentras and C. Moser, "See-through ophthalmoscope for retinal imaging" J. Biomed. Opt. 22(5) (2017).

T. Laforest*, D. Carpentras*, L. Kowalczyk, F. Behar-Cohen, C. Moser, "Quantitative phase imaging of retinal cells" arXiv:1701.08854 (2017).

